

POLYMERIC PRINT HYDROGEL NANOPARTICLES:  
NEXT GENERATION DRUG DELIVERY VEHICLES TARGETING CANCEROUS TISSUE

Kevin Gerald Reuter

A dissertation submitted to the faculty of the University of North Carolina at Chapel Hill  
in partial fulfillment of the requirements for the degree of Doctor of Philosophy  
in the Department of Chemistry.

Chapel Hill  
2015

Approved by:

Joseph M. DeSimone

Samuel Lai

Sergei S. Sheiko

Andrew Wang

Wei You

© 2015  
Kevin Gerald Reuter  
ALL RIGHTS RESERVED

## ABSTRACT

Kevin Gerald Reuter: POLYMERIC PRINT HYDROGEL NANOPARTICLES:  
NEXT GENERATION DRUG DELIVERY VEHICLES TARGETING CANCEROUS TISSUE  
(Under the direction of Joseph M. DeSimone)

Standard cancer treatment generally consists of surgery, radiation, and small molecule chemotherapies that distribute systemically throughout the body. The systemic distribution of a toxic chemotherapeutic commonly produces unwanted side-effects leading to dose-limiting toxicity (such as fatigue, hair loss, anemia, nausea, nerve damage, and in some cases death). Accompanying the large volume of distribution ( $V_d$ ) and subsequent dose-limiting toxicity, small molecule therapies may display less than desirable pharmacokinetic behavior due to poor solubility and low permeability once administered orally or intravenously. Over the last 30 years of development, the use of nanoparticulate drug carriers has resulted in lowered  $V_d$ , enhanced solubility and permeability of the cargo, and improved efficacy in both academic and clinical endeavors. In addition, the increased size of a carrier, in comparison to the drug cargo, has been observed to enhance permeation and retention into the porous tumor vasculature. However, while manufacturing these nano-carriers, issues arise due to intrinsic particle heterogeneity associated with common fabrication methods. The use of Particle Replication in Non-wetting Templates (PRINT<sup>®</sup>) technology helps overcome this issue and allows for fine control over shape, size, modulus, composition, and surface chemistry. In this account, PRINT is employed to fabricate nanoparticle carriers that exhibit precisely engineered surface characteristics and size that are optimal for tumor deposition. The surface of PRINT hydrogels were precisely functionalized with a coating of poly (ethylene glycol), or PEG, that elicited inhibition of protein binding,

macrophage resistance, and a vastly improved blood circulation half-life compared to non-PEGylated counterparts upon administration *in vivo*. Upon attachment of an EGFR targeting affibody to the terminal end of this PEG group, dramatic changes were observed *in vitro* and *in vivo* with changes in density of targeting ligand. In addition, a number of different murine cancer models were analyzed for passive particle tumor accumulation revealing size and disease model dependent neoplastic sequestration, as well as, preferential accumulation in primary and metastatic disease sites. Finally, preliminary experimentation with environment-sensitive pro-drugs linkages revealed site-specific cargo release in dissolution studies. Overall, these efforts may lead to improved drug delivery to cancerous tissue and aid in the development of next generation drug delivery vehicles.

## ACKNOWLEDGEMENTS

Where do I start? In the twenty-seven years of my life I have come across so many influential people that have helped me become who I am today. When I was seven did I say to myself, “You know, I want to be in school for 20 more years and get a Ph.D.?” No. When I was seven I wanted to deliver pizza because I thought I would be able to eat it and maybe run into the Teenage Mutant Ninja Turtles. As I “matured”, I was influenced by my sister Jessica who seemed to always outperform me in school. With constant love and care of my parents, I took a liking to the challenge of school and what I thought it meant at the time. So really, my sister and parents started me on this path of “academic curiosity”, the desire to succeed at learning ... or at least getting good grades. That brings me next to my teachers, the really good ones, the engaging and passionate ones, the teachers that cared about me as a person. I was lucky and had teachers that helped me care beyond the letter grade. From grade school to college I was given one of the greatest advantages a young person can have ... a good teacher. These mentors helped me figure out that I was curious person and pushed me academically. The ones that pushed hard are the ones I remember the most. Throughout this entire process of growing up, the good and bad times, I had my friends and family. Where would I be without my cousins Dan and Ryan? Or my best buddies Travis, Justin, and Mark? Or Sarah, my calming presence and best friend throughout graduate school? Or my graduate school mentors Jillian, Chris, and Joe? Who would I be? I would be boring. I would be ordinary. I would not be who I am today. My friends and family, you have helped me become me. For that and everything else ... thank you. I love you all.

## TABLE OF CONTENTS

LIST OF FIGURES.....	xi
LIST OF TABLES.....	xvi
LIST OF SCHEMES.....	xvii
LIST OF EQUATIONS.....	xviii
LIST OF ABBREVIATIONS AND SYMBOLS.....	xix
CHAPTER 1 Nanoparticulate Drug Carriers as a Treatment for Cancer .....	1
1.1 A Brief History of Macromolecular-Based Drug Delivery .....	1
1.2 Key Parameters Facilitating Delivery to Solid Tumors .....	3
1.3 Nanoparticle Fabrication with PRINT Technology .....	15
1.4 References .....	18
CHAPTER 2 PEGylated PRINT Nanoparticles: The Impact of PEG Density on Protein Binding, Macrophage Association, Biodistribution, and Pharmacokinetics .....	22
2.1 Introduction.....	22
2.2 Results and Discussion .....	26
2.2.1 Nanoparticle Fabrication, Surface Modification, and Characterization .....	26
2.2.2 Protein Binding and In Vitro Assays .....	29
2.2.3 Circulation and Biodistribution Evaluation .....	32
2.3 Conclusions.....	37
2.4 Materials and Methods.....	38
2.4.1 Materials .....	38

2.4.2	Nanoparticle Fabrication.....	39
2.4.3	Nanoparticle Characterization .....	40
2.4.4	PEGylation Quantification.....	41
2.4.5	PEG Density Calculations.....	42
2.4.6	PEGylation and Acetylation for <i>In Vitro</i> and <i>In Vivo</i> Studies .....	43
2.4.7	Protein Binding Using Isothermal Titration Calorimetry .....	44
2.4.8	Macrophage Association Assay .....	44
2.4.9	In Vivo Studies .....	45
2.5	References.....	47
CHAPTER 3	Targeted PRINT Hydrogels: The Role of Nanoparticle Size and Ligand Density on Cell Association, Biodistribution, and Tumor Accumulation .....	51
3.1	Introduction.....	51
3.2	Results and Discussion .....	53
3.2.1	Passive Targeting: NP Fabrication, Surface Modification, and Characterization ....	53
3.2.2	Assessment of Passive Accumulation as Function of Particle Size.....	54
3.2.3	Active Targeting: Conjugation of Ligand at Distinct Surface Densities .....	55
3.2.4	<i>In vitro</i> Analysis as Function of Particle Size, Shape, and Ligand Density .....	58
3.2.5	Assessment of Biodistribution and Pharmacokinetics of Targeted Particles.....	64
3.3	Conclusions.....	67
3.4	Materials and Methods.....	68
3.4.1	Materials .....	68
3.4.2	Nanoparticle Fabrication.....	69
3.4.3	Nanoparticle Characterization .....	71

3.4.4	Surface Conjugation of NPs for Non-Targeted Studies.....	72
3.4.5	Affibody Quantification.....	72
3.4.6	Surface Conjugation of NPs for Targeted Studies .....	74
3.4.7	A431 Cell Association and Competition Assay.....	74
3.4.8	Macrophage Association Study .....	74
3.4.9	<i>In Vivo</i> Studies .....	75
3.5	References .....	78
CHAPTER 4 Mediating Passive Accumulation with PRINT Nanoparticles:		
	Effect of Particle Size and Tumor Model .....	81
4.1	Introduction.....	81
4.2	Results and Discussion .....	84
4.2.1	Particle Fabrication and Characterization .....	84
4.2.2	Biodistribution and Blood Pharmacokinetics in Healthy Mice .....	85
4.2.3	<i>In Vitro</i> Assessment of NPs.....	87
4.2.4	NP Distribution in Flank Tumor Models and Immunohistochemistry .....	88
4.2.5	NP Distribution in Orthotopic Tumor Models.....	92
4.3	Conclusions.....	96
4.4	Materials and Methods.....	97
4.4.1	Materials .....	97
4.4.2	Nanoparticle Fabrication.....	98
4.4.3	Nanoparticle Characterization .....	98
4.4.4	Surface Modification for <i>In Vitro</i> and <i>In Vivo</i> Experiments.....	99
4.4.5	Cellular Association Studies .....	99
4.4.6	<i>In Vivo</i> Studies .....	99



4.4.7 Immunohistochemistry Analysis .....	101
4.5 References .....	103
CHAPTER 5 Environment-Sensitive Drug Release from PRINT Nanoparticles .....	106
5.1 Introduction.....	106
5.2 Results and Discussion .....	109
5.2.1 Pro-drug Nanoparticle Fabrication and Characterization .....	109
5.2.2 Gemcitabine Release from Hydrogel Nanoparticles.....	112
5.2.3 Cytotoxicity of Gemcitabine-Loaded PRINT NPs .....	113
5.3 Materials and Methods.....	116
5.3.1 Materials .....	116
5.3.2 Pro-drug Incorporation and Particle Characterization .....	117
5.3.3 Drug Release and HPLC Quantification.....	117
5.3.4 Cytotoxicity Studies.....	118
5.4 Conclusions.....	119
5.5 References .....	120
CHAPTER 6 Future Work and Summary.....	122
6.1 Hydrogel PRINT Nanoparticles for the Treatment of Cancer .....	122
6.2 The PEGylation Paradox.....	123
6.3 Summary .....	126
6.3.1 PEGylated PRINT Nanoparticles: The Impact of PEG Density on Protein Binding, Macrophage Association, Biodistribution, and Pharmacokinetics .....	126
6.3.2 Targeted PRINT Hydrogels: The Role of Nanoparticle Size and Ligand Density on Cell Association, Biodistribution, and Tumor Accumulation .....	127

6.3.3	Mediating Passive Accumulation with PRINT Nanoparticles: The Effect of Particle Size and Tumor Model .....	127
6.3.4	Environment-Sensitive Drug Release from PRINT Nanoparticles .....	129
6.4	References .....	130
APPENDIX.....		132

## LIST OF FIGURES

Figure 1.1 Nanoparticle characteristics for in vivo biocompatibility. <sup>6</sup> .....	4
Figure 1.2 Margination of non-spherical particulates to the vessel wall while spherical counterparts remain in center of the blood flow. <sup>17</sup> .....	6
Figure 1.3 Active and passive accumulation mechanisms of a nanoparticle platform for cancer therapy. <sup>7</sup> .....	12
Figure 1.4 The role of nanoparticle shape in binding avidity between the ligand and the target receptor. <sup>17</sup> .....	14
Figure 2.1 Scanning electron image of 80 nm x 80 nm x 320 nm PRINT hydrogel nanoparticles, scale bar represents 500 nm.....	27
Figure 2.2 PEG density quantification of 80 nm x 320 nm particles reacted with 14.0 and 2.0 mg of fluorescein-PEG5k-SCM resulting in brush ( $0.083 \pm 0.006$ PEG / nm <sup>2</sup> ) and mushroom ( $0.028 \pm 0.002$ PEGs / nm <sup>2</sup> ) conformations, respectively (n = 6). .....	27
Figure 2.3 Cartoon representation of 80 nm x 80 nm x 320 nm PRINT hydrogel nanoparticles with functionalized PEG in brush (A) and mushroom (B) conformations. ....	28
Figure 2.4 Mass of adsorbed BSA on non-PEGylated, PEG mushroom and PEG brush NPs (n = 3; insert is a representative image raw data collected from the isothermal titration calorimetry experiments). .....	30
Figure 2.5 Percent of MH-S cells associated with non-PEGylated, PEG mushroom and PEG brush nanoparticles after various incubation times (n = 3). .....	31
Figure 2.6 Intravital microscopy circulation profiles based upon fraction of maximum fluorescence remaining for non-PEGylated, PEG mushroom, and PEG brush nanoparticles. ....	32
Figure 2.7 Concentration of nanoparticles in blood over time (n = 4). Data is fit to a two-compartment PK model (solid lines) .....	33
Figure 2.8 Biodistribution of nanoparticles at 0.083 h post-injection, expressed as percent recovered fluorescence per organ (n = 4). ....	34
Figure 2.9 Biodistribution of nanoparticles at 0.25 h post-injection, expressed as percent recovered fluorescence per organ (n = 4). ....	34

Figure 2.10 Biodistribution of nanoparticles at 0.5 h post-injection, expressed as percent recovered fluorescence per organ (n = 4). .....	35
Figure 2.11 Biodistribution of nanoparticles at 1 h post-injection, expressed as percent recovered fluorescence per organ (n = 4).....	35
Figure 2.12 Biodistribution of nanoparticles at 3 h post-injection, expressed as percent recovered fluorescence per organ (n = 4).....	36
Figure 2.13 Biodistribution of nanoparticles at 24 h post-injection, expressed as percent recovered fluorescence per organ (n = 4).....	36
Figure 3.1 Scanning electron micrograph of 80 x 320 nm (left) and 55 x 60 nm (right) hydrogel PRINT nanoparticles. ....	54
Figure 3.2 Biodistribution of PEGylated 80 x 320 nm and 55 x 60 nm NPs at 24 h in A431 tumor-bearing mice (inset - enhanced view of blood, tumor, kidney, and lung at 24 h). ....	55
Figure 3.3 Quantification of targeting ligand on 80 x 320 nm (left) and 55 x 60 nm (right) NPs based upon various amounts of fluorescein-labeled Z <sup>EGFR</sup> affibody charged .....	57
Figure 3.4 Quadrants upon bivariate analysis of flow cytometry of cell-association with targeted nanoparticles. ....	59
Figure 3.5 In vitro association of A431 cell population upon incubation with targeted 80 x 320 nm (top) and 55 x 60 nm NPs (bottom). Two cell populations are shown, one with NPs both bound to the outer cell membrane and internalized (left) and a second population with NPs only internalized (right). ....	61
Figure 3.6 Sub-populations A431 cell interactions with 80 x 320 nm particles at five different targeting ligand densities and various dosages. ....	62
Figure 3.7 Percent association of alveolar macrophage cells (MH-S) with targeted 80 x 320 nm (left) and 55 x 60 nm (right) at three distinct ligand densities.....	62
Figure 3.8 Average mean fluorescence intensity of alveolar macrophage cells (MH-S) associated with targeted 80 x 320 nm (left) and 55 x 60 nm (right) at three distinct ligand densities.....	63
Figure 3.9 A431 cell association of 80 x 320 nm particles (ligand density = $1.1 \times 10^{-3}$ LG/nm <sup>2</sup> with pre-dose of free affibody administered at five different concentrations 30 min. prior to particle addition. ....	64

Figure 3.10 Blood pharmacokinetics of 80 x 320 nm NPs at various targeting densities [square = $6.5 \times 10^{-4}$ LG/nm <sup>2</sup> triangle = $1.8 \times 10^{-3}$ LG/nm <sup>2</sup> ; inverted triangle = $4.5 \times 10^{-3}$ LG/nm <sup>2</sup> ] at five time points (0.083, 0.5, 1, 3, and 24 h). PEGylated [circle] and wild-type [diamond] used as controls (n = 4).....	65
Figure 3.11 Biodistribution of 80 x 320 nm particles at 24 hours. PEGylated and wild-type affibody particles used as controls [Low LG = $6.5 \times 10^{-4}$ LG/nm <sup>2</sup> ; Med LG = $1.1 \times 10^{-3}$ LG/nm <sup>2</sup> ; High LG = $1.8 \times 10^{-3}$ LG/nm <sup>2</sup> ].....	66
Figure 3.12 Biodistribution (left) and accumulation ratio between tumor and whole blood (right) with 55 x 60 nm NPs at 24 hours. PEGylated and Taq polymerase binder, a bacterial-binding protein, NPs were used as controls [Low LG = $1.2 \times 10^{-3}$ LG/nm <sup>2</sup> ; Med LG = $2.0 \times 10^{-3}$ LG/nm <sup>2</sup> ; High LG = $3.0 \times 10^{-3}$ LG/nm <sup>2</sup> ]. ....	67
Figure 4.1 Scanning electron micrographs of 55 x 60 nm, 80 x 180 nm, and 80 x 320 nm PRINT hydrogel particles. ....	84
Figure 4.2 Blood pharmacokinetics of three NP types in healthy mice at several time points: 0.5, 4, 24, 48, and 72 h (n = 5 per NP arm). ....	86
Figure 4.3 Biodistribution of 55 x 60, 80 x 180, and 80 x 320 nm in healthy mice at 24 hour post-injection at 60 mg / kg (n = 4).....	87
Figure 4.4 <i>In vitro</i> cell association of various NP types with murine macrophages (MH-S) and three different cancer cell types (A431, A549, and SKOV-3). ....	88
Figure 4.5 Flank tumor accumulation of PRINT particles of various sizes and shapes was evaluated at 24 h post-injection at 60 mg/kg. Data displayed as percent recovered fluorescence per gram of tissue (n = 4).....	90
Figure 4.6 Biodistribution of NPs at three distinct sizes in four different tumor-bearing mouse models at 24 h post-injection (60 mg / kg). Organs of interest were resected and fluorescently imaged (n = 4).....	90
Figure 4.7 Photographs of different flank tumors once resected from the mouse. ....	91
Figure 4.8 Immunohistochemistry analysis of paraffin-fixed flank tumors. Vascularization of the cancerous tissue was identified with a CD-31 marker. Complete vessel is defined as endothelial tissue coupled with lumen. ....	92
Figure 4.9 Immunohistochemistry analysis of paraffin-fixed flank tumors with several markers: lymphatic vessel (Lyve1), tumor-associated macrophage (F480), collagen (Collagen IV), and vascular endothelial growth factor (VEGF).....	92

Figure 4.10 Photograph and fluorescence images of orthotopic 344SQ (left two) and A549 (right two) tumors treated with fluorescently labeled PRINT particles indicating preferential accumulation of particles in diseased tissue. White triangles indicate primary tumors, and blue triangles indicate either lymph node metastasis or pleural cavity tumors. ....	94
Figure 4.11 Representative photograph of orthotopic SKOV-3 tumors (indicated by the white triangle) formed in the IP cavity of a nude mouse. ....	94
Figure 4.12 Biodistribution of 55 x 60 nm particles in tumor-bearing mice 24 h post-injection (60 mg / kg). Organs of interest were resected and imaged via fluorescence. Both orthotopic (gray bar) and flank (black bar) tumor models were investigated for the following cell lines (A) 344SQ, (B) A549, (C) SKOV3. Total fluorescence of diseased tissue was compared in orthotopic models (D). ....	95
Figure 4.13 Biodistribution of 55 x 60 nm particles in metastatic disease sites throughout the three orthotopic mouse models: A549 (top-left), SKOV-3 (top-right), and 344SQ (bottom). ....	96
Figure 5.1 Base chemotherapeutic gemcitabine (top) and subsequent derivatives: diisopropyl silyl ether acrylate (iPr-GEM; middle) and reducible disulphide acrylate (SS-GEM; bottom). ....	110
Figure 5.2 Scanning electron microscopic images of harvested iPr-GEM NPs (left) and laminated SS-GEM (right) loaded 80 nm x 80 nm x320 nm [scale bar on right = 1 $\mu$ m]. ....	111
Figure 5.3 Release of free gemcitabine from iPr-GEM loaded 80 x 320 nm NPs upon dissolution as quantified by HPLC (time points: 0, 1, 4, 24, 48, and 120 hours). ....	113
Figure 5.4 Release of free gemcitabine from SS-GEM loaded 80 x 320 nm NPs upon dissolution in 5 mM glutathione as quantified by HPLC (time points: 0, 1, 4, 24, 48, and 120 hours). ....	113
Figure 5.5 Cytotoxicity of SS-GEM loaded 80 x 320 nm NPs dosed onto 344SQ (mouse non-small cell lung carcinoma) cells with approximate IC <sub>50</sub> values of 4, 60, and 500 nM for the free-gemcitabine, SS-GEM pro-drug, and SS-GEM loaded NPs, respectively. ....	115
Figure 5.6 Cytotoxicity of SS-GEM loaded 80 x 320 nm NPs dosed onto A549 (GFP-expressing human non-small cell lung carcinoma) cells with approximate IC <sub>50</sub> values of 3, 15, and 125 nM for the free-gemcitabine, SS-GEM pro-drug, and SS-GEM loaded NPs, respectively. ....	115

Figure 5.7 Cytotoxicity of SS-GEM loaded 80 x 320 nm NPs dosed onto A431 (human epidermoid carcinoma) cells with approximate IC <sub>50</sub> values of 4 and 100 nM for the free-gemcitabine and SS-GEM pro-drug, respectively. No IC <sub>50</sub> for drug loaded NPs was quantified.....	116
Figure 6.1 Diorthoester (A), hydrazone (B), and $\beta$ -thiopropionate (C) pH-sensitive linkages commonly used with sheddable PEG and subsequent hydrolysis reactions (R <sub>1</sub> = PEG, R <sub>2</sub> = NP). <sup>2</sup> .....	125
Figure A.1 Chromatogram of gemcitabine·HCl (0.25 mg / mL in sterile water) upon analysis via HPLC (Abs = 267 nm) with observed elution time of ~ 6.5 m.....	132
Figure A.2 Chromatogram of SS-GEM pro-drug (0.1 mg / mL in sterile water) upon analysis via HPLC (Abs = 267 nm) with observed elution time of ~ 13.4 m.....	132
Figure A.3 Chromatogram of iPr-GEM pro-drug (0.1 mg / mL in sterile water) upon analysis via HPLC (Abs = 267 nm) with observed elution time of ~ 22.2 min.....	133
Figure A.4 Standard curve of gemcitabine (10 standard dilutions) upon analysis via HPLC (Abs = 267 nm).....	133

## LIST OF TABLES

Table 1.1 Synthetic Polymers as Cancer Therapeutics* .....	2
Table 1.2 Common Excipients Used For Oral and Injectable Formulations <sup>31</sup> .....	9
Table 2.1 Comparison of parameters used to determine surface PEG density on nanoparticles and their biological interactions. ....	25
Table 2.2 Nanoparticle characterization based upon dynamic light scattering .....	29
Table 2.3 Pharmacokinetic parameters from two-compartment model fit of blood concentration data. ....	37
Table 2.4 Constants of integration from two-compartmental model fit of blood concentration data with coefficient of determination ( $R^2$ ). ....	37
Table 3.1 Nanoparticle characterization via dynamic light scattering.....	54
Table 3.2 Targeted nanoparticle characterization by dynamic light scattering .....	58
Table 3.3 Pharmacokinetic parameters of targeted 80 x 320 nm NPs .....	66
Table 4.1 Particle characterization by dynamic light scattering .....	85
Table 4.3 Blood pharmacokinetics as a function a nanoparticle type.....	86
Table 5.1 Composition of drug-loaded PRINT NPs .....	111
Table 5.2 Dynamic light scatting of prodrug-loaded 80 nm x 80 nm x 320 nm NPs .....	111
Table 5.3 $IC_{50}$ values of Gemcitabine in Three Cancer Cell-lines .....	114



## LIST OF SCHEMES

Scheme 1.1 Batch PRINT translation to the novel roll-to-roll system .....	17
Scheme 1.2 The R2R process .....	17
Scheme 3.1 Conjugation of PRINT NPs to targeting ligand .....	57

## LIST OF EQUATIONS

Equation 2.1 .....	28
Equation 2.2 .....	28
Equation 2.3 .....	28
Equation 2.4 .....	42
Equation 2.5 .....	43
Equation 2.6 .....	43
Equation 2.7 .....	43
Equation 2.8 .....	43

## LIST OF ABBREVIATIONS AND SYMBOLS

°C	degrees Celsius
°F	degrees Fahrenheit
μL	microliters
μm	micrometer
344SQ	mouse non-small cell lung cancer
A	area
A431	human epidermoid carcinoma
A549	human non-small cell lung cancer
ADCs	antibody-drug conjugates
AEM	aminoethyl methacrylate
AFM	atomic force microscopy
AIC	Akaike information criteria
A <sub>lipid</sub>	area of lipid
API	active pharmaceutical ingredient
Arg	arginine
Asp	aspartic acid
Au	gold
AUC	area-under-curve
BSA	bovine serum albumin
CL	clearance
CSM	cure-site monomer
D	distance

d	nanoparticle diameter
D <sub>h</sub>	hydrodynamic diameter
DLS	dynamic light scattering
DMEM	Dulbecco's modified eagle medium
DMF	N,N-dimethylformamide
DPBS	Dulbecco's phosphate buffered saline
DTT	dithiothreitol
EDTA	ethylenediaminetetraacetic acid
EGFR	epidermal growth factor receptor
EPR	enhanced permeation and retention
<i>f</i>	mass fraction
FACS	fluorescence assisted cell sorting
FBS	fetal bovine serum
FDA	U.S. Food and Drug Administration
FITC	fluorescein isothiocyanate
g	gram
GEM	gemcitabine
Gly	glycine
GSH	glutathione
h	hour
HEPES	(4-(2-hydroxyethyl)-1-piperazineethanesulfonic acid)
HER-2	human epidermal growth factor receptor - 2
HP <sub>4</sub> A	hydroxyl (PEG) <sub>4</sub> acrylate

HPLC	high performance liquid chromatography
Hz	Hertz
IC <sub>50</sub>	half maximal inhibitory concentration
IHC	immunohistochemistry
IR	infrared
ITC	isothermal titration calorimetry
IV	intravenous
IVM	intravital microscopy
kg	kilogram
L	length
LG	ligand
m	mass
mg	milligrams
MH-S	mouse alveolar macrophage
min	minute
mL	milliliters
mM	millimolar
M <sub>n</sub>	number average molecular weight
mol	mole
M <sub>PEG</sub>	molecular weight of polyethylene glycol
MPS	mononuclear phagocyte system
mV	millivolts
M <sub>w</sub>	weight average molecular weight

N	number monomers per polymer chain
N <sub>A</sub>	Avogadro's number
NHS	n-hydroxide succinimide
nm	nanometer
NP	nanoparticle
NSCLC	non-small cell lung cancer
PBS	phosphate buffered saline
PD	pharmacodynamics
PDI	polydispersity index
PECAM	platelet endothelial cell adhesion molecule
PEG	polyethylene glycol
PET	polyethylene terephthalate
PK	pharmacokinetics
PLGA	polylactic-co-glycolic acid
ppm	parts per million
PPS	pre-particle solution
PRINT	Particle Replication In Non-wetting Templates
PSI	pressure per square inch
Pt	platinum
PTFE	polytetrafluoroethylene
PVOH	polyvinyl alcohol
R2R	roll-to-roll
RBC	red blood cell

RCF	relative centrifugal force
RES	reticuloendothelial system
$R_F$	Flory radius
RH	relative humidity
RPM	rotations per minute
S	PEG density
$SA_{NP}$	surface area of nanoparticle
SCM	succinimidyl carboxymethyl ester
SEC	size exclusion chromatography
SEM	scanning electron microscopy
SKOV3	human ovarian carcinoma
SPR	surface plasmon resonance
$t_{1/2}$	half-life
TAMs	tumor-associate macrophages
TB	trypan blue
TCEP	tris (2-carboxyethyl) phosphine
TEA	triethylamine
TFA	trifluoroacetic acid
TGA	thermal gravimetric analysis
TGF- $\beta$	tumor growth factor beta
TPO	diphenyl (2,4,6-trimethylbenzoyl)-phosphine oxide
$\mu\text{cal}$	microcalories
$\mu\text{M}$	micromolar

UV-LED	ultraviolet-light emitting diode
V	volume
$V_d$	volume of distribution
VEGF	vascular endothelial growth factor
wt	weight
XPS	X-ray photoelectron spectroscopy
$\alpha$	monomer length
$\zeta$	zeta potential
$\lambda_{em}$	emission wavelength
$\lambda_{ex}$	excitation wavelength
$\rho$	density



## CHAPTER 1 NANOPARTICULATE DRUG CARRIERS AS A TREATMENT FOR CANCER

### 1.1 A Brief History of Macromolecular-Based Drug Delivery

Dr. Richard Feynman, the charismatic Nobel laureate, suggested in 1959 that one day we could “swallow the doctor”. That lecture, “There’s Plenty of Room at the Bottom”, helped ignite a scientific revolution in the field of nanotechnology that continues to this day.<sup>1</sup> As the revolution continues, the question proposed by Feynman remains, “[what if] we can arrange atoms the way we want them” and “swallow the doctor”? The medical community is now realizing how provocative that lecture was as drug design at the molecular level is beginning to benefit the patient in ways previously thought impossible.

In the mid-1970’s Helmut Ringsdorf hypothesized that synthetic polymers could promote innate therapeutic benefit.<sup>56</sup> The key idea was unlike low molecular weight therapeutics with high pharmacokinetic volume of distribution ( $V_d$ ) and systemic toxicities, polymers could reduce  $V_d$  due to cellular internalization being limited to endocytosis rather than diffusion. While polymeric drug carriers were already in development, Ringsdorf proposed that by altering an intrinsically non-toxic polymer major alterations could be made to its pharmacokinetics, pharmacodynamics, and cell-receptor interactions. Additionally, Ringsdorf described several polymeric characteristics that may affect these *in vivo* outcomes: molecular weight (Mw), coil structure, co-polymer composition, tacticity, and polyelectrolyte charge. In one fascinating example, poly (vinylpyridine)-N-oxides were found to be active against silicosis, a respiratory disease caused by breathing in silica dust, a common issue in any chemical laboratory.<sup>66,67</sup>

Unlike low molecular weight isopropylpyridine-N-oxides, the polymer was discovered to protect macrophage in the lung from injury by coating the silica particulates, in effect, preventing lysosomal membrane interaction, and subsequent rupture. From discoveries just like this, a field of synthetically derived therapeutically active polymers originated (Table 1.1). As macromolecular therapies against cancer advanced, in the mid-1980's a discovery was made at Kumamoto University Medical School in Japan which spurred the field of nanomedicine.

Table 1.1 Synthetic Polymers as Cancer Therapeutics\*

Polymer	Preclinical Anticancer Activity	Reference
Polyetheneimine (Mw Not reported)	Ehrlich ascites via direct antitumor therapeutic effect	57
Polylysine (Mw = 50 k)	Non-lympocytic cell line K562 via direct antitumor therapeutic effect	58
DEAE-dextran (diethylamino-ethyl-dextran) [Mw = $2 \times 10^7$ ]	NJA leukemia, JBJ ascites, plasmocytoma, and yoshida ascites in vivo	59
Poly(Arg-Gly-Asp) [Mw = 10k]	Metastasis and migration inhibition of B16-BL6 melonoma cells via ECM	60
Sulfated and carboxymethylated-Chitin [Mw = 10-60k]	Cell attachment and migration of B16-BL6 melanoma cells via ECM	61
Divinyl ether-maleic anhydride copolymer [Mw < 18k]	Stimulates host immune system with L1210 mice polymer coupled with decitabine resulted in cures	62
Maleic anhydride-ethylene copolymer [Intermediate Mw]	Inhibition of nuceloside uptake in HM5-Carb/S melonoma in vivo	63
1,3 bis (methylaminocarboxy)-2 methylene propane carbamate and N-vinylpyrrolidone copolymer [Mw = 5.8k]	May act via stimulation of host immune system against 180 sarcoma, P388 leukemia, and carcinoma F0771 in mice, and Walker 1098 in rats	64

\*Table Adapted from Advances in Polymer Science, Vol. 122 written by D. Putnam and J. Kopecek<sup>65</sup>

In 1986, Yasuhiro Matsumura and Hiroshi Maeda made a discovery that reflected the revelations of Dr. Feynman with their discovery of the enhanced permeation and retention effect (EPR) of tumor vasculature. Utilizing radio-labelled proteins of various sizes, they were able to probe the effects of macromolecular size towards tumoritropic accumulation. In these

groundbreaking studies, they found that large molecular weight proteins (29,000-160,000 g / mol) accumulated preferentially in Sarcoma 180 tumors located on the rear flank of ddY mice in comparison to smaller molecular weight proteins (12,000 and 16,000 g / mol). In these preliminary experiments, they speculated that the preferential sequestration was due to the hypervascularity network of tumors caused by rapid angiogenesis, as well, they proposed that the persistence of large macromolecules in tumor tissue could be attributed to an overall lack of lymphatic network. These discoveries in the 1980's spurred an entirely new field of drug delivery that exploits preferential tumoritropic accumulation.<sup>2</sup>

Macromolecules were soon conjugated to potent chemotherapeutics in a number of polymeric and protein-based matrices and structures. Similar to the macromolecular system developed by Maeda, albumin and cage-like viral drug-conjugates were constructed that exhibit biologic compatibility and are inert by nature. Micelles and liposomes were one of the first nanocarriers developed due to their ability to self-assemble and form a core around the desired therapeutic. Along with the encapsulation of drug, liposomes and micelles exhibit biocompatibility and facile surface modification if the innate particle characteristics are undesirable. Polymeric nanoparticles and dendrimers are remarkable in the diversity of therapeutic cargos as both hydrophilic and hydrophobic drugs can be functionalized to the carrier.<sup>3</sup> The vast number of drug delivery systems that have been developed points to how impactful the findings of Maeda and Matsumura were.

## 1.2 Key Parameters Facilitating Delivery to Solid Tumors

Current drug delivery vehicles are limited by their physical characteristics as only certain particle parameters facilitate successful delivery to solid tumors. Size, shape, modulus,

composition, and surface functionality are the key factors that contribute to the interaction of nanoparticles and the biological systems they are administered into. These parameters have drastic effects on cytotoxicity, reticuloendothelial system (RES) recognition, and how effective the carrier penetrates into the diseased mass via the EPR effect. In a broad sense, cytotoxicity concerns can be addressed by negating the positive surface charge and tumor penetration can be enhanced by limiting particle size to sub-100 nm.<sup>4</sup> However, there are a number of particle parameters that should also be modified in order to evade the reticuloendothelial system (RES) responsible for eliminating foreign, “non-self”, entities from the body. Kupffer cells (liver), alveolar macrophages (lungs), splenic histiocytes, and systemic macrophages in the blood are just a few illustrations of RES cells that are located throughout the body and are responsible for nanoparticle clearance.<sup>5</sup> Along with elimination via RES, mechanical filtration is another route for particle clearance, renal clearance is prevalent with particles smaller than 8 nm, liver and splenic filtration with rigid particles larger than 200 nm, and biliary excretion with diameters less than 30-40 nm (diameter<sub>bile duct</sub> ~ 30 nm).<sup>6</sup> With these limits of mechanical filtration in mind, a particle of certain physical parameters can be designed that better avoids filtration and effectively transports to the site of interest (Figure 1.1).<sup>6</sup>

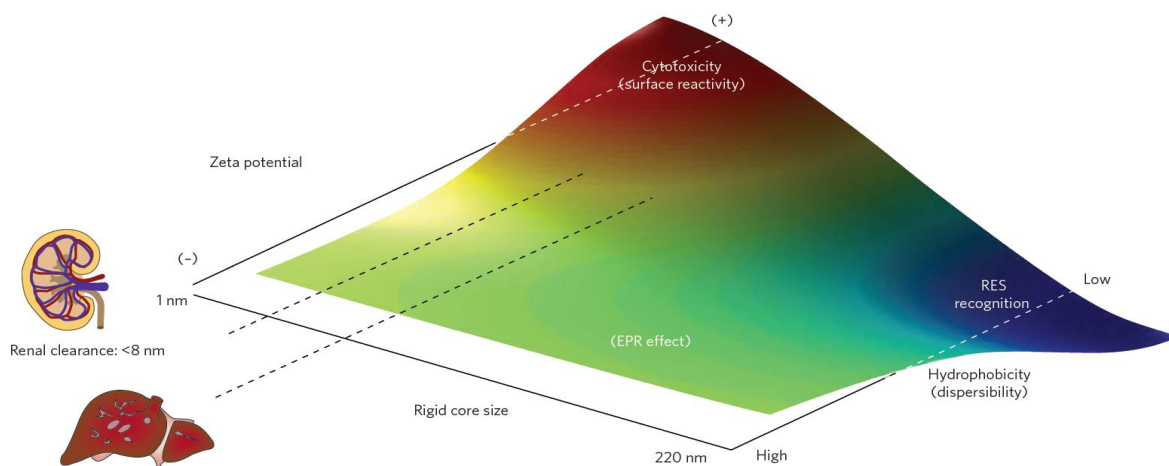


Figure 1.1 Nanoparticle characteristics for in vivo biocompatibility.<sup>6</sup>

Blood persistence is paramount for a therapeutic carrier to enhance tumor accumulation. The EPR effect is dependent on a long-circulating nanocarrier, as the particles must remain in circulation long enough to passively accumulate in the cancerous tissue and release their cargo. Size and shape are two important factors in engineering a long-circulating nanoparticle and significant work has been conducted to lay the foundation for the appropriate NP size ranges.<sup>4,8</sup> The majority of NP shapes are limited to a roughly spherical shape due to a limited availability of techniques to produce non-spherical particles. Recently, a number of fabrication technologies have been developed that result in shape specificity. Due to this new advancement, the effects of particle shape on circulation profiles, cell kinetics, and biodistribution have now been studied.<sup>9,10-17</sup>

A key factor in particle circulation is the ability to marginate towards the epithelial walls within the blood vessels. Margination enhances the probability of the nanocarrier to extravasate into the tortuous neoplastic vasculature and significant work has been conducted in this area comparing spherical and non-spherical particles of various sizes.<sup>17-20</sup> Interestingly, higher aspect ratios have been shown to marginate more readily than spherical particles (Figure 1.2) and also reduce macrophage association when tested *in vitro*.<sup>11,22,23</sup> With the higher rate of margination and decreased macrophage uptake, particle filtration out of circulation by the RES and subsequent sequestration in the liver and spleen is mitigated.<sup>15,22,24</sup>

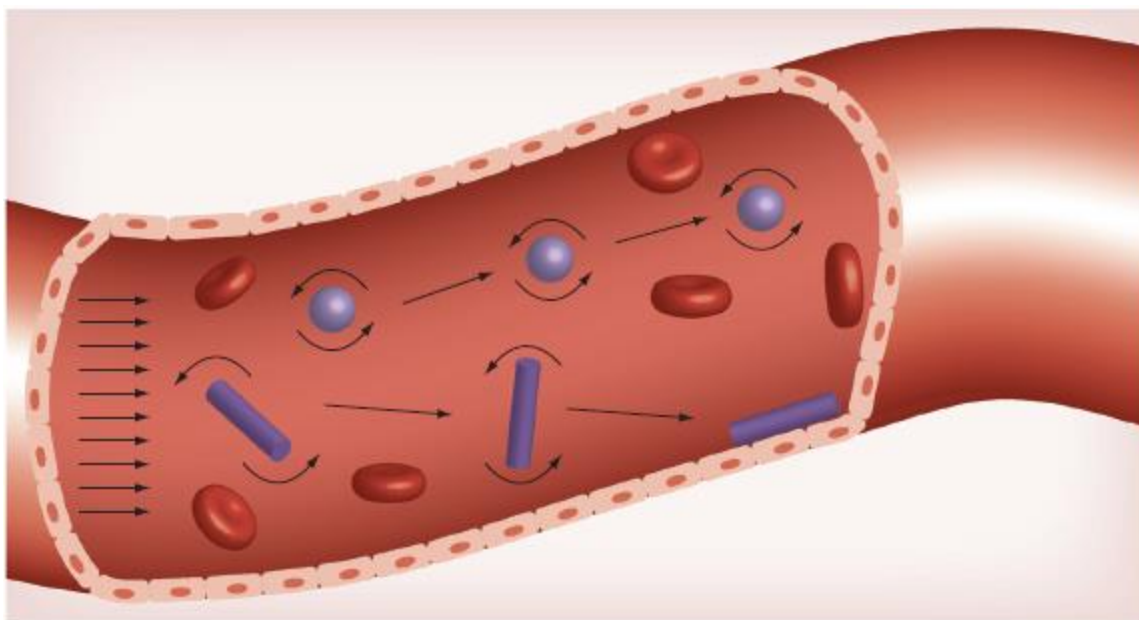


Figure 1.2 Margination of non-spherical particulates to the vessel wall while spherical counterparts remain in center of the blood flow.<sup>17</sup>

Upon avoiding filtration by the RES, the carrier must passively accumulate in the cancerous tissue and effectively extravasate into the diseased tissue. An underreported factor in this particle extravasation is the high degree of heterogeneity in the tumor tissue. Not only is there dramatic heterogeneity amongst different tumor models and cell-lines, but, significant differences exist across a single cancerous mass.<sup>54,55</sup> The complexity of cancer tissue has spurred studies into what particle types penetrate most effectively into solid tumors. Similar to previous work in blood circulation profiles, high aspect ratio particles have proven advantageous as they penetrate more rapidly into solid tumors when compared to spherical counterparts.<sup>25</sup> In other accounts, high aspect ratio particles also have shown to internalize more readily into cancer cells when tested *in vitro* with HeLa cells.<sup>16</sup> Across literature, high aspect ratio particles have shown to greatly improve a number of key factors that facilitate particulate delivery to solid tumor masses.

In the labs of Joseph DeSimone, the benefits of aspect ratio are being studied thoroughly with the use of the nanofabrication technique known as Particle Replication in Non-wetting

Templates (PRINT). Utilizing PRINT, the DeSimone lab was able to fabricate poly (lactic-co-glycolic) acid particles of two distinct sizes: 200 nm x 200 nm and 80 nm x 80 nm x 320 nm. In these studies, docetaxel was encapsulated within the PLGA matrix at similar concentrations and then administered intravenously into mice bearing SKOV-3 human ovarian carcinoma xenografts. Both PRINT NP arms outperformed the free drug control, Taxotere, and the 80 x 320 nm type enhanced blood and tumor retention while lowering splenic and liver accumulation over the 200 x 200 nm type.<sup>26</sup> These advancements in carrier persistence in the blood, avoidance of organ filtration, and tumor delivery translated to vastly improved efficacy in an A549 orthotopic xenograft model.<sup>27</sup>

In addition to size and shape, particle modulus plays a role in avoiding physical filtration as low-modulus particles can circumvent the seemingly stringent size limitations. Red blood cells (RBCs) are a great representation of modulus effects *in vivo*. RBCs are ~8  $\mu\text{m}$  in diameter and exhibit extraordinary deformability as they can pass through splenic slits 2-3  $\mu\text{m}$  wide.<sup>28</sup> Yet as the RBCs age, the cells stiffen, are no longer malleable, and are removed from circulation by the slits in the spleen. In the DeSimone lab, deformable hydrogel red blood cell mimics (RBCMs) were created whose mechanical properties could be modified via cross-linkage density. Cross-linker incorporation of 1% by weight into the particle matrix generated a modulus of approximately 8 kPa and the resulting blood pharmacokinetic profile was extended dramatically exhibiting an elimination half-life on the order of four days.<sup>29</sup> Filamentous PRINT-based, 80 nm x 5000 nm, particles were also fabricated that exhibited similar low cross-link density. These particles were able to pass through a 200 nm porous membrane, mimicking the pores found in the liver and spleen. However, rigid, asbestos-like, particles were unable to permeate through the tight junctions and smaller particles (80 nm x 320 nm, and 80 nm x 180 nm) easily transported

through the 200 nm porous membranes independent of modulus.<sup>30</sup> These optimizations in size, shape, and modulus have dramatic effects *in vivo* and are nevertheless useless without a potent therapeutic cargo.

New pharmacological drugs are often hydrophobic and poorly-soluble in aqueous media meaning they cannot be utilized *in vivo* without significant formulation. Formulation typically consists of adding a number of organic solvents or low molecular weight surfactants in order to effectively stabilize the drug prior to administration (Table 1.2).<sup>31</sup> As expected, these solubilizing excipients act as any small molecular weight compound: dispersing throughout the entire body, leading to systemic exposure, and resulting dose-limiting toxicities unrelated to the active pharmaceutical ingredient (API). Along with solubility, new pharmaceutical compounds are typically formulated to have a distinct drug-release profile depending on route-of-administration and indication. As with solubility formulation, release kinetics modification can be time-intensive and have significant monetary restrictions leading to impactful new drug entities never coming to market. Nanoparticle-based formulations have the capability of circumventing these issues.



Table 1.2 Common Excipients Used For Oral and Injectable Formulations<sup>31</sup>

Water-soluble	Water-insoluble	Surfactants
Dimethylacetamide (DMA)	Beeswax	Polyoxyl 35 castor oil (Cremophor EL)
Dimethyl sulfoxide (DMSO)	Oleic acid	Polyoxyl 40 hydrogenated castor oil (Cremophor RH 40)
Ethanol	Soy fatty acids	Polyoxyl 60 hydrogenated castor oil (Cremophor RH 60)
Glycerin	<i>d</i> - $\alpha$ -tocopherol (Vitamin E)	Polysorbate 20 (Tween 20)
<i>N</i> -methyl-2-pyrrolidone (NMP)	Corn oil mono-di-tridiglycerides	Polysorbate 80 (Tween 80)
PEG 300	Medium chain (C <sub>8</sub> /C <sub>10</sub> ) mono- and diglycerides	<i>d</i> - $\alpha$ -tocopheryl polyethylene glycol 1000 succinate (TPGS)
PEG 400	Long-chain triglycerides	Solutol HS-15
Poloxamer 407	Castor oil	Sorbitan monooleate (Span 20)
Propylene glycol	Corn oil	PEG 300 caprylic/capric glycerides (Softigen 767)
Hydroxypropyl- $\beta$ -cyclodextrin	Cottonseed oil	PEG 400 caprylic/capric glycerides (Labrasol)
Sulfobutylether- $\beta$ -cyclodextrin (Captisol®)	Olive oil	PEG 300 oleic glycerides (Labrafil M-1944CS)
$\alpha$ -cyclodextrin	Peanut oil	PEG 300 linoleic glycerides (Labrafil M-2125CS)
Phospholipids	Peppermint oil	Polyoxyl 8 stearate (PEG 400 monostearate)
Hydrogenated soy phosphatidylcholine (HSPC)	Safflower oil	Polyoxyl 40 stearate (PEG 1750 monostearate)
Distearoylphosphatidylglycerol (DSPG)	Sesame oil	Peppermint oil
L- $\alpha$ -dimyristoylphosphatidylcholine (DMPC)	Soybean oil	
L- $\alpha$ -dimyristoylphosphatidylglycerol (DMPG)	Hydrogenated soybean oil	
	Hydrogenated vegetable oils	
	Medium-chain triglycerides	
	Caprylic/capric triglycerides derived from coconut oil or palm seed oil	

Formulation of these APIs within a nano-carrier can overcome issues of stability and undesired drug release with relative ease and simultaneously improve PK/PD behavior. With nano-formulation, as long as the carrier exhibits solubility in the desired medium, the API will mirror that stability without solubilizing excipients. Nanotherapies hold the API within the matrix by one of two methods: chemical conjugation or physical entrapment and the release of API from the matrix is dependent on the method chosen. Upon particle administration, the API is usually kept within the blood compartment, therefore, minimizing the volume of distribution ( $V_d$ ). The  $V_d$  is reduced because the carrier cannot easily extravasate through the tightly-packed epithelial junctions in the blood vessels like traditional diffusion of small molecules. In consequence, deposition in off-target tissues is greatly diminished and a greater amount of the injected dose can reach the target tissue. Elimination half-life ( $t_{1/2}$ ) and overall exposure (area-under-curve; AUC) are typically improved as well since the API is kept in the plasma compartment.

The way in which the active therapeutic is coupled to the carrier is an important consideration when designing a nanoformulation. Covalent attachment between the carrier and cargo typically relies on a release mechanism to free the active therapeutic from the carrier. Along with the complexity of chemically modifying the API is the potential benefit of site-specific release. In numerous accounts throughout literature, cargo detachment has been shown to be initiated by both external (light, magnetic fields, and ultrasound) and physiological (pH and redox states) stimuli depending on the linker chemistry employed.<sup>32-36</sup> Extensive development of this linker can be undertaken so that the API not only releases at the target-site but also at the desired release rate. Ideally, the particulate should present minimal premature release of drug before it reaches the intended site, and sufficient release after it reaches the target, in effect, reducing systemic deposition and improving efficacy. While covalent linkage offers fine control of the cargo, complexity of these systems may defer some to simpler encapsulation methods.

Traditionally, physical entrapment of the API (encapsulation) is the most utilized method of therapeutic attachment due to the ease of formulation. PLGA, a biodegradable, biocompatible, and FDA-approved thermoplastic is the most prevalent material used for non-covalent encapsulation within nanoformulations. In this composition, hydrophobic drugs are loaded by polymeric entrapment or weak intermolecular interactions (such as van Der Waals, hydrogen-bonding, etc.), and rate of drug release is based upon matrix degradation, drug loading, and passive diffusion. Since release is largely diffusion-based, this method lacks precision for what environmental conditions elicit drug release and immediate burst release is typically observed upon administration. Polymer or lipid coatings can be used to overcome this burst release profile.<sup>37</sup> In the labs Dr. Andrew Wang, a cross-linkable lipid shell was developed to decrease the release rate of hydrophobic therapeutics from PLGA NPs. By altering the surface

functionality, slower drug release translated to improved efficacy; while NPs lacking a lipid shell showed no therapeutic benefit over the free drug.<sup>38</sup> In general, surface modification is possibly the easiest parameter to alter because it can be conducted post-particle fabrication, yet, the changes can translate to vastly improved behavior *in vivo*.

Surface modification of particulate delivery systems can aid in both passive and active targeting to cancerous tissue. Passively targeted particles are typically surface functionalized with stealthing agents, to allow for long circulation and thus accumulation through the EPR effect. Actively targeted particles are modified with targeting ligands used to recognize overexpressed receptors on the tumor cell surface (Figure 1.3).<sup>7</sup> As previously discussed, passive accumulation relies heavily on extending the elimination half-life, thus increasing the probability of accumulating within the target site. This is commonly achieved by grafting from, grafting to, or adsorbing polyethylene glycol (PEG) to the surface of nanoparticles (PEGylation). While other polymers show promise for surface passivation, such as zwitterionic coatings and sugar-based moieties, PEG remains the dominant choice due to its robust performance, ease of attachment, and market availability.<sup>39,40</sup> Altogether, effects of PEGylation are highly dependent on two interrelated parameters: the molecular weight (Mw) and surface density of the PEG coating. The density of PEG necessary to promote protein resistance and extend blood circulation varies drastically for different nanoparticle types and this will be discussed in greater detail in Chapter 2. While passivation remains the most utilized surface modification, active targeting has become a fixture in particle platforms.

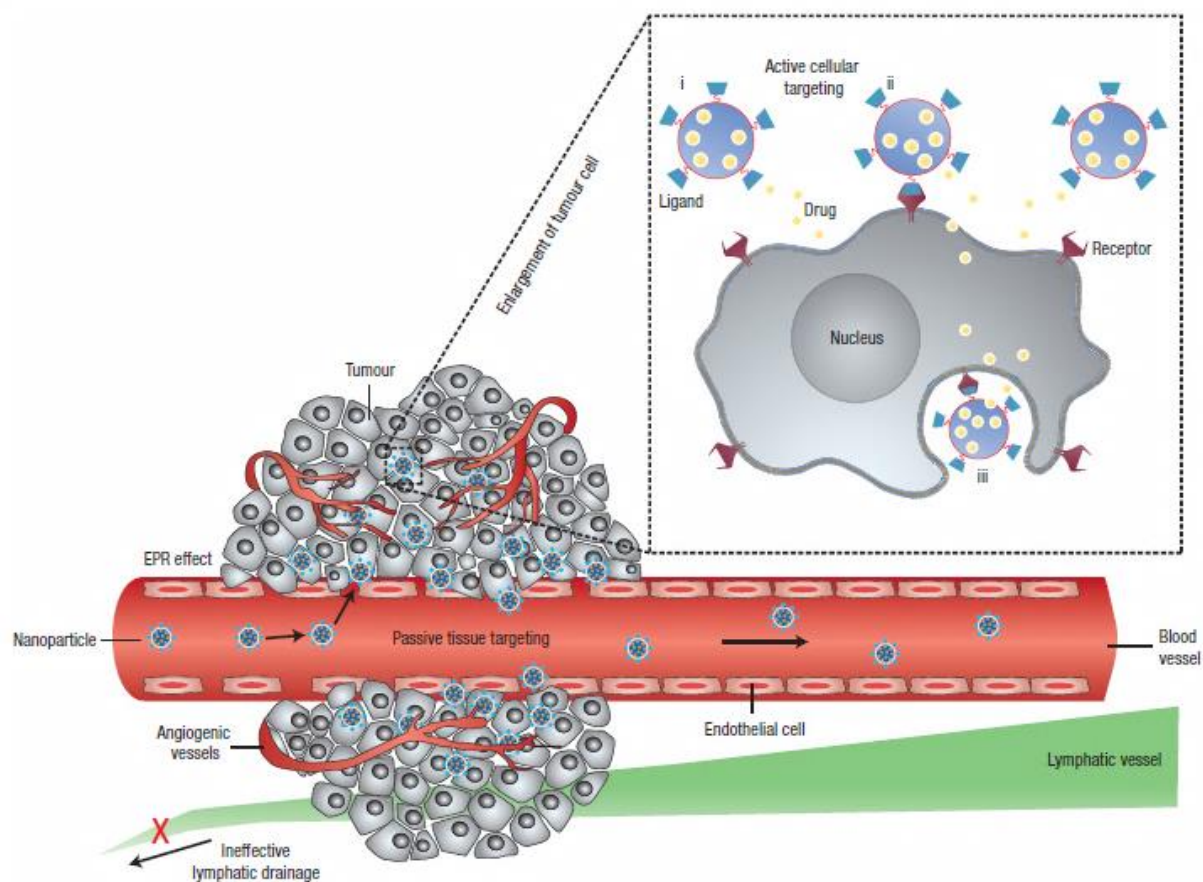


Figure 1.3 Active and passive accumulation mechanisms of a nanoparticle platform for cancer therapy.<sup>7</sup>

The “holy grail” in drug delivery is to transport a highly potent therapeutic to the diseased tissue, while completely eliminating exposure to off-target, healthy cells.<sup>41</sup> With active targeting, carriers are surface modified with ligands that bind precisely to unique overexpressed receptors on the diseased cell surface. There are a number of neoplastic cell receptors commonly targeted: epidermal growth factor receptor (EGFR), vascular endothelial growth factor (VEGF), and the human epidermal growth factor receptor 2 (HER-2) to name only a few.<sup>42,43</sup> The diversity of targeting agents is just as expansive as the receptors they are directed towards. Antibodies, affibodies, small molecules, peptides, and aptamers are just a sampling of targeting ligands that have been functionalized to nanoparticles delivery vehicles.<sup>42,44,45</sup> Engineering an actively targeted drug carrier can lead to preferential cell interactions within the diseased tissue,

enhanced cell uptake, and efficacy, however, creating an intricate carrier may come with unexpected consequences.

In reality, off-targeting to healthy cells persist due to innate expression of the target-receptor, albeit to a lesser extent. Dramatic shifts in blood PK, biodistribution, and efficacy have also been detected upon ligand attachment, and as with PEGylation, the surface density of targeting ligands plays a role in these systematic changes.<sup>45,46</sup> In one example, cytotoxicity was observed towards Ramos cells with an inert transferrin-targeted PRINT particles and the toxicity increased as a function of transferrin surface density. In this instance, enhancing multivalency (binding affinity associated with multiple ligand-receptor binding sites) produced unprecedented cell death for reasons not completely understood.<sup>47</sup>

The size and shape of the carrier can also influence targeting avidity. Theoretical work concluded that rod-like particles have greater probability to adhere to the target cell as compared to spherical particles.<sup>48</sup> Computational modeling reflected this by quantifying the increase in binding probability with increasing aspect ratio.<sup>49,50</sup> Experimentally, it was reported that rod-like NPs exhibit higher avidity/selectivity toward their target than their spherical analogs *in vivo* (Figure 1.4).<sup>51,17</sup> Similarly, actively targeting nanoworms enhanced multivalent interactions with cell receptors, which amplified their passive accumulation *in vivo* over spherical nanoparticle controls.<sup>52</sup>

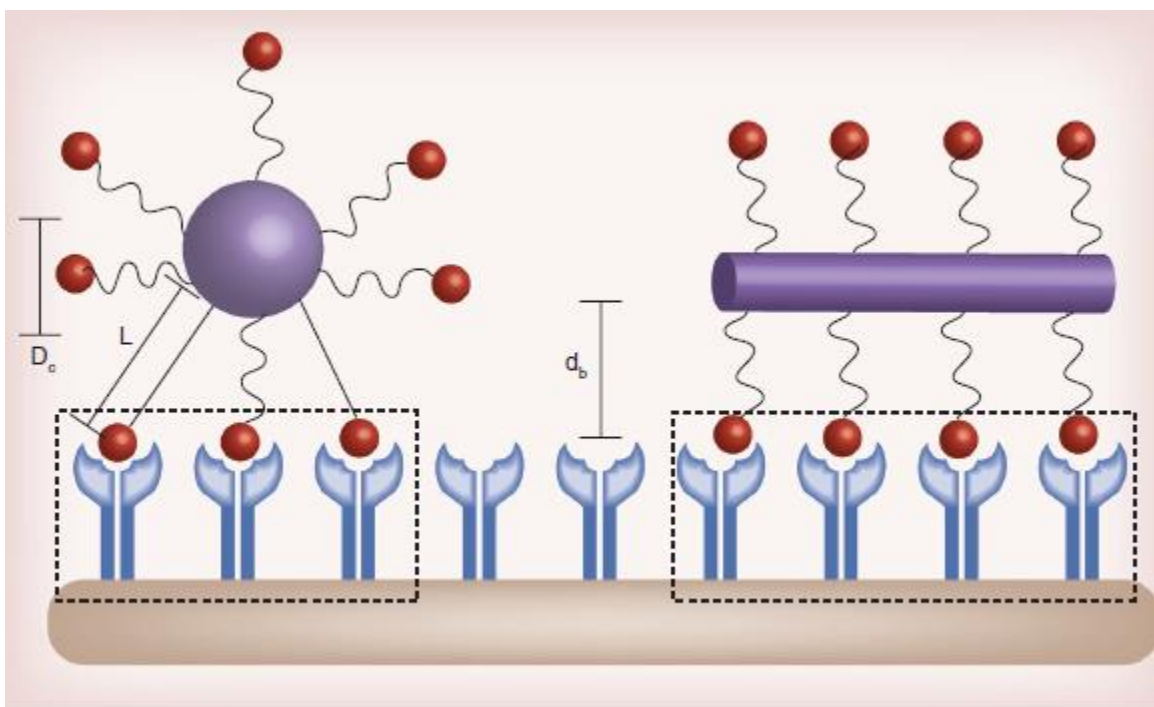


Figure 1.4 The role of nanoparticle shape in binding avidity between the ligand and the target receptor.<sup>17</sup>

Precision in particle fabrication is paramount when trying to accurately discern how changes in shape and size on the nanometer scale impact behavior upon *in vivo* administration. Most common nanoparticle types (liposomes, micelles, inorganic complexes), while being easier to scale and less expensive, sacrifice precise control of these parameters due to their nature of particle synthesis. The versatility of PRINT overcomes these limitations and allows independent control over particle parameters (size, shape, surface chemistry, modulus, etc.). PRINT has produced particles of compositions that range from pure protein to pure chemotherapeutic, moduli that span orders of magnitude, and sizes that vary from microns to nanometers, enabling the fabrication of a diverse library of NPs. This diversity is only made possible by the atypical top-down synthesis of PRINT nanoparticles.

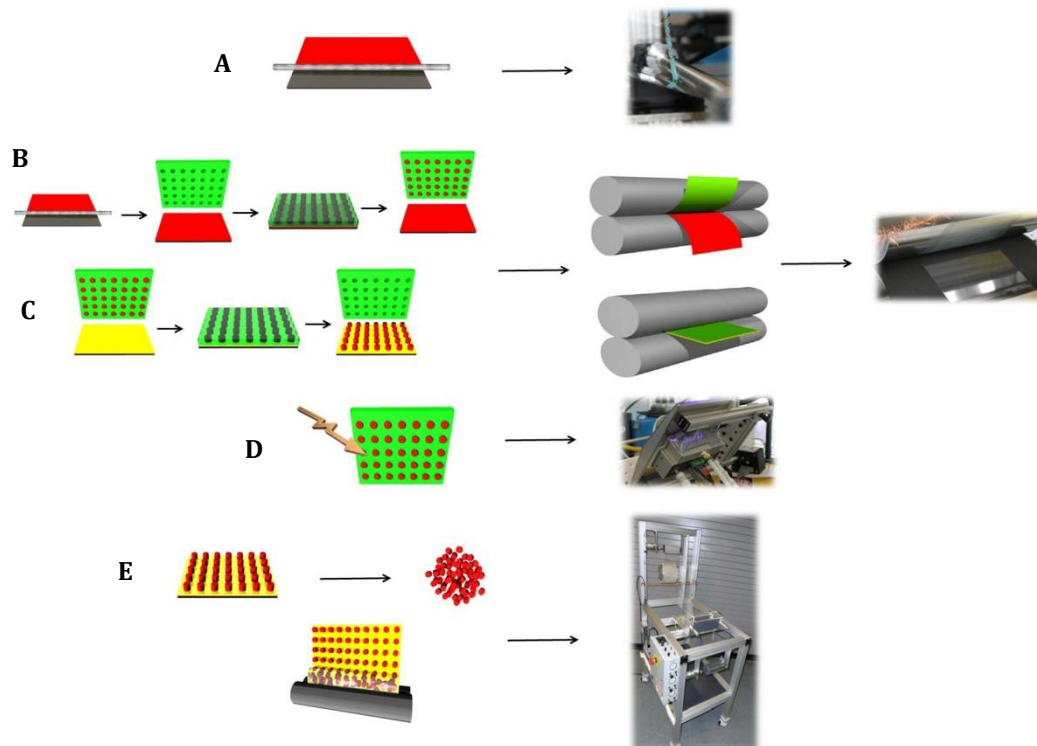
### 1.3 Nanoparticle Fabrication with PRINT Technology

Nanostructures are typically designed using one of two fabrication platforms. The “bottom-up” strategy uses atomic or molecular assembly creating macromolecular arrangements, the “top-down” strategy utilizes nanostructures fabricated by adding or removing material from a given surface. Lithography is one method of top-down fabrication in which nano-scale features can be etched onto a master template using similar technology found in the semiconductor industry. Particle Replication in Non-wetting Templates (PRINT) uses similar master templates and subsequently creates a Teflon-like negative template with distinct cavities of desired size and shape. With this mold one can control over particle shape, size, chemical composition, modulus, and surface chemistry. This versatility, coupled with its production of calibration-quality particles, has driven PRINT to the forefront of nanoparticle control.<sup>16,26,27,29,30,47,53</sup> The addition of a new roll-to-roll (R2R) machine has expanded the PRINT process into a high-throughput fabrication technique.

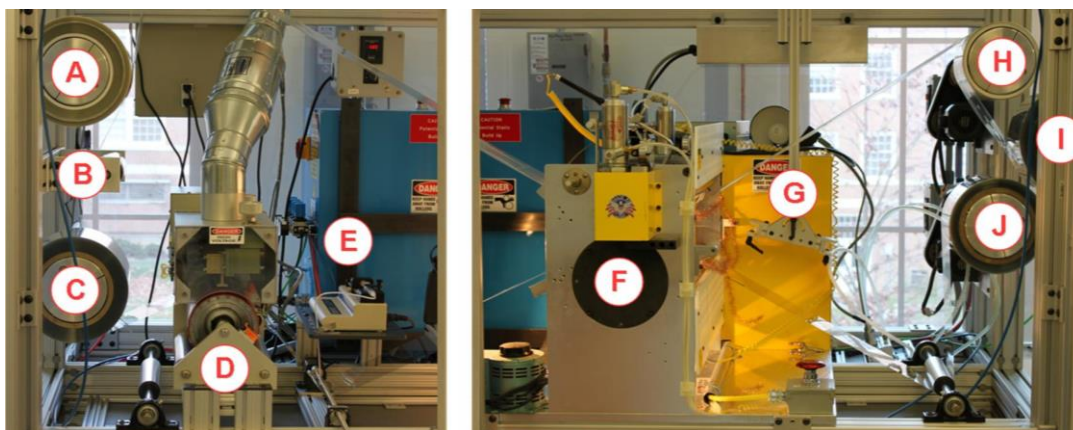
The R2R method takes the original batch PRINT process (Scheme 1.1) and transforms it to an “assembly-line” (Scheme 1.2), maximizing efficiency and yield. As previously mentioned, general PRINT fabrication utilizes a low surface energy mold constructed from a silicon master precursor. With the mold in hand, a polymeric solution is deposited onto a high surface energy polyethylene terephthalate (PET) sheet and the solvent is allowed to fully evaporate leaving a thin polymer film. The thin film is brought into conformal contact with the mold which is then passed through a pressurized nip. The nano-sized cavities are then filled with uncured liquid polymer via capillary action and, in the case of acrylate-based polymers, the filled mold is photo-cured with a high-intensity UV-LED oven. After curing, an array of isolated nanoparticles now fills the features in the mold with the absence of a flash-layer. The isolated nanoparticles are

harvested by means of a sacrificial adhesive film that is later dissolved with a common solvent (aqueous or non-aqueous), releasing free PRINT particles. These particles can finally be purified from the harvesting solution by simple centrifugation methods and put into a solvent of choice for future studies or post-fabrication surface modification.





Scheme 1.1 The roll-to-roll process incorporates each step in the fabrication process A) a Mayer rod and pre-particle solution (PPS) deposition controls film thickness onto a high surface energy PET delivery sheet B) a heated nip aids in transfer of the PPS to the low surface energy mold cavities and C) transfer to the harvesting sheet D) UV-LED photo-cures the PPS leading to polymerized nanoparticles E) R2R bead harvester allows for particle collection up to 5-6 ft/min in a compatible solvent.



Scheme 1.2 The novel roll-to-roll system allows for high-throughput PRINT NP fabrication. First, the mold (A), cover sheet collector (B), and PET delivery sheet (C) are strung up onto rollers. The delivery sheet passes through a plasma treater (D) and then PPS is dispensed by a syringe pump (E) onto the delivery sheet. The mold and delivery sheet are laminated with a heated nip (F) and the filled mold passes through a UV-LED (G). The delivery sheet waste (J) and filled mold (H) are collected on rollers while an optional adhesive layer is laminated to the mold (I).

## 1.4 References

1. Feynman, R.P. *Eng. Sci.* **1960**, 23(2), 22; *Sat. Rev.* **1960**, 43 (April 2), 45.
2. Matsumura, Y. and Maeda, H. *Cancer Res.* **1986**, 46, 6387-6392.
3. Cho, K.; Wang, X.; Nie, S.; Chen, Z.; and Shin, D. *Clin. Cancer Res.* **2008**, 14 (5), 1310-1316
4. Alexis, F.; Pridgen, E.; Molnar, L. K.; Farokhzad, O. C. *Mol. Pharmaceutics* **2008**, 5 (4), 505-515.
5. Singh, Inderbir. Textbook of Human Histology, 5<sup>th</sup> ed.; JP Medical Ltd.: New Delhi, 2003.
6. Nel, A. E.; Mädler, L.; Velegol, D.; Xia, T.; Hoek, E. M.; Somasundaran, P.; Klaessig, F.; Castranova, V. and Thompson, M. *Nat. Mater.* **2009**, 8, 543-557.
7. Peer, D.; Karp, J.M; Hong, S.; Farokhzad, O.C.; Margalit, R. and Langer, R. *Nat. Nano.* **2007**, 2, 751-760.
8. Albanese, A., P.S. Tang, and W.C.W. Chan, *Annu. Rev. Biomed. Eng.* **2012**, 14, 1-16.
9. Champion, J.A., Y.K. Katare, and S. Mitragotri. *J. Control. Release* **2007**, 121 (1-2), 3-9.
10. Champion, J.A.; Katare, Y. K. and Mitragotri, S. *PNAS* **2007**, 104 (29), 11901-11904.
11. Champion, J.A. and S. Mitragotri. *Pharm. Res.* **2009**. 26 (1), 244-249.
12. Carboni, E.; Tschudi, K.; Nam, J.; Lu, X. and Ma, A. *AAPS Pharm. Sci. Tech.* **2014**, 15 (3), 762-771.
13. Decuzzi, P.; Godin, B.; Tanaka, T.; Lee, S.; Chiappini, C.; Liu, X. and Ferrari, M. *J. Control. Release*, **2010**, 141 (3), 320-327.
14. Gentile, F.; Chiappini, C.; Fine, D.; Bhavane, R.C.; Peluccio, M. S.; Ming-Cheng Cheng, M.; Liu, X.; Ferrari, M. and Decuzzi, P. *J. Biomech.* **2008**, 41(10), 2312-2318.
15. Geng, Y.; Dalhaimer, P.; Cai, S.; Tsai, R.; Tewari, M.; Minko, T. and Discher, D. E. *Nat. Nano.* **2007**, 2 (4), 249-255.
16. Gratton, S.E.A., Ropp, P. A.; Pohlhaus, P. D.; Luft, J. C.; Madden, V. J.; Napier, M. E. and DeSimone, J. M. *PNAS*, **2008**. 105 (33), 11613-11618.
17. Toy, R.; Peiris, P. M.; Ghaghada, K. B. and Karathanasis, E. *Nanomedicine* **2014**, 9 (1), 121-134.

18. Perry, J. L.; Herlihy, K. P.; Napier, M. E. and DeSimone, J. M. *Acc. Chem. Res.*, **2011**, *44* (10), 990–998.
19. Moghimi, S. M.; Hunter, A. C. and Andresen, T. L. *Annu. Rev. Pharm. Tox.* **2012**, *52*, 481-503.
20. Decuzzi, P.; Lee, S.; Bhushan, B. and Ferrari, M. *Annals Biomed. Eng.* **2005**, *33* (2), 179-190.
21. Decuzzi, P.; Pasquanlini, R.; Arap, W. and Ferrari, M. *Pharm. Res.*, **2009**, *26*(1), 235-243.
22. Champion, J.A. and S. Mitragotri. *PNAS* **2006**, *103* (13), 4930-4934.
23. Sharma, G.; Valenta, D. T.; Altman, Y.; Harvey, S.; Xie, H.; Mitragotri, S. and Smith, W. *S. J. Control. Release*, **2010**, *147* (3), 408-412.
24. Arnida, M. M.; Ray, A.; Peterson, C. M. and Ghandehari. *Eur. J. Pharm. Biopharm.* **2011**, *77* (3), 417-423.
25. Chauhan, V.P.; Popovic, Z.; Chen, O.; Cui, J.; Fukumura, D.; Bawendi, M. G. and Jain, R. K. *Ange. Chemie-Int. Ed.* **2011**, *50*(48), 11417-11420.
26. Chu, K. S.; Hasan, W.; Rawal, S.; Walsh, M. D.; Enlow, E. M.; Luft, J. C.; Bridges, A. S.; Kuijter, J. L.; Napier, M. E.; Zamboni, W. C. and DeSimone, J. M. *Nanomed-Nanotechnol.* **2013**, *9* (5), 686-693.
27. Chu, K. S.; Schorzman, A. N.; Finniss, M. C.; Bowerman, C. J.; Peng, L.; Luft, J. C.; Madden, A. J.; Wang, A. Z.; Zamboni, W. C. and DeSimone, J. M. *Biomater.* **2013**, *34* (33), 8424-8429.
28. Hemant Sarin. *J. Angio. Res.* **2010**, *2* (14), 1-19.
29. Merkel, T. J.; Jones, S. W.; Herlihy, K. P.; Kersey, F. R.; Shields, A. R.; Napier, M.; Luft, J. C.; Wu, H. L.; Zamboni, W. C.; Wang, A. Z.; Bear, J. E.; DeSimone, J. M. *PNAS* **2011**, *108*, (2), 586-591.
30. Kersey, F.; Merkel, T. J.; Perry, J.; Napier, M. E. and DeSimone, J. M. *Langmuir* **2012**, *28* (23), 8773-8781.
31. Robert G. Strickley. *Pharm. Res.* **2004**, *21* (2), 201-230.
32. Bae, Y.; Fukushima, S.; Harada, A. and Kataoka, K. *Angew. Chem. Int. Ed.* **2003**, *42*(38), 4640-4643.
33. Bohmer, M.R.; Klibanov, A. L.; Tiemann, K.; Hall, C. S.; Gruell, H. and Steinbach, O. C. *Eur. J. Radiol.* **2009**, *70* (2), 242-253.

34. Caldorera-Moore, M.; Guimard, N.; Shi, L.; Roy, K. *Expert Opin. On Drug Delivery*, **2010**, 7 (4), 479-495.
35. Doshi, N. and S. Mitragotri. *Adv. Funct. Mater.* **2009**, 19(24), 3843-3854.
36. Ganta, S.; Devalapally, H.; Shahiwala, A.; Amiji, M. *J. Control. Release* **2008**, 126 (3), 187-204.
37. Makadia, H.K. and S.J. Siegel, *Polymers* **2011**, 3 (3), 1377-1397.
38. Sethi, M.; Sukumar, R.; Karve, S.; Werner, M. E.; Wang, E. C.; Moore, D. T.; Kowalczyk, S. R.; Zhang, L. and Wang . A. *Z. Nanoscale* **2014**, 6 (4), 2321-2327.
39. García, I.; Marradi, M. and Penadés, S. *Nanomed.* **2010**, 5 (5), 777-792.
40. García, K.P.; Zarschler, K.; Barbaro, L.; Barreto, J. A.; O'Malley, W.; Spiccia, L.; Stephan, W. and Graham, B. *Small* **2014**, 10 (13), 2516-2529.
41. Pirollo, K.F. and E.H. Chang, *Trends Biotechnol.* **2008**, 26 (10), 552-558.
42. Byrne, J. D.; Betancourt, T. and Brannon-Peppas, L. *Adv. Drug Deliver. Rev.* **2008**, 60, 1615-1626.
43. Lammers, T.; Kiessling, F.; Hennink, W. E, and Storm, G. *J. Control. Release* **2012**, 161 (2), 175-187.
44. Benhabbour, S. R.; Luft, J. C.; Kim, D.; Jain, A.; Wadhwa, S.; Parrott, M. C.; Liu, R.; DeSimone, J. M. and Mumper, R. J. *J. Control. Release* **2012**, 158 (1), 63-71.
45. Kamaly, N.; Xiao, Z.; Valencia, P. M.; Radovic-Moreno, A. F. and Farokhzad , O. C. *Chem. Soc. Rev.* **2012**, 41 (7), 2971-3010.
46. Hrkach, J. et al. *Sci. Transl. Med.* **2012**, 4 (128), 128-139.
47. Wang, J.; Tian, S.; Petros, R. A.; Napier, M. E. and DeSimone, J. M. *J. Am. Chem. Soc.* **2010**, 132 (32), 11306-11313.
48. Decuzzi, P. and M. Ferrari. *Biomaterials* **2006**, 27 (30), 5307-5314.
49. Shah, S.; Liu, Y.; Hu. W. and Gao, J. *J. Nanosci. Nanotechnol.* **2011**, 11 (2), 919-928.
50. Liu, Y., S. Shah, and J. Tan. *Rev. Nanosci. and Nanotech.* **2012**, 1(1), 66-83.
51. Kolhara, P.; Anselmob, A. C.; Guptab, V.; Pantc, K.; Prabhakarpanbianc, B.; Ruoslahtid, E. and Mitragotria, S. *PNAS* **2013**, 110 (26), 10753-10758.

52. Park, J. H.; Maltzahn, G.; Zhang, L.; Schwartz, M. P.; Ruoslahti, E.; Bhatia, S. N. and Sailor, M. J. *Adv. Mater.* **2008**, *20* (9), 1630-1635.
53. Rolland, J. P.; Maynor, B. W.; Euliss, L. E.; Exner, A. E.; Denison, G. E.; and DeSimone, J. M. *J. Am. Chem. Soc.* **2005**, *127*, 10096-10100.
54. Dexter, D. L.; Kowalski, H. M.; Blazar, B. A.; Zuzana, F.; Vogel, R. and Heppner, G. H. *Cancer Res.* **1978**, *38*, 3174-3181.
55. Gloria H. Heppner. *Cancer Res.* **1984**, *44*, 2259-2265.
56. Ringsdorf, Helmut. *J. Polymer Sci. Sym.* **1975**, *51*, 135-153.
57. Ambrose, E. J., Easty, D. M. and Jones, P. C. T. *Br. J. Cancer.* **1958**, *12*, 439-447.
58. McGuire, J. J. and Russell, C. A. *Leukemia* **1990**, *4*, 48-52.
59. Larsen, B. and Thorling, E. B. *Acta. Path. Microbiol. Scandinav.* **1969**, *75*, 229-236.
60. Saiki, I.; Murata, K.; Matsuno, K.; Ogawa, R.; Nishi, N.; Tokura, S. and Azuma, I. *Jpn. J. Cancer Res.* **1990**, *81*, 660-667.
61. Saiki, I.; Murata, J.; Nakajima, M.; Tokura, S. and Azuma, I. *Cancer Res.* **1990**, *50*, 3631-3637.
62. Zaharko, D. S. and Corey, J. M. *Cancer Treat. Rep.* **1984**, *68*, 1255.
63. Ardalan, B. and Paget, G. E. *Cancer Res.* **1986**, *46*, 5473-5476.
64. Rosenblum, M. G. and Hortobagyi, G. N. *Cancer Chemother. Pharmacol.* **1986**, *18*, 247-251.
65. Putnam, D. and Kopecek, J. *Advances in Polymer Science: Polymer Conjugates with Anticancer Activity*; Springer Verlag Berlin Heidelberg: New York. 1995
66. Schlipkoter, H.W. and Brockhaus, A. *Disch. Med. Wschr.* **1960**, *85*, 920-923.
67. Allison, A. C.; Harrington, J. S. and Birbeck, M. *J. Exp. Med.* **1966**, *124*, 141-143.

## CHAPTER 2 PEGYLATED PRINT NANOPARTICLES: THE IMPACT OF PEG DENSITY ON PROTEIN BINDING, MACROPHAGE ASSOCIATION, BIODISTRIBUTION, AND PHARMACOKINETICS<sup>1</sup>

### 2.1 Introduction

The full potential for nanotechnology has yet to surface even after decades of groundbreaking research. Nano-based drug delivery systems have produced advancements towards next generation cancer therapy (Doxil and Abraxane), but rapid elimination of nanoparticles (NPs) from the body continues to mitigate progress.<sup>1-4</sup> Following intravenous (IV) administration, NPs are rapidly removed from circulation and accumulate mainly in the liver and spleen, due to opsonization and recognition by the mononuclear phagocyte system (MPS).<sup>2, 5-7</sup> There have been many attempts to reduce uptake of nanoparticles by the MPS by controlling the physicochemical characteristics of the particles, such as size, surface charge, hydrophilicity and surface functionality.<sup>2,5,8-10</sup> Generally, nanoparticles that have a mean diameter of 200 nm or less, with a neutral to negative zeta potential, and an extended hydrophilic polymer surface exhibit prolonged blood circulation.<sup>2,5,10, 11</sup>

Poly(ethylene glycol) (PEG) has been extensively used on a variety of nanoparticle systems to increase surface hydrophilicity and improve circulation half-life by decreasing interactions with blood proteins and MPS cells.<sup>1,2,6,12-15</sup> PEGylation can be conducted with several unique techniques using di-block PEG derivatives, or by covalently attaching, entrapping, or adsorbing PEG chains onto the surface of a nanoparticle.<sup>1,6,14</sup> The effects of PEGylation are

---

<sup>1</sup> This chapter previously appeared as an article in Nano Letters. The original citation as follows: Perry, J. and Reuter, K. et al. Nano Lett. 2012, 12 (10), 5304-5310.

highly dependent on the PEG Mw, polymer chain architecture, and surface density of the PEG coating which leads to transitions in PEG conformations at the surface.<sup>13,14,16</sup> There is a general consensus that stealth properties can be achieved by coating with a high density of PEG, with MW ranging from 2k to 10k.<sup>14, 17-21</sup> In spite of PEG extending particle circulation in vivo, there is no general standard as to what surface density is needed to accomplish this goal. This stems partially from a lack of easy and efficient PEG quantification strategies.

A number of techniques are currently used to measure degree of PEGylation on NP surfaces, yet few have reported precise techniques for PEG quantification on polymeric NPs.<sup>7</sup> Most techniques described in literature are qualitative assessments of PEGylation such as NMR (PEG peak typically observed ~ 3.65 ppm), dynamic light scattering, and zeta-potential.<sup>22,23</sup> In some instances, PEG surface density is determined by simply assuming complete saturation of PEG on the surface of the nanoparticle, and therefore surface PEG density is reported based upon PEG size and nanoparticle surface area. For other nanoparticle formulations, PEG is incorporated into the nanoparticle matrix and PEG surface coverage is then based upon the weight or mole percent of the PEG incorporated – assuming that all the PEG chains are on the surface and not embedded within the particle.<sup>14</sup> Both of these methods typically offer an overestimation of PEG grafting. Few quantitative methods exist to accurately determine PEG surface density. Chromatography, such as size exclusion chromatography (SEC) and high performance liquid chromatography (HPLC), are well-documented quantitation techniques for PEGylated liposomes.<sup>6,24</sup> Thermogravimetric analysis (TGA) is used to calculate PEG weight, but is restricted to metallic NPs.<sup>25</sup> Surface plasmon resonance (SPR) is another method to determine PEG loadings with the caveat that quantification is generally characterized on flat substrates.<sup>7</sup> X-ray photoelectron spectroscopy (XPS) and Raman analyses can yield detailed information on

conformation and quantification, however, these methods are beyond typical analytical practices.<sup>7, 21</sup> Fluorescent assays are commonly used for rapid PEG quantification and are amenable for a variety of nanoparticle core compositions.<sup>7,24,26</sup>

PEGylation density is commonly described in terms of the conformation that surface-bound PEG chains achieve, which is based upon the Flory radius ( $R_F$ ) of the PEG graft, the distance ( $D$ ) between PEG grafts, or the length/thickness ( $L$ ) of the grafted PEG layer.<sup>7,27,28</sup> Based upon these parameters, there are two main conformations that PEG chains can acquire – ‘mushroom’ or ‘brush’.<sup>27,29,30</sup> Mushroom conformation is dictated by having a low density PEG coverage, where  $D > R_F$ , and therefore the PEG chains are not fully extended away from the nanoparticle surface, resulting in a thin PEG layer. As  $D$  decreases to that of  $R_F$ , PEG chains arrange in a brush conformation, with the PEG chains extending away from the nanoparticle surface, resulting in a thick layer. When  $L > 2R_F$ , the brush conformation was further defined by Damodaran et. al. to be a dense brush.<sup>31</sup> Thus by knowing the three parameters,  $D$ ,  $R_F$ , and  $L$ , the conformation of the PEG chain can be distinguished. Unfortunately, there is a disconnect throughout literature as to what parameters are reported. For ease of comparing degree of PEGylation, we have compiled data (Table 2.1) from the literature consisting of these key parameters and how they affect protein binding, macrophage uptake, and circulation half-life. Equations 2.1-2.8 were used to calculate unreported values (see methods section 2.4.5 for description of calculations). Based upon this compilation, it appears that the beneficial effects of PEGylation (protein and macrophage rejection and enhanced circulation half-life) occur when the PEG grafts are in the dense brush regime.



Table 2.1 Comparison of parameters used to determine surface PEG density on nanoparticles and their biological interactions.

PEG MW (g/mol)	R <sub>F</sub> (nm)	D (nm)	L (nm)	Regime	Protein Resistance	Macrophage Resistance	t1/2 (h)	REF
5K	5.96	3.2	8.80	Brush	NO	NO	-	14
5K	5.96	2.8	9.80	Brush	-	NO	-	46
5K	5.96	2.5	10.6	Brush	-	NO	0.3	39
3.4K	4.76	1.8	8.70	Brush	NO	-	-	55
2K	3.5	2.6	10.2	Dense Brush	-	YES	-	6
5K	5.96	2.2	11.5	Dense Brush	YES	YES	-	14
5K	5.96	2.0	12.4	Dense Brush	-	YES	-	46
5K	5.96	1.8	13.1	Dense Brush	-	YES	34.3	39
5K	5.96	1.7	13.5	Dense Brush	-	YES	6	19
3.4K	4.76	1.7	9.50	Dense Brush	YES	-	-	55
5K	5.96	1.3	16.6	Dense Brush	YES	YES	8.5	18
5K	5.96	0.98	20.0	Dense Brush	YES	YES	11.3	18

The aim of this study was to evaluate PRINT hydrogel nanoparticles (80 nm x 80 nm x 320 nm) with varying PEG surface coverage. PEG conformation was determined through standard plate-reader analysis of fluorescein-labeled PEG grafts. Herein we report predictive screening methods that can rapidly assess the circulation fate of our PEGylated PRINT nanoparticles. We explored the use of in vitro assays (protein binding and macrophage uptake) to predict in vivo circulation behavior. Intravital microscopy was used to quickly screen the circulation profiles of our particles, and a biodistribution study was conducted to look at long time points and confirm the results of in vitro assays.

## 2.2 Results and Discussion

### 2.2.1 Nanoparticle Fabrication, Surface Modification, and Characterization

We synthesized calibration quality 80 nm x 80 nm x 320 nm hydrogel particles with a narrow polydispersity index (PDI) on a continuous roll-to-roll lab line using the PRINT process (Figure 2.1). Utilizing this roll-to-roll method, PRINT particles were successfully made continuously at a rate of 360 mg/hour, which also resulted in highly uniform populations of particles. Particles were fabricated with amine functional handles (from the amino ethyl methacrylate), which were reacted with either a methoxy- or fluorescein-terminated PEG<sub>5k</sub>-succinimidyl carboxy methyl ester (PEG<sub>5k</sub>-SCM). PEG grafting density was controlled by varying the PEG<sub>5k</sub>-to-nanoparticle ratio, and was quantified by fluorescence measurements of the fluorescein-PEG<sub>5k</sub> labeled particles. The fluorescence signal was correlated to the concentration of fluorescein-PEG<sub>5k</sub> with a standard curve. PEG density was calculated based upon the concentration of particles in solution and the surface area of hydrated particles (equations can be found in supplementary information). PEG density was calculated to be  $0.083 \pm 0.006$  PEG/nm<sup>2</sup> and  $0.028 \pm 0.002$  PEG/nm<sup>2</sup> for the high and low PEG density NPs, respectively (Figure 2.2). In these calculations for PEG density, we assumed a uniform layer of PEG on the surface of the particle. Even though hydrogel particles swell, leading to possible penetration into the particle, it is entropically unfavorable for a large PEG molecule to permeate the hydrogel.

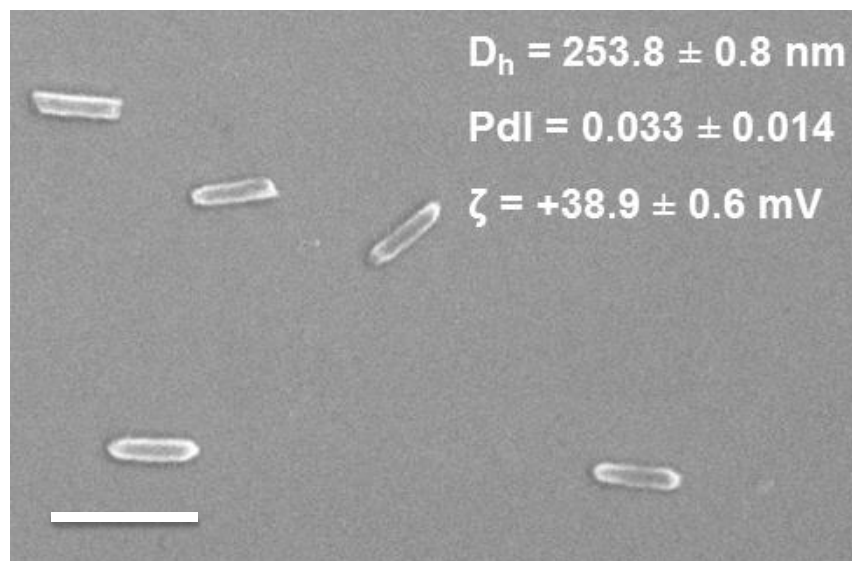


Figure 2.1 Scanning electron image of 80 nm x 80 nm x 320 nm PRINT hydrogel nanoparticles, scale bar represents 500 nm.

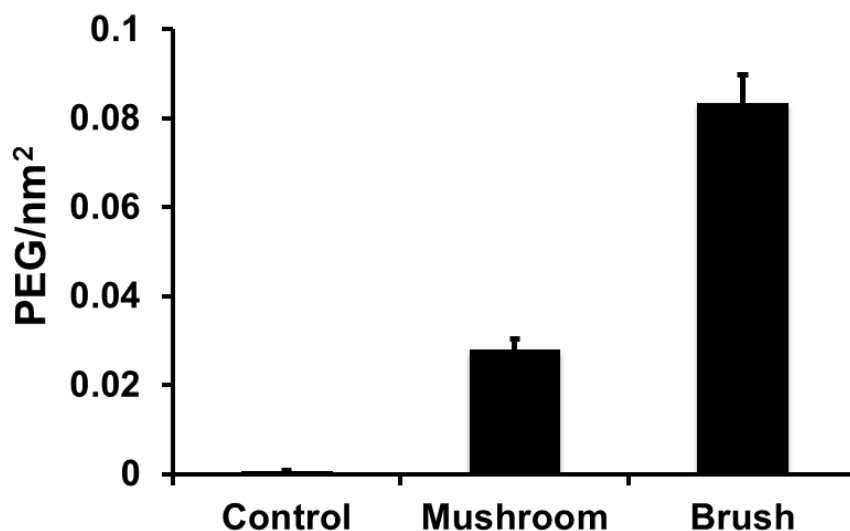


Figure 2.2 PEG density quantification of 80 nm x 320 nm particles reacted with 14.0 and 2.0 mg of fluorescein-PEG5k-SCM resulting in brush ( $0.083 \pm 0.006$  PEG / nm<sup>2</sup>) and mushroom ( $0.028 \pm 0.002$  PEGs / nm<sup>2</sup>) conformations, respectively (n = 6).

PEG density was converted to the area that one PEG chain occupies (A) and the distance between PEG graft sites (D) was calculated (Equation 2.3) to be 3.9 nm and 6.7 nm for the high and low PEG density particles, respectively.<sup>32</sup> As discussed in the introduction, the conformation of the PEG grafts is dictated by the relationship between D and  $R_F$ . The Flory radius (Equation 2.1) is determined by the number of monomers per polymer chain (N), and the length of one monomer ( $\alpha$ ).<sup>29</sup> For PEG<sub>5k</sub>,  $\alpha = 0.35$  nm and  $N = 113$ , therefore  $R_F = 5.96$  nm.<sup>33,34</sup> Based upon  $R_F$

and D, the PEG polymers were in the mushroom conformation for the low PEG density NPs and in the brush conformation for the high PEG density NPs (Figure 2.3). PEG brush thickness was calculated (Equation 2.2) to be  $7.9 \pm 0.1$  nm for high PEG density NPs. Based upon Damodaran criterion, the high PEG density NPs were not in the dense brush regime.<sup>31</sup> Hereafter, particles will be referred to as PEG mushroom and PEG brush NPs.

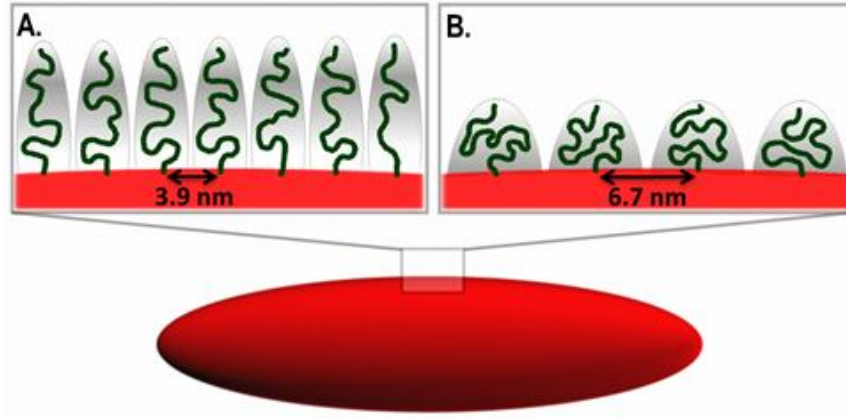


Figure 2.3 Cartoon representation of 80 nm x 80 nm x 320 nm PRINT hydrogel nanoparticles with functionalized PEG in brush (A) and mushroom (B) conformations.

Equation 2.1

$$R_F = aN^{\frac{3}{5}}$$

Equation 2.2

$$L = \frac{Na^{\frac{5}{3}}}{D^{\frac{2}{3}}}$$

Equation 2.3

$$D = 2 \sqrt{\frac{A}{\pi}}$$

For all of the *in vitro* and *in vivo* studies, particles were PEGylated using the same method outlined above but with a methoxy-PEG<sub>5k</sub>-SCM. Following PEGylation, the NPs were

acetylated to quench any remaining unreacted amines on the particle surface, resulting in particles with a slightly negatively zeta potential. The acetylation reaction was necessary because nanoparticles with positively charged surface groups typically exhibit higher protein adsorption and cell association than neutral or negative groups.<sup>35-37</sup> After acetylation, particles were characterized by dynamic light scattering (DLS) and degree of PEGylation was determined by fluorescence (Table 2.2). DLS was used to determine particle hydrodynamic diameter ( $D_h$ ), PdI, and zeta potential.  $D_h$  values listed in the table are not indicative of quantitative length scales and only act to compare relative trends between different particle types. Calculations for D and L were based upon measuring particle dimensions from SEM and AFM images.

Table 2.2 Nanoparticle characterization based upon dynamic light scattering

Sample	$D_h$ (nm) <sup>a</sup>	PdI <sup>a</sup>	$\zeta$ (mV) <sup>a</sup>	D (nm) <sup>b</sup>	L (nm) <sup>b</sup>
non-PEGylated	236.1 $\pm$ 4.4	0.063 $\pm$ 0.008	-27.9 $\pm$ 0.9	-	-
PEG mushroom	341.2 $\pm$ 5.3	0.101 $\pm$ 0.030	-8.15 $\pm$ 0.15	6.7 $\pm$ 0.3	5.5 $\pm$ 0.2
PEG brush	347.7 $\pm$ 7.7	0.042 $\pm$ 0.014	-11.6 $\pm$ 0.5	3.9 $\pm$ 0.1	7.9 $\pm$ 0.1

<sup>a</sup> Measured by dynamic light scattering

<sup>b</sup> Calculated from fluorescence analysis

### 2.2.2 Protein Binding and In Vitro Assays

It is well established that phagocytosis is facilitated by the adsorption of plasma proteins to NP surfaces, and that varying the surface chemistry of NPs can affect the identity and amount of proteins adsorbed.<sup>15,35,36,38-40</sup> One metric commonly used to characterize ‘stealth’ of PEGylated NPs is through *in vitro* classification including protein binding and/or macrophage uptake experiments.<sup>14,19,21,36,39-46</sup> In an effort to typify our PEGylated PRINT nanoparticles, we conducted a comprehensive study of protein binding and macrophage association on NPs with varying surface coverage of PEG.

Previous reports indicated that varying the surface chemistry of particles can affect both the identity and amount of proteins adsorbed.<sup>35,36,46</sup> Isothermal Titration Calorimetry (ITC) is the gold standard for measuring biomolecular interactions and has recently been utilized to determine nanoparticle-protein interactions.<sup>47-52</sup> Following a protocol by Lindman and co-workers, we used ITC to screen the effect that PEG conformation (mushroom vs. brush) had on protein adsorption.<sup>47</sup> We investigated the interaction of bovine serum albumin (BSA) with non-PEGylated, PEG mushroom and PEG brush NPs. BSA was chosen as a model protein because albumin is the most abundant protein in serum and is typically a major component in the protein corona surrounding nanoparticles.<sup>14,35,36,53,54</sup> The stoichiometry of proteins bound per nanoparticle was derived from a simple fit to the data of a one-site binding model using ORIGIN software (Figure 2.4). Figure 2.4 shows the amount of protein bound per particle significantly decreased with increasing surface PEG density. These results support previous findings where an increase in surface PEG density leads to decreased protein adsorption.<sup>14, 42, 43, 46, 55</sup> However, in comparison to literature, we are reporting protein rejection properties at much lower surface PEG density.<sup>14</sup>

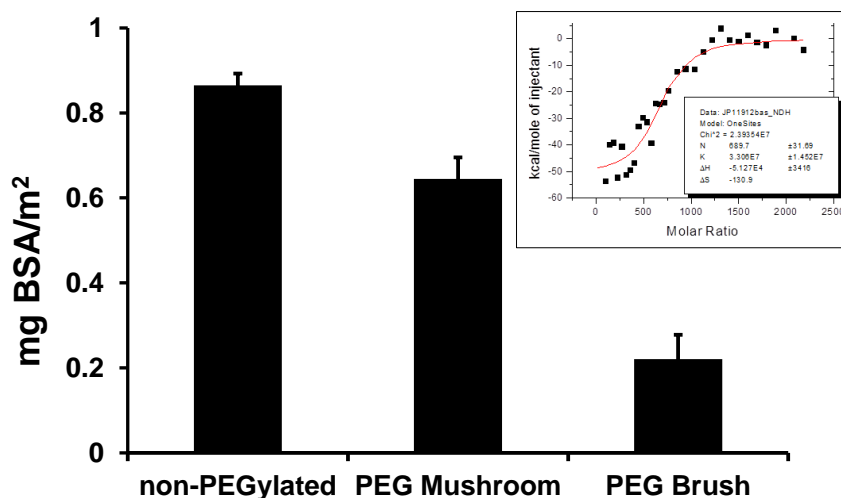


Figure 2.4 Mass of adsorbed BSA on non-PEGylated, PEG mushroom and PEG brush NPs (n = 3; insert is a representative image raw data collected from the isothermal titration calorimetry experiments).

The ITC studies clearly indicate that surface PEG density regulated the quantity of adsorbed BSA, therefore we hypothesized that it would also regulate the efficiency of macrophage uptake. To address macrophage association, nanoparticles were incubated in cell culture medium with the MH-S cells. Under these conditions, protein adsorption (from the cell culture medium) onto the surface of the nanoparticles can lead to cellular recognition by the macrophages and thus initiate uptake. We measured nanoparticle association with macrophages as a function of PEG surface density and time (Figure 2.5). At early time points (0.5 to 6 h) the PEG mushroom and PEG brush particles behaved the same and were associated with MP-S cells 4 to 14 times less than non-PEGylated NPs. After 24 h, a slight difference between the PEG mushroom and PEG brush NPs became evident. These findings are in agreement with literature; as PEG surface coverage increases both protein adsorption and macrophage association decreases.<sup>31,35,43,46</sup> However, as shown in Table 1, these protein/macrophage rejection properties are not typically observed until PEG grafts are in the dense brush regime, whereas we observed these properties for both PEG mushroom and PEG brush.

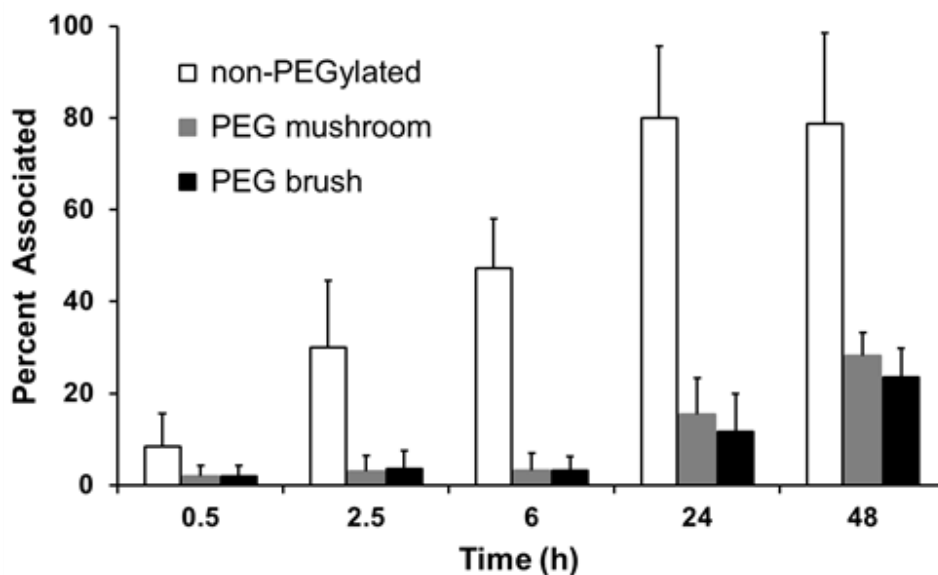


Figure 2.5 Percent of MH-S cells associated with non-PEGylated, PEG mushroom and PEG brush nanoparticles after various incubation times (n = 3).

### 2.2.3 Circulation and Biodistribution Evaluation

In an effort to translate *in vitro* data to circulation time *in vivo*, intravital microscopy (IVM) was utilized to track fluorescent nanoparticles in the ear vasculature of anesthetized mice over 2 h. Blood clearance curves of particles with varying surface PEG densities were generated from IVM fluorescence measurements (Figure 2.6). The data plot clearly indicates that PEGylation is essential for extending circulation times. Both mushroom and brush PEG particles appeared to have similar long-circulation profiles, whereas the non-PEGylated particles were cleared rapidly. These findings are in line with those observed from the macrophage assay, where the PEG mushroom and PEG brush NPs exhibited nearly identical association.

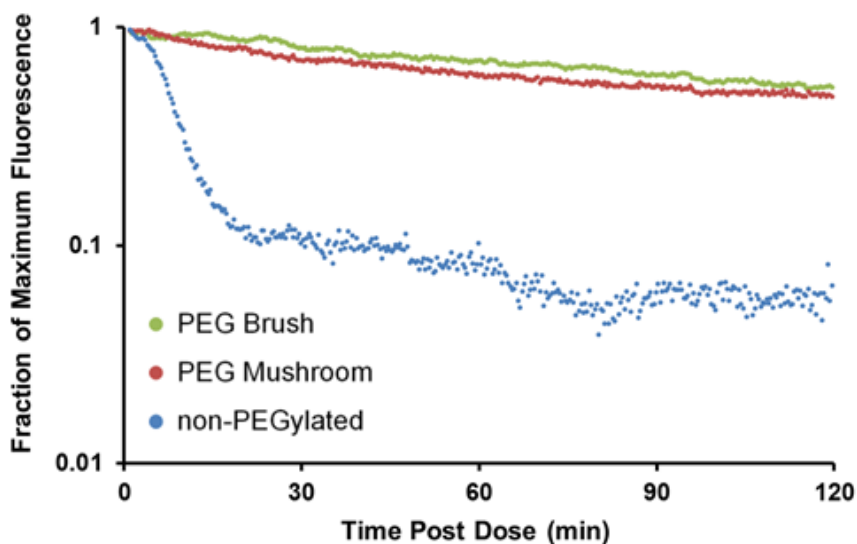


Figure 2.6 Intravital microscopy circulation profiles based upon fraction of maximum fluorescence remaining for non-PEGylated, PEG mushroom, and PEG brush nanoparticles.

In order to distinguish the difference between a mushroom and brush conformation, the concentration of particles in blood at longer time points was investigated. Mice were dosed with particles and sacrificed at certain time points extending out to 24 h. Figure 2.7 depicts blood circulation curves, with accompanying two-compartment PK model fits. The trend among the particle types closely follows that of the IVM profiles. The non-PEGylated particles exhibited



the same rapid clearance. However, further delineation between a mushroom and brush was displayed during the initial time points ( $> 3$  h), with a consistent difference at 24 h.

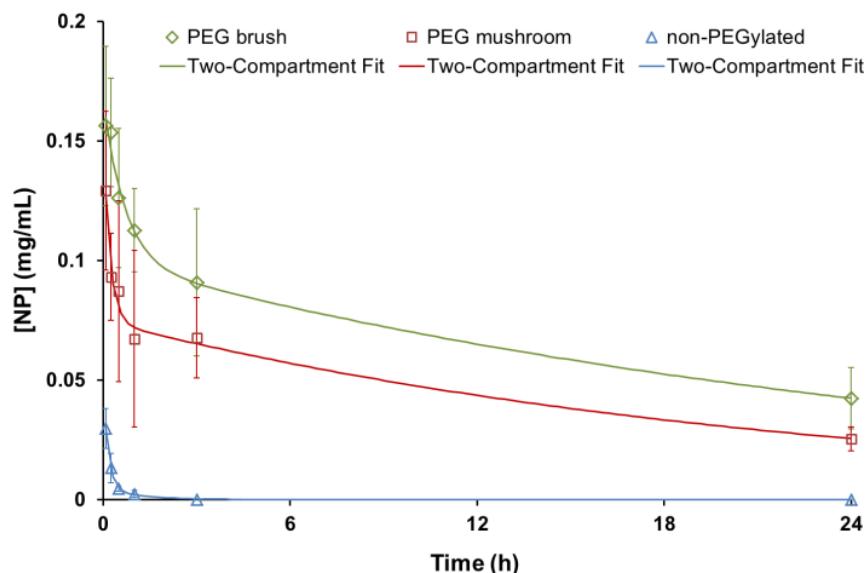


Figure 2.7 Concentration of nanoparticles in blood over time ( $n = 4$ ). Data is fit to a two-compartment PK model (solid lines)

Additionally, the MPS organs were resected and analyzed for particle fluorescence, to determine if organ accumulation was also dependent on surface PEG conformation. Figure 2.13 shows the organ accumulation as a function of PEG surface density at 24 h post-injection (organ accumulation at earlier time points in Figures 2.8-2.12). The blood concentration of non-PEGylated particles was undetectable at 24 h. Liver accumulation was high for all particle types, but showed decreased uptake as PEG density increased. Furthermore, as PEG density increased, so did splenic uptake. This has been observed for other PEGylated polymeric particles compared to non-PEGylated particles, where a shift from liver to splenic accumulation was observed.<sup>19, 56, 57</sup> It was hypothesized that longer circulation times allow more exposure of the particles to the spleen, resulting in higher splenic filtration and uptake by resident phagocytic cells.<sup>57</sup> Our data fits this theory, with a marked increase in splenic fluorescence between non-PEGylated and PEGylated particles, and a small increase as PEG density increased further. Thus, while

PEGylation increases circulation time via delayed phagocytosis, a particle's fate is ultimately the MPS organs.<sup>19</sup> While the exact mechanism is still unclear, this trend has been observed for over a decade with many particle sizes, shapes and compositions.<sup>1,5,14,30,58,59</sup> Finally, lung and kidney accumulation was minimal and likely attributed to fluorescence in residual blood within the organ.

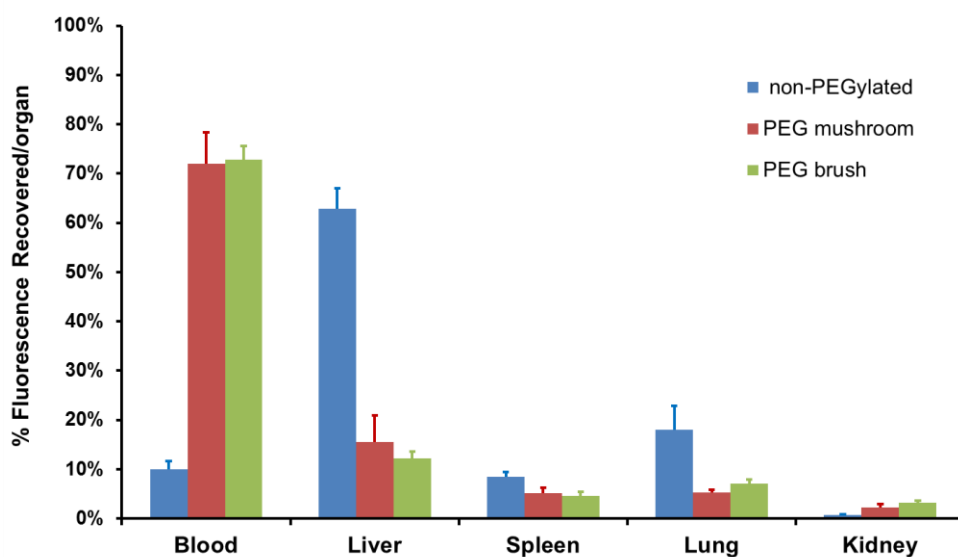


Figure 2.8 Biodistribution of nanoparticles at 0.083 h post-injection, expressed as percent recovered fluorescence per organ (n = 4).

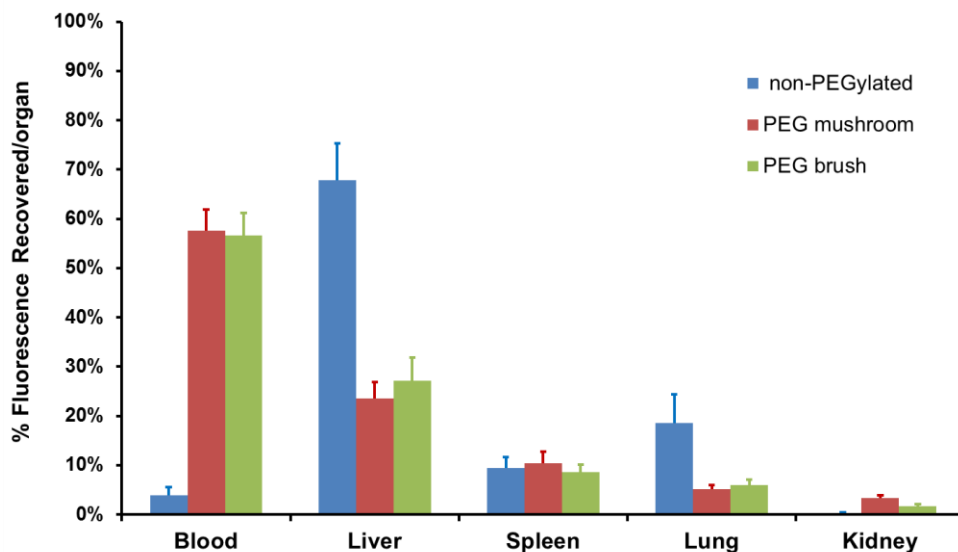


Figure 2.9 Biodistribution of nanoparticles at 0.25 h post-injection, expressed as percent recovered fluorescence per organ (n = 4).

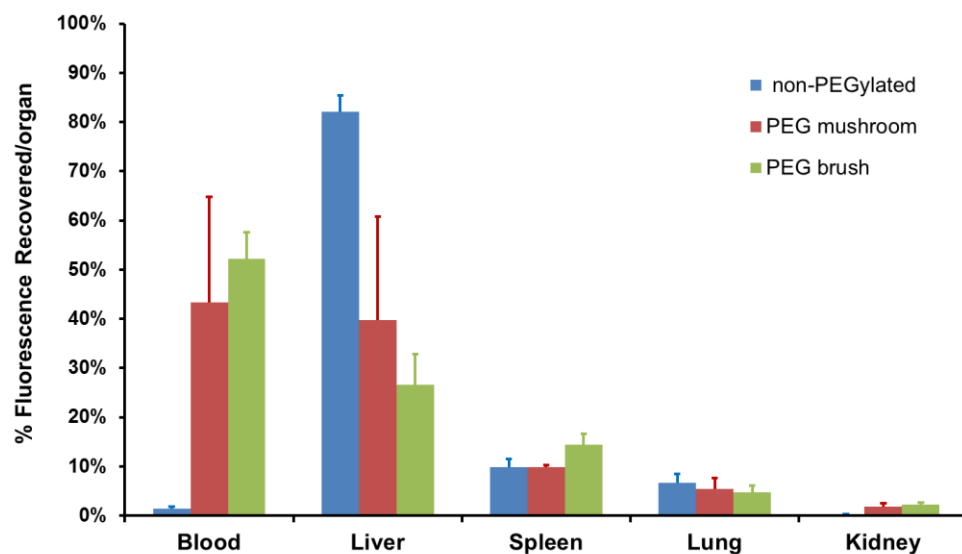


Figure 2.10 Biodistribution of nanoparticles at 0.5 h post-injection, expressed as percent recovered fluorescence per organ (n = 4).

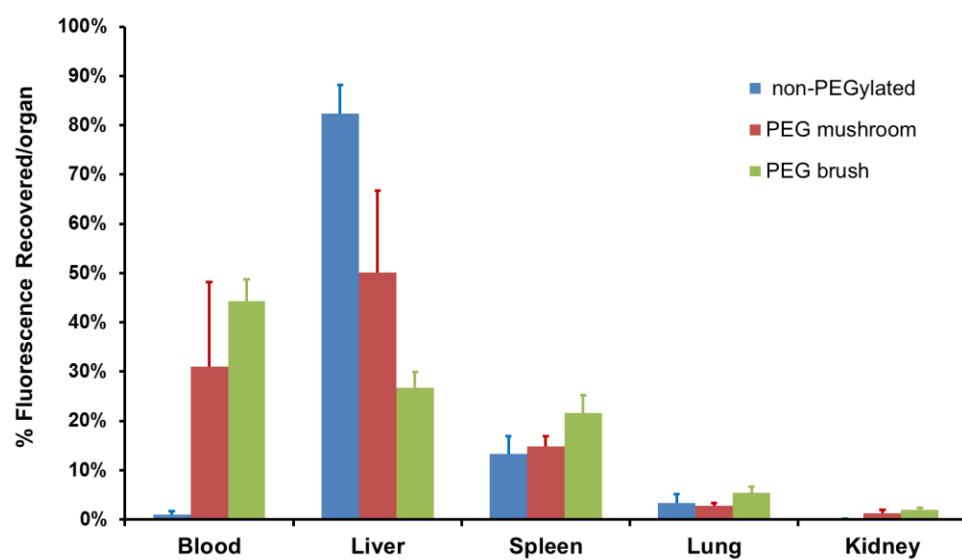


Figure 2.11 Biodistribution of nanoparticles at 1 h post-injection, expressed as percent recovered fluorescence per organ (n = 4).

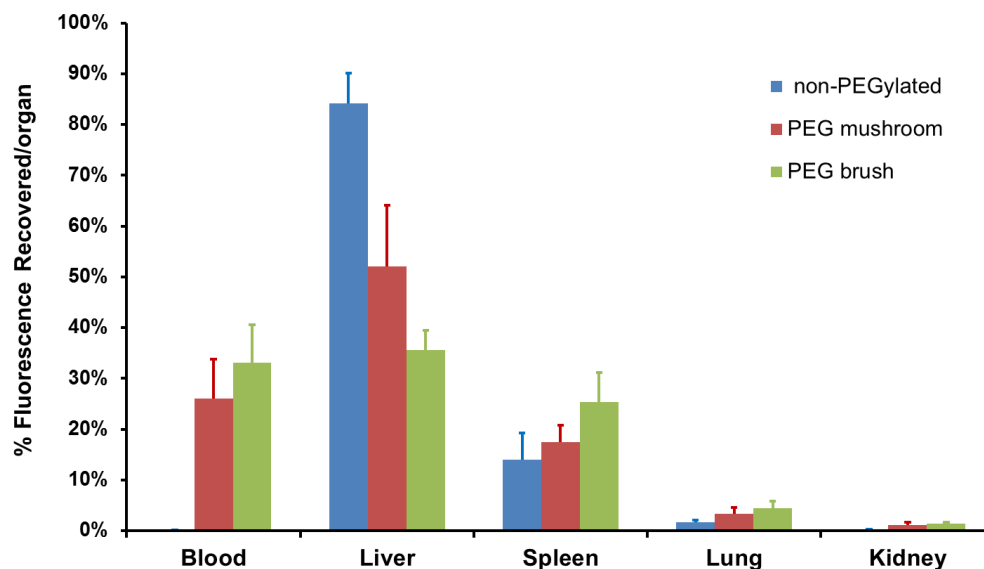


Figure 2.12 Biodistribution of nanoparticles at 3 h post-injection, expressed as percent recovered fluorescence per organ (n = 4).

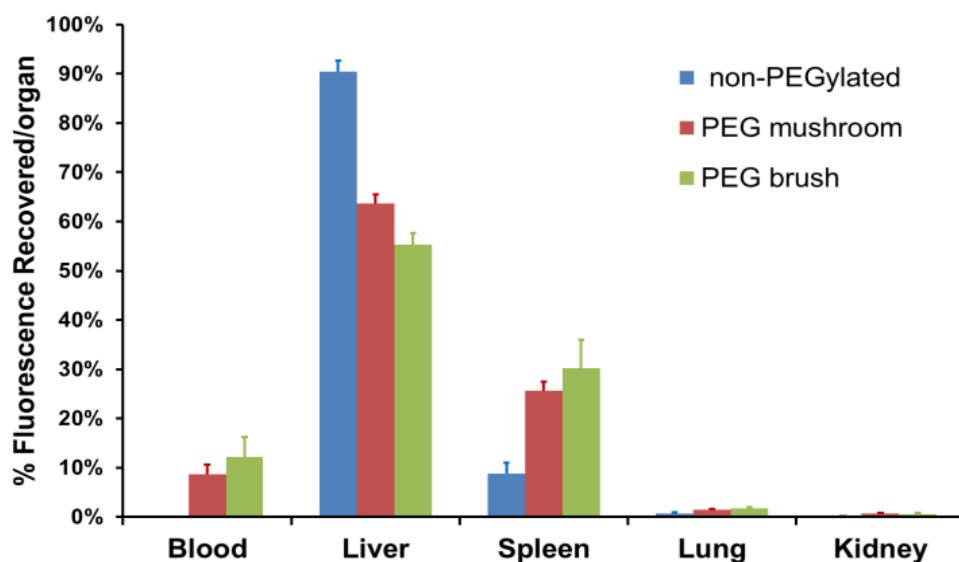


Figure 2.13 Biodistribution of nanoparticles at 24 h post-injection, expressed as percent recovered fluorescence per organ (n = 4).

Pharmacokinetic (PK) parameters were determined from the blood concentration curves for each particle type. Data was subjected to both one- and two-compartment analysis, with elimination from the central compartment, using PKSolver. A two-compartment model was found to be the best for all three particle types upon comparison of Akaike Information Criterion values. Table 2.3 lists the secondary parameters calculated from the primary constants of

integration from the two-compartment model. As suggested by IVM data, PEGylation clearly extends particle circulation on longer time scales. The half-life (beta-phase) increased from 0.89 h for non-PEGylated, to 15.5 h for PEG mushroom and 19.5 h for PEG Brush. Clearance and AUC (parameters important in drug delivery applications) also increased as PEG density increased. A PEG brush surface resulted in a 200-fold and 1.5-fold decrease in clearance versus a bare and PEG mushroom surface, respectively. Significant improvements in PK values upon PEGylation are widely cited in literature with similar results.<sup>14,57,59</sup> Furthermore, long-circulation half-lives are generally only observed for NPs with a dense PEG brush surface. Again, we have shown these same improvements for NPs with PEG mushroom and brush surfaces.

Table 2.3 Pharmacokinetic parameters from two-compartment model fit of blood concentration data.

	$t_{1/2, \alpha}$ (h)	$t_{1/2, \beta}$ (h)	CL (mL/h)	$V_d$ (mL)	$AUC_{0-t}$ (h*mg/mL)
non-PEGylated	0.116	0.892	17.5	4.75	0.013
PEG mushroom	0.144	15.5	0.128	1.40	1.12
PEG brush	0.478	19.5	0.087	1.48	1.66

Table 2.4 Constants of integration from two-compartmental model fit of blood concentration data with coefficient of determination ( $R^2$ ).

	A	$\alpha$	B	$\beta$	$R^2$
non-PEGylated	0.042	5.98	0.004	0.777	0.9996
PEG mushroom	0.080	4.82	0.075	0.045	0.9977
PEG brush	0.068	1.45	0.100	0.036	0.9990

### 2.3 Conclusions

We have developed a method for fabricating calibration quality hydrogel nanoparticles via a continuous process. This allowed us to conduct comprehensive *in vitro* and *in vivo* studies

using highly uniform populations of particles and to fully characterize how NPs behave as a function of surface PEG density. PEG density was varied using a highly tunable method that could easily be quantified by fluorescence. Protein adsorption and macrophage association were significantly reduced upon PEGylation of the NPs. An increase in PEG density, resulting in a conformation change from mushroom to brush, showed slight improvements in these *in vitro* studies. Extended circulation due to PEGylation was confirmed using IVM, with both PEGylated particles behaving similarly. Furthermore, a larger difference in behavior between the two regimes became evident through PK and biodistribution analysis. PEGylation resulted in at least a 17-fold increase in circulation half-life, a 136-fold decrease in clearance, and an 86-fold increase in AUC over non-PEGylated NPs. In conclusion, we show significant improvement in overall particle behavior with lower PEG densities than previously reported.

## 2.4 Materials and Methods

### 2.4.1 Materials

Poly(ethylene glycol) diacrylate ( $M_n$  700) (PEG<sub>700</sub>DA), 2-aminoethyl methacrylate hydrochloride (AEM), diphenyl (2,4,6-trimethylbenzoyl)-phosphine oxide (TPO), bovine serum albumin (BSA) protein standards (2 mg/mL), trypsin, ethylenediametetraacetic acid (EDTA), and sucrose were purchased from Sigma-Aldrich. Thermo Scientific Dylight 488, 650 and 680 maleimide, Thermo Scientific HyClone fetal bovine serum (FBS), PTFE syringe filters (13 mm membrane, 0.22  $\mu$ m pore size), dimethylformamide (DMF), triethylamine (TEA), pyridine, sterile water, borate buffer (pH 8.6), Dulbecco's phosphate buffered saline (PBS) (pH 7.4), 1X phosphate buffered saline (PBS) (pH 7.4), acetic anhydride, and methanol were obtained from Fisher Scientific. Fluorescein-PEG(5k)-succinimidyl carboxy methyl ester (fluorescein-PEG<sub>5k</sub>-SCM) and methoxy-PEG(5k)-succinimidyl carboxy methyl ester (mPEG<sub>5k</sub>-SCM) were

purchased from Creative PEGWorks. Conventional filters (2  $\mu\text{m}$ ) were purchased from Agilent and polyvinyl alcohol (Mw 2000) (PVOH) was purchased from Acros Organics. PRINT molds (80 nm x 80 nm x 320 nm) were obtained from Liquidia Technologies. Tetraethylene glycol monoacrylate (HP<sub>4</sub>A) was synthesized in-house as previously described.<sup>60</sup> Murine alveolar macrophage (MH-S) cells were purchased from American Type Culture Collection.

#### 2.4.2 Nanoparticle Fabrication

The PRINT particle fabrication technique has been described previously in detail.<sup>61</sup> The pre-particle solution was prepared by dissolving 3.5 wt% of the various reactive monomers in methanol. The reactive monomers included: a cure-site monomer (an oligomeric PEG with a nominal molar mass of 700 g/mol terminally functionalized on both end groups with an acryloxy functionality); a hydrophilic monomer used to make up the majority of the particle composition (HP<sub>4</sub>A); an amine containing monomer (AEM) which served to provide the amine functionality used to conjugate PEG onto the surface of the PRINT particles; and in some cases a polymerizable fluorescent tag. In all cases a photoinitiator, TPO, was also added. Two different pre-particle solutions were used throughout the following studies. For quantifying PEG density and ITC studies the pre-particle solution was comprised of 68 wt% HP<sub>4</sub>A, 20 wt% AEM, 10 wt% PEG<sub>700</sub>DA, and 1 wt% TPO. For the remainder *in vitro* and *in vivo* studies, the pre-particle solution was comprised of 67.5 wt% HP<sub>4</sub>A, 20 wt% AEM, 10 wt% PEG<sub>700</sub>DA, 1 wt% TPO and 1.5 wt% Dylight maleimide (either 680, 650 or 488). Using a # 3 Mayer rod (R.D. Specialties), a thin film of the pre-particles solution was drawn onto a roll of freshly corona treated PET, using a custom-made roll-to-roll lab line (Liquidia Technologies) running at 12 ft/min. The solvent was evaporated from this delivery sheet by exposing the film to a hot air dam derived from heat guns. The delivery sheet was laminated (80 PSI, 12 ft/min) to the patterned side of the mold, followed

by delamination at the nip. Particles were cured by passing the filled mold through a UV-LED (Phoseon, 395 nm, 3 SCFM N<sub>2</sub>, 12 ft/min). A PVOH harvesting sheet was hot laminated to the filled mold (140 °C, 80 PSI, 12 ft/min). Upon cooling to room temperature, particles were removed from the mold by splitting the PVOH harvesting sheet from the mold. Particles were then harvested by dissolving the PVOH in a bead of water (1 mL of water per 5 ft of harvesting sheet). The particle suspension was passed through a 2 µm filter (Agilent) to remove any large particulates. To remove the excess PVOH, particles were centrifuged (Eppendorf Centrifuge 5417R) at ca. 21,000 g for 15 min, the supernatant was removed and the particles were re-suspended in sterile water. This purification process was repeated 4 times.

#### 2.4.3 Nanoparticle Characterization

Stock particle concentrations were determined by thermogravimetric analysis (TGA) using a TA Instruments Q5000 TGA. TGA analysis was conducted by pipetting 20 µL of the stock nanoparticle solution into a tared aluminum sample pan. Samples suspended in water were heated at 30 °C/min to 130 °C, followed by a 10 minute isotherm at 130 °C. Samples suspended in DMF were heated at 30 °C/min to 170 °C, followed by a 10 minute isotherm at 170 °C. All samples were then cooled at 30 °C/min to 30 °C, followed by a 2 minute isotherm at 30 °C. TGA was also performed on a 20 µL aliquot of supernatant from a centrifuged sample of the stock nanoparticle solution to account for the mass of any stabilizer remaining in each sample. The concentration of stabilizer was subtracted from the concentration of stock particle solution to determine the actual particle concentration. Particles were visualized by scanning electron microscopy (SEM) using a Hitachi S-4700 SEM. Prior to imaging, SEM samples were coated with 1.5 nm of gold-palladium alloy using a Cressington 108 auto sputter coater. Particle size



and zeta potential were measured by dynamic light scattering (DLS) on a Zetasizer Nano ZS (Malvern Instruments, Ltd.).

Swelling of the particles in an aqueous environment was analyzed using fluid atomic force microscopy (AFM) with an Asylum Research MFP-3D atomic force microscope at room temperature. Height, phase, and amplitude images were acquired in water, in tapping mode, with a silicon nitride cantilever (Budget Sensors,  $k = 0.06$  N/m) at a scan rate of 1 Hz. Samples for imaging were prepared by pipetting particle suspension onto a clean glass slide. The solution was allowed to evaporate in an effort to settle the nanoparticles onto the glass slide. A droplet of water was then placed upon the dried nanoparticles to re-hydrate them. A droplet of water was also placed upon the AFM tip. The two droplets were merged and images collected. The hydrated dimensions of the particles were then determined from the AFM images.

#### 2.4.4 PEGylation Quantification

After purification, the particles were reconstituted in DMF following the centrifugation technique outlined above and the concentration of particles in DMF was determined by TGA. The particles fabricated contain free primary amine groups which were used as functional handles to react with a fluorescein-PEG<sub>5k</sub>-SCM. The particles (1 mg NPs in 1 mL DMF) were reacted with TEA (100  $\mu$ L) for 10 min at room temperature on a shaker plate (Eppendorf, 1400 rpm). The fluorescein-PEG<sub>5k</sub>-SCM was dissolved in DMF and added to the reaction mixture (14 mg and 2 mg of fluorescein-PEG<sub>5k</sub>-SCM for high and low PEG density, respectively). A deactivated fluorescein-labeled NHS-PEG via addition of ethanolamine was utilized as a negative control. The reaction mixture was shaken overnight and then quenched with borate buffer (100  $\mu$ L). The nanoparticle solution was then washed 5 times with DMF via centrifugation. The PEGylated particles were characterized by SEM, DLS, and TGA. After conjugating

fluorescently-tagged PEG<sub>5k</sub> to the nanoparticle surface, the amount of PEG bound to the particle was assessed via fluorescence measurements. The fluorescein-PEG-NP solution was diluted 1:10 in borate buffer and pipetted (200 µL) into a Corning 96-well clear bottom plate in triplicate. The supernatant from the same nanoparticle solution was added to the 96-well plate using the same method. A serial dilution of unconjugated fluorescent-PEG<sub>5k</sub> was utilized to create a standard curve. Fluorescence measurements ( $\lambda_{\text{ex}} = 494 \text{ nm}$ ;  $\lambda_{\text{em}} = 521 \text{ nm}$ ) of the 96-well plate containing the (1) PEGylated nanoparticle (2) supernatant and (3) standard curve were taken using a SpectraMax M5 plate-reader. The fluorescence in the supernatant was subtracted from the fluorescence observed from the nanoparticle suspension and the final fluorescence measurement was correlated to fluorescein-PEG<sub>5k</sub> concentration through the standard curve.

#### 2.4.5 PEG Density Calculations

PEG density was calculated based upon the concentration of particles in solution and the surface area of hydrated particles. First, we calculated the total number of PEG molecules and nanoparticles in each sample. The number of PEG molecules was calculated from the standard curve. The number of NPs was calculated using Equation 2.4, where the mass of NPs per well ( $m$ ) was determined by TGA, the density of the nanoparticle ( $\rho_{\text{NP}}$ ) is  $1.1 \text{ g/cm}^3$  and the volume ( $V$ ) determined by measurements from SEM images. Equation 2.5 was used to calculate PEG density ( $S$ ), where the surface area ( $SA_{\text{NP}}$ ) of a hydrated  $80 \text{ nm} \times 320 \text{ nm}$  nanoparticle was measured by fluid AFM. The area occupied by each PEG chain ( $A$ ) is defined by Equation 2.6. Assuming that PEG occupies a circular footprint on the particle surface, the distance between PEG grafts ( $D$ ) can be calculated using Equation 2.3.

Equation 2.4

$$\#NPS = \frac{m}{\rho_{\text{NP}} V_{\text{NP}}}$$

Equation 2.5

$$S = \frac{\# \text{ PEGs}}{SA_{NP}}$$

Equation 2.6

$$A = \frac{1}{S}$$

In order to calculate unreported values from referenced literature as seen in Table 1, a number of equations were utilized. Equation 2.7 was used explicitly to calculate the area occupied per PEG chain (A) for PLGA nanoparticles, where  $M_{PEG}$  is the molecular weight of the PEG graft,  $f$  is mass fraction of PEG in the particle,  $\rho$  is the density of the nanoparticle,  $N_A$  is Avogadro's number, and  $d$  is the diameter of the particle.<sup>14</sup> Using this value for A, D was then calculated using Equation 2.3. Equation 2.8 was used only to calculate D for liposomal particles.<sup>6</sup> For this equation  $A_{lipid}$  is the area occupied per lipid and  $m$  is the mole fraction of PEG incorporated in the nanoparticle.<sup>28</sup> For all other nanoparticles listed in Table 1, Equations 2.1-2.3 were used.

Equation 2.7

$$A = \frac{6M_{PEG}}{dN_A f \rho}$$

Equation 2.8

$$D = \sqrt{\frac{A_{lipid}}{m}}$$

#### 2.4.6 PEGylation and Acetylation for *In Vitro* and *In Vivo* Studies

For *in vitro* and *in vivo* studies, particles were PEGylated using the same procedure outlined above. However, instead of a fluorescein-PEGK<sub>5K</sub>-SCM, a methoxy-PEG<sub>5K</sub>-SCM was used. Following PEGylation, particles were acetylated with acetic anhydride to quench any unreacted amines and to yield a negative zeta potential. For acetylation, nanoparticles (1 mg NP

in 1 mL DMF) were reacted with an excess (10  $\mu$ L) of pyridine and acetic anhydride (7  $\mu$ L). The reaction was carried out in a sonicator bath (Branson Ultrasonic Cleaner 1.4 A, 160 W) for 15 min, after which a second addition of acetic anhydride (7  $\mu$ L) was added and the suspension was sonicated for another 15 min. Following acetylation, the particles were washed by centrifugation one time in DMF, followed by a borate buffer wash to neutralize any acetic acid side product, and then 4 washes with sterile water. Post-acetylation, particles were analyzed by TGA, DLS and SEM.

#### 2.4.7 Protein Binding Using Isothermal Titration Calorimetry

The isothermal titration calorimetry (ITC) experiments were performed at 37 °C, using a VP-ITC microcalorimeter (GE MicroCal Inc., USA). Experiments were performed by injecting 20  $\mu$ M solution of BSA in 1X PBS into a 2 mL sample cell containing nanoparticles at a concentration of 2 mg/mL in 1X PBS with a stirring speed of 300. A total of 44 injections were performed with a spacing of 240 s and a reference power of 10  $\mu$ cal/s. Titration volumes of BSA were as follows: a first injection of 2  $\mu$ L, followed by twenty eight injections of 5  $\mu$ L, and fourteen injections of 10  $\mu$ L. Binding isotherms were plotted and analyzed using Origin Software (MicroCal Inc., USA), where the ITC measurements were fit to a one-site binding model.

#### 2.4.8 Macrophage Association Assay

Murine alveolar macrophage cells (MH-S) were used to investigate the uptake of nanoparticles as a function of surface PEG density. MH-S cells were plated at a density of 40,000 cells per well in a 24-well plate and were incubated at 37°C for 24 hours. Following 24 h, the dye-labeled (Dylight 650 or 680) nanoparticle samples (20  $\mu$ g in 1 mL water) were incubated with the cells for 0.5, 2.5, 6, 24, and 48 h. At the set time points, cells were washed three times with 500  $\mu$ L 1X PBS and detached by the addition of 1X trypsin/EDTA (300  $\mu$ L) to each well.

Following a 5 minute incubation (37°C), 1X DBPS/10% FBS (500 µL) was added to each well and was mixed vigorously. This final solution was then transferred to a polypropylene tube and analyzed using a Dako CyAn flow cytometer with excitation and emission filters set to match that of the fluorescent dye incorporated into the particles. For each sample, 10,000 cells were measured.

#### 2.4.9 In Vivo Studies

All experiments involving the mice were carried out in accordance with an animal use protocol approved by the University of North Carolina Animal Care and Use Committee. Female BALB/c mice (18-25 g, Jackson Laboratory) were dosed via tail vein injections of 12.5 mg of NPs per kg of mouse weight. The volume of injection ranged from 75 µL to 104 µL of (3 mg/mL) nanoparticle suspension in an isotonic sucrose solution (9.25 wt%).

Intravital microscopy (IVM) was used to assess the circulation profile of the three different particle types. Experiments were performed using an IV 100 laser scanning microscope (Olympus). The mouse was anesthetized with isoflurane and a tail vein catheter was applied. Hair was removed from the ear of the mouse with Nair, and the mouse was placed on a 37 °C heated stage in the prone position and kept under anesthesia. The hairless ear was immobilized to an aluminum block with double-sided tape, and vasculature was visualized with a 488-nm laser. Mice were then dosed with Dylight 650-labeled NPs with varying PEG surface coverage. Fluorescence was measured using a 633-nm laser, and imaging scans were captured every 5 s for 2 hrs. For circulation analysis, the image files from each scan were exported to ImageJ. Following literature procedures, the images were stacked in groups of four, and fluorescent signal in each stack was analyzed in the region of interest.<sup>61, 62</sup> Background corrections were obtained using the initial fluorescence in the region of interest before injection.

In an effort to determine circulation half-life, blood draw and biodistribution studies were also completed. Injections and tissue/blood collection were performed with assistance of the Animal Studies Core (UNC-CH). Mice were dosed with NPs or sucrose (control). For each particle type and control, we examined four mice per time point (5 min, 15 min, 30 min, 1 h, 3 h, and 24 h). At the various time points post-injection, mice were given a dose of ketamine/dexmedetomidine blend to deeply anesthetize them prior to cardiac puncture for blood collection. Blood was collected and stored in heparinized Eppendorf tubes (Milan, USA). Mice were sacrificed and organs (liver, spleen, kidney, and lung) were harvested, weighed, and transferred to 6- or 12-well plates for fluorescence analysis with an IVIS Lumina imager (Caliper Life Sciences); excitation and emission filters were set to 675 nm and 720 nm, respectively. Heparinized blood was pipetted in 100  $\mu$ L aliquots into black 96-well plates and imaged on the IVIS Lumina. In order to determine particle concentration in the blood, we performed serial dilutions (in triplicate) of particles in freshly harvested mouse blood and plotted a standard curve. Pharmacokinetic analysis of the blood draw data was performed using PKSolver.<sup>63</sup> Data was fit to either a one- or two-compartment model and the Akaike information criterion (AIC) was used to compare goodness of fit for each nanoparticle type.<sup>64</sup>

## 2.5 References

1. Owens, D. E.; Peppas, N. A. *Int. J. Pharm.* **2006**, *307* (1), 93-102.
2. Alexis, F.; Pridgen, E.; Molnar, L. K.; Farokhzad, O. C. *Mol. Pharmaceutics* **2008**, *5* (4), 505-515.
3. Muggia, F. M. *J. Clin. Oncol.* **1998**, *16* (2), 811-811.
4. Gradishar, W. J. *Expert. Opin. Pharmacother.* **2006**, *7* (8), 1041-1053.
5. Nel, A. E.; Madler, L.; Velegol, D.; Xia, T.; Hoek, E. M. V.; Somasundaran, P.; Klaessig, F.; Castranova, V.; Thompson, M. *Nat. Matter.* **2009**, *8* (7), 543-557.
6. Li, S. D.; Huang, L. *Biochim. Biophys. Acta* **2009**, *1788* (10), 2259-2266.
7. Jokerst, J. V.; Lobovkina, T.; Zare, R. N.; Gambhir, S. S. *Nanomedicine* **2011**, *6* (4), 715-728.
8. McNeil, S. E. *WIREs Nanomed. Nanobiotechnol.* **2009**, *1* (3), 264-271.
9. Debbage, P. *Curr. Pharm. Des.* **2009**, *15* (2), 153-172.
10. Dobrovolskaia, M. A.; Aggarwal, P.; Hall, J. B.; McNeil, S. E. *Mol. Pharmaceutics* **2008**, *5* (4), 487-495.
11. Li, S. D.; Huang, L. *Mol. Pharmaceutics* **2008**, *5* (4), 496-504.
12. Knop, K.; Hoogenboom, R.; Fischer, D.; Schubert, U. S. *Angew. Chem., Int. Ed.* **2010**, *49* (36), 6288-6308.
13. Mosqueira, V. C. F.; Legrand, P.; Morgat, J. L.; Vert, M.; Mysiakine, E.; Gref, R.; Devissaguet, J. P.; Barratt, G. *Pharm. Res.* **2001**, *18* (10), 1411-1419.
14. Gref, R.; Luck, M.; Quellec, P.; Marchand, M.; Dellacherie, E.; Harnisch, S.; Blunk, T.; Muller, R. H. *Colloids Surf., B* **2000**, *18* (3-4), 301-313.
15. Moghimi, S. M.; Szebeni, J. *Prog. Lipid Res.* **2003**, *42* (6), 463-478.
16. Malmsten, M.; Emoto, K.; Van Alstine, J. M. *J. Colloid Interface Sci.* **1998**, *202* (2), 507-517.
17. Benhabbour, S. R.; Sheardown, H.; Adronov, A. *Macromolecules* **2008**, *41* (13), 4817-4823.

18. Fang, C.; Shi, B.; Pei, Y. Y.; Hong, M. H.; Wu, J.; Chen, H. Z. *Eur. J. Pharm. Sci.* **2006**, 27 (1), 27-36.
19. Bazile, D.; Prudhomme, C.; Bassoullet, M. T.; Marlard, M.; Spenlehauer, G.; Veillard, M. *J. Pharm. Sci.* **1995**, 84 (4), 493-498.
20. Stolnik, S.; Illum, L.; Davis, S. S. *Adv. Drug Del. Rev.* **1995**, 16 (2-3), 195-214.
21. Zahr, A. S.; Davis, C. A.; Pishko, M. V. *Langmuir* **2006**, 22 (19), 8178-8185.
22. Garcia-Fuentes, M.; Torres, D.; Martin-Pastor, M.; Alonso, M. J. *Langmuir* **2004**, 20 (20), 8839-8845.
23. Duncanson, W. J.; Figa, M. A.; Hallock, K.; Zalipsky, S.; Hamilton, J. A.; Wong, J. Y. *Biomaterials* **2007**, 28 (33), 4991-4999.
24. Cheng, T.-L.; Chuang, K.-H.; Chen, B.-M.; Roffler, S. R. *Bioconjugate Chem.* **2012**, 23 (5), 881-899.
25. Bhattacharya, R.; Patra, C. R.; Earl, A.; Wang, S.; Katarya, A.; Lu, L.; Kizhakkedathu, J. N.; Yaszemski, M. J.; Greipp, P. R.; Mukhopadhyay, D.; Mukherjee, P. *Nanomed-Nanotechnol.* **2007**, 3 (3), 224-238.
26. Xia, X. H.; Yang, M. X.; Wang, Y. C.; Zheng, Y. Q.; Li, Q. G.; Chen, J. Y.; Xia, Y. N. *ACS Nano* **2012**, 6 (1), 512-522.
27. Degennes, P. G. *Adv. Colloid Interface Sci.* **1987**, 27 (3-4), 189-209.
28. Kenworthy, A. K.; Hristova, K.; Needham, D.; McIntosh, T. J. *Biophys. J.* **1995**, 68 (5), 1921-1936.
29. Degennes, P. G. *Macromolecules* **1980**, 13 (5), 1069-1075.
30. Storm, G.; Belliot, S. O.; Daemen, T.; Lasic, D. D. *Adv. Drug Del. Rev.* **1995**, 17 (1), 31-48.
31. Damodaran, V. B.; Fee, C. J.; Ruckh, T.; Popat, K. C. *Langmuir* **2010**, 26 (10), 7299-7306.
32. Rex, S.; Zuckermann, M. J.; Lafleur, M.; Silviu, J. R. *Biophys. J.* **1998**, 75 (6), 2900-2914.
33. Hristova, K.; Needham, D. *Macromolecules* **1995**, 28 (4), 991-1002.
34. Soong, R.; Macdonald, P. M. *Biochim. Biophys. Acta* **2007**, 1768 (7), 1805-1814.



35. Lundqvist, M.; Stigler, J.; Elia, G.; Lynch, I.; Cedervall, T.; Dawson, K. A. *PNAS* **2008**, 105 (38), 14265-14270.
36. Ehrenberg, M. S.; Friedman, A. E.; Finkelstein, J. N.; Oberdorster, G.; McGrath, J. L. *Biomaterials* **2009**, 30 (4), 603-610.
37. Faure, A. C.; Dufort, S.; Josserand, V.; Perriat, P.; Coll, J. L.; Roux, S.; Tillement, O. *Small* **2009**, 5 (22), 2565-2575.
38. Moghimi, S. M.; Hunter, A. C.; Murray, J. C. *Pharmacol. Rev.* **2001**, 53 (2), 283-318.
39. Sheng, Y.; Yuan, Y.; Liu, C. S.; Tao, X. Y.; Shan, X. Q.; Xu, F. *J. Mater. Sci.: Mater. Med.* **2009**, 20 (9), 1881-1891.
40. Aggarwal, P.; Hall, J. B.; McLeland, C. B.; Dobrovolskaia, M. A.; McNeil, S. E. *Adv. Drug Del. Rev.* **2009**, 61 (6), 428-437.
41. Dos Santos, N.; Allen, C.; Doppen, A. M.; Anantha, M.; Cox, K. A. K.; Gallagher, R. C.; Karlsson, G.; Edwards, K.; Kenner, G.; Samuels, L.; Webb, M. S.; Bally, M. B. *Biochim. Biophys. Acta* **2007**, 1768 (6), 1367-1377.
42. Damodaran, V. B.; Fee, C. J.; Popat, K. C. *Appl. Surf. Sci.* **2010**, 256 (16), 4894-4901.
43. Du, H.; Chandaroy, P.; Hui, S. W. *Biochim. Biophys. Acta* **1997**, 1326 (2), 236-248.
44. Gessner, A.; Paulke, B. R.; Muller, R. H.; Goppert, T. M. *Pharmazie* **2006**, 61 (4), 293-297.
45. Howard, M. D.; Jay, M.; Dziublal, T. D.; Lu, X. L. *J. Biomed. Nanotechnol.* **2008**, 4 (2), 133-148.
46. Walkey, C. D.; Olsen, J. B.; Guo, H. B.; Emili, A.; Chan, W. C. W. *J. Am. Chem. Soc.* **2012**, 134 (4), 2139-2147.
47. Lindman, S.; Lynch, I.; Thulin, E.; Nilsson, H.; Dawson, K. A.; Linse, S. *Nano Lett.* **2007**, 7 (4), 914-920.
48. De, M.; You, C.-C.; Srivastava, S.; Rotello, V. M. *J. Am. Chem. Soc.* **2007**, 129 (35), 10747-10753.
49. Baier, G.; Costa, C.; Zeller, A.; Baumann, D.; Sayer, C.; Araujo, P. H. H.; Mailander, V.; Musyanovych, A.; Landfester, K. *Macromol. Biosci.* **2011**, 11 (5), 628-638.
50. Cedervall, T.; Lynch, I.; Lindman, S.; Berggard, T.; Thulin, E.; Nilsson, H.; Dawson, K. A.; Linse, S. *PNAS* **2007**, 104 (7), 2050-2055.

51. Pierce, M. M.; Raman, C. S.; Nall, B. T. *Methods* **1999**, *19* (2), 213-221.
52. Jelesarov, I.; Bosshard, H. R. *J. Mol. Recognit.* **1999**, *12* (1), 3-18.
53. Anderson, N. L.; Anderson, N. G. *Mol. Cell. Proteomics* **2002**, *1* (11), 845-867.
54. Casals, E.; Pfaller, T.; Duschl, A.; Oostingh, G. J.; Puentes, V. *ACS Nano* **2010**, *4* (7), 3623-3632.
55. Meng, F. H.; Engbers, G. H. M.; Feijen, J. J. *Biomed. Mater. Res., Part A* **2004**, *70* (1), 49-58.
56. Gref, R.; Minamitake, Y.; Peracchia, M. T.; Trubetskoy, V.; Torchilin, V.; Langer, R. *Science* **1994**, *263* (5153), 1600-1603.
57. Peracchia, M. T.; Fattal, E.; Desmaele, D.; Besnard, M.; Noel, J. P.; Gomis, J. M.; Appel, M.; d'Angelo, J.; Couvreur, P. *J. Controlled Release* **1999**, *60* (1), 121-128.
58. Lankveld, D. P. K.; Rayavarapu, R. G.; Krystek, P.; Oomen, A. G.; Verharen, H. W.; van Leeuwen, T. G.; De Jong, W. H.; Manohar, S. *Nanomedicine* **2011**, *6* (2), 339-349.
59. Sloat, B. R.; Sandoval, M. A.; Li, D.; Chung, W. G.; Lansakara, D. S. P.; Proteau, P. J.; Kiguchi, K.; DiGiovanni, J.; Cui, Z. R. *Int. J. Pharm.* **2011**, *409* (1-2), 278-288.
60. Guzman, J.; Iglesias, M. T.; Compan, V.; Andrio, A. *Polymer* **1997**, *38* (20), 5227-5232.
61. Merkel, T. J.; Jones, S. W.; Herlihy, K. P.; Kersey, F. R.; Shields, A. R.; Napier, M.; Luft, J. C.; Wu, H. L.; Zamboni, W. C.; Wang, A. Z.; Bear, J. E.; DeSimone, J. M. *PNAS* **2011**, *108* (2), 586-591.
62. Tong, L.; He, W.; Zhang, Y. S.; Zheng, W.; Cheng, J. X. *Langmuir* **2009**, *25* (21), 12454-12459.
63. Zhang, Y.; Huo, M. R.; Zhou, J. P.; Xie, S. F. *Comput. Meth. Prog. Bio.* **2010**, *99* (3), 306-314.
64. Akaike, H. *Ieee Transactions on Automatic Control* **1974**, *AC19* (6), 716-723.

## CHAPTER 3 TARGETED PRINT HYDROGELS: THE ROLE OF NANOPARTICLE SIZE AND LIGAND DENSITY ON CELL ASSOCIATION, BIODISTRIBUTION, AND TUMOR ACCUMULATION

### 3.1 Introduction

Passive targeting continues to be the crux of nanoparticle-mediated drug delivery to tumor vascular. Improved efficacy typically associated with particulate systems is dependent on an improved pharmacokinetic profile compared to the native therapeutic as well as preferential accumulation of the carrier within the discontinuous and irregular tumor tissue.<sup>1,3</sup> This superior accumulation is known as the enhanced permeation and retention (EPR) effect, as coined by Maeda and Matsumura in the late 1980's.<sup>2</sup> By reducing the carrier size to sub-100 nm dimensions and by enhancing plasma retention, neoplastic delivery can be augmented drastically due to improved interstitial diffusivity and probability of accretion, respectively.<sup>3</sup> In order to extend circulation time, the carrier must exhibit a neutral or slightly negative surface potential to avoid non-specific cell association and surface chemistry adept at evading the mononuclear phagocytic system (MPS).<sup>4-9</sup> Shape is yet another parameter that should be controlled. While NPs are typically spherical, recent literature has demonstrated that rod-shaped carriers have enhanced cellular internalization both *in vitro* and *in vivo*, as well, greater extravasation into and accumulation within diseased tissue.<sup>10-12</sup> Beyond passive targeting, actively targeted nanoparticulate systems can further enhance therapeutic effect by preferentially targeting over-expressed cellular receptors on cancerous tissue.<sup>13-16</sup>

A distinct advantage offered with particulate-based active targeting is establishing multivalent interactions between the carrier and target cell.<sup>17</sup> Multivalency can lead to enhanced

avidity to target cells with traditional low-affinity ligands; therefore, the ligand library is greatly expanded when coupled with a particle carrier.<sup>18,25</sup> In addition, multivalent interactions can enhance cell binding several orders of magnitude over the unbound ligand yielding dramatically improved payload delivery and tumor reduction.<sup>19</sup> Particle shape and size also have been shown to vary the multivalency effect, with high aspect ratio particulates undergoing cellular endocytosis more rapidly than their spherical counterparts.<sup>20</sup> With these benefits, multivalency also comes with a cost of complexity and can lead to significant changes *in vitro* and *in vivo* from the untargeted counterpart. Determining the optimal density of targeting ligand to epitomize multivalent effects remains an arduous task. The impact of finely controlling ligand surface density cannot be understated, with noted alterations in toxicity, binding coefficient to the target receptor, and tumor accumulation.<sup>15,18, 21-23</sup> While actively targeting these complex particulate systems has become a well-pursued area, off-targeting affects associated with ligand density have yet to be fully understood. Depending on the nanoparticle fabrication technique utilized, controlling all of the outlined parameters (surface chemistry, shape, size, etc.) simultaneously is a challenging if not altogether unobtainable objective.

To this aim, we investigated the effects nanoparticle size, shape, and targeting ligand density *in vitro* and *in vivo*. Passive accumulation in tumor tissue was assessed with sphere-like and rod-shaped hydrogel PRINT particles to determine the role of NP size and shape. Using a FITC-labelled Z<sup>EGFR</sup> affibody, we delicately controlled ligand density functionalized to both particles. Particle shape and size effects on receptor-mediated endocytosis and non-specific uptake were observed as ligand density was held constant between both NPs. Biodistribution and pharmacokinetics were observed as a function of nanoparticle shape, size, and ligand density.

Overall, passive targeting was the dominant factor influencing tumor accumulation while changes in ligand density dramatically shifted *in vitro* and *in vivo* particle behavior.

## 3.2 Results and Discussion

### 3.2.1 Passive Targeting: NP Fabrication, Surface Modification, and Characterization

Calibration-quality hydrogel nanoparticles were synthesized at two sizes: 55 x 60 nm and 80 x 320 nm (Figure 3.1 and Table 3.1). Using a continuous roll-to-roll fabrication system, PRINT particles were rapidly fabricated at 72 and 360 mg/hour for 55 x 60 nm and 80 x 320 nm, respectively. The particle composition consisted of UV-cured acrylate based monomers. A fluorescent marker was included for *in vitro* (Dylight 488) and *in vivo* (Dylight 650/680) studies in addition to the other acrylate polymeric components. The particle matrix was mainly comprised of an HP<sub>4</sub>A monomer coupled with PEG<sub>700</sub>DA cross-linker, yielding a PEG-based nanoparticle that aids in immune system evasion when administered *in vivo*.<sup>5,8,28</sup> An amino functional monomer was incorporated to allow for facile post-functionalization chemistry. For these studies the primary amine was reacted through NHS (N-Hydroxysuccinimide) chemistry to either a monofunctional or bifunctional PEG, for either passive or active tumor accumulation studies. The mass of either mono- or bifunctional terminated PEG charged to the hydrogel particles resulted in a surface density of PEG sufficient to inhibit macrophage uptake and protein opsonization while extending circulation times *in vivo*. Residual amine groups post-PEGylation were converted to inert acetyl groups resulting in a negative NP surface charge, further decreasing undesired cellular uptake when administered IV.<sup>28</sup> As discussed in previous accounts, fabrication by PRINT continued to yield calibration-quality nanoparticles that exhibited narrow polydispersity post-functionalization.<sup>10,21,27,28,34-36</sup>

Table 3.1 Nanoparticle characterization via dynamic light scattering

Type (nm)	Surface Modification	$D_h$ (nm)	PdI	$\zeta$ (mV)
55 x 70	-	$126.8 \pm 4.0$	$0.130 \pm 0.01$	$+38.0 \pm 1.1$
	mPEG/acetylation	$126.7 \pm 2.4$	$0.095 \pm 0.01$	$-16.7 \pm 1.1$
80 x 320	-	$276.6 \pm 2.4$	$0.034 \pm 0.01$	$+35.1 \pm 0.9$
	mPEG/acetylation	$257.3 \pm 2.1$	$0.008 \pm 0.01$	$-19.0 \pm 1.1$

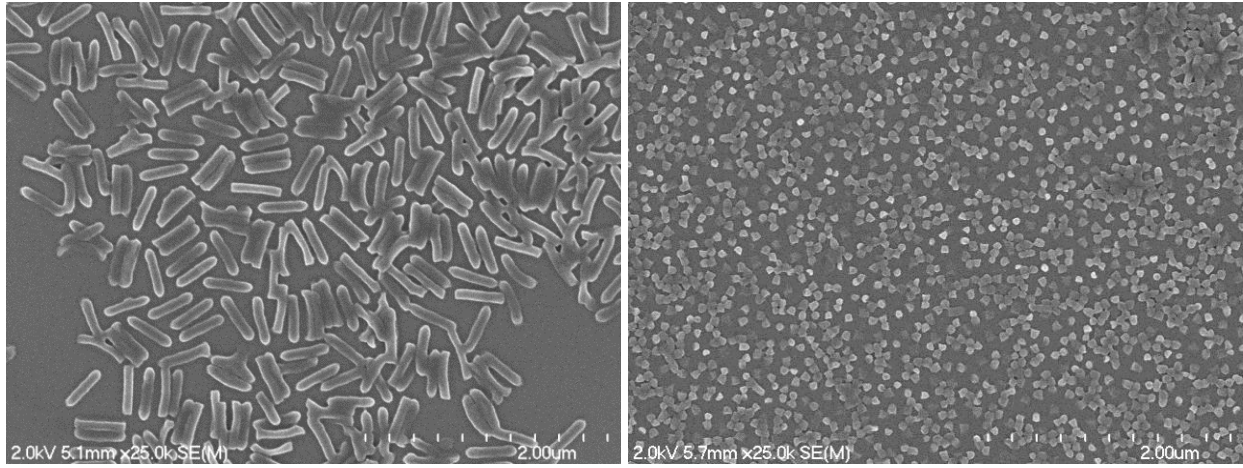


Figure 3.1 Scanning electron micrograph of 80 x 320 nm (left) and 55 x 60 nm (right) hydrogel PRINT nanoparticles.

### 3.2.2 Assessment of Passive Accumulation as Function of Particle Size

Nanoparticle size is arguably the most significant factor dictating success of a nano-based cancer therapy as passive tumor accumulation is largely regulated on size of the carrier.<sup>30</sup> To this end, sub-100 nm particles have recurrently shown greater accumulation and efficacy than larger analogs, as well, general trends indicate tumor uptake is directly correlated to reductions in NP size.<sup>31-33</sup> Yet, previous work from the DeSimone lab has displayed remarkable efficacy in tumor-bearing mouse models with 80 x 320 nm PLGA NPs.<sup>34-36</sup> Taking these findings into account, we conducted biodistribution studies with non-targeted 55 x 60 nm and 80 x 320 nm hydrogel particles in tumor-bearing mice (Figure 3.2). In these studies, the liver exhibited 2-fold greater accumulation with 55 x 60 nm particle ( $42 \pm 5\%$ ) compared to the 80 x 320 nm particle ( $18 \pm$

7%), however, the inverse was observed in the spleen with over 2-fold increase with the larger rod-shaped particle ( $72 \pm 7\%$ ) over the smaller particle ( $30 \pm 7\%$ ). Blood retention at 24 h was statistically the same between the two NP types while tumor accumulation was dramatically enhanced over five-fold with the smaller particle ( $9.1 \pm 2.5\%$ ) compared to the larger particle ( $1.7 \pm 0.7\%$ ). These findings coincided with literature as size reduction typically results in more dispersed distribution throughout all tissues.<sup>38</sup> The noteworthy improvement in tumor accretion reflects the general trend of enhanced tumor penetration with NP size reduction as previously mentioned. This hypothesis is further confirmed as both particles exhibited similar blood retention at 24 h; therefore, each NP type exhibits equal exposure to the tumor vasculature and equal chance to permeate into the diseased tissue.

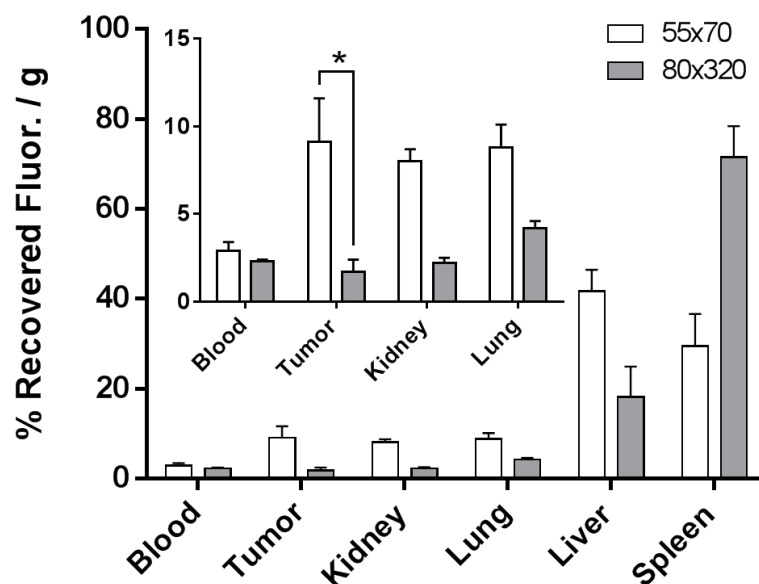


Figure 3.2 Biodistribution of PEGylated 80 x 320 nm and 55 x 60 nm NPs at 24 h in A431 tumor-bearing mice (inset - enhanced view of blood, tumor, kidney, and lung at 24 h).

### 3.2.3 Active Targeting: Conjugation of Ligand at Distinct Surface Densities

Fabricating actively targeted nano-carriers has shown great precedence improving tumor delivery and efficacy.<sup>13-16</sup> Yet, as discussed previously, the optimal ligand density for a particle

platform is reliant on many factors, and changing the targeting density may result in major shifts in biodistribution and PK, possibly rendering an advantageous nanotherapy ineffective.<sup>15,23</sup> In effort to preserve the improved biological profile gained by PEG density optimization, it was of great importance to study ligand density variation on hydrogel NPs.<sup>28</sup> To this end, a highly tunable and precisely controlled ligand quantitation scheme was developed in an effort to delicately vary targeting density on both particle types.

The targeting conjugation scheme utilized an anti-EGFR affibody, selective to the extracellular domain of the EGFR surface glycoprotein, precisely conjugated to the NP surface at several ligand densities (Scheme 3.1). After PEGylating with a thiol-reactive maleimide-PEG<sub>5k</sub>-SCM and subsequent acetylation, FITC-labelled affibody functionalized with a non-structural cysteine group was reacted to the NP surface. Surface modification concluded with addition of mPEG<sub>1k</sub>-thiol to quench residual maleimide groups with an inert methoxy-functionality. Affibody was charged at various amounts to both particle types and the targeting ligand density (LG / nm<sup>2</sup>) was quantified by fluorescence methods similar to those previously described for quantifying PEG density.<sup>28</sup> Due to the fine control exhibited, we were able to maintain similar ligand density between the two particle sizes at three separate densities. For the 80 nm particle, targeting ligand density was calculated to be 0.65, 1.1, 1.8, 3.3, and 4.5 ( x 10<sup>-3</sup>) ligands / nm<sup>2</sup> corresponding to ~ 100, 170, 280, 560, and 700 ligands / NP, respectively. For the 55 nm particle, densities of 1.2, 2.0, and 3.0 ( x 10<sup>-3</sup>) ligands / nm<sup>2</sup> were calculated corresponding to ~ 20, 30, and 40 ligands / NP, respectively (Figure 3.3). For *in vitro* and *in vivo* studies, the FITC-labeled ligand was replaced with an unlabeled analog to reduce possibility of immune recognition. Upon dynamic light scattering and zeta-potential analyses, size and PDI were observed to increase slightly as a function of targeting ligand density while surface charge



neutralized. However, with the 55 nm particle, no distinct trend was observed for size, PDI, or surface charge (Table 3.2).

Scheme 3.1 Conjugation of PRINT NPs to Targeting Ligand

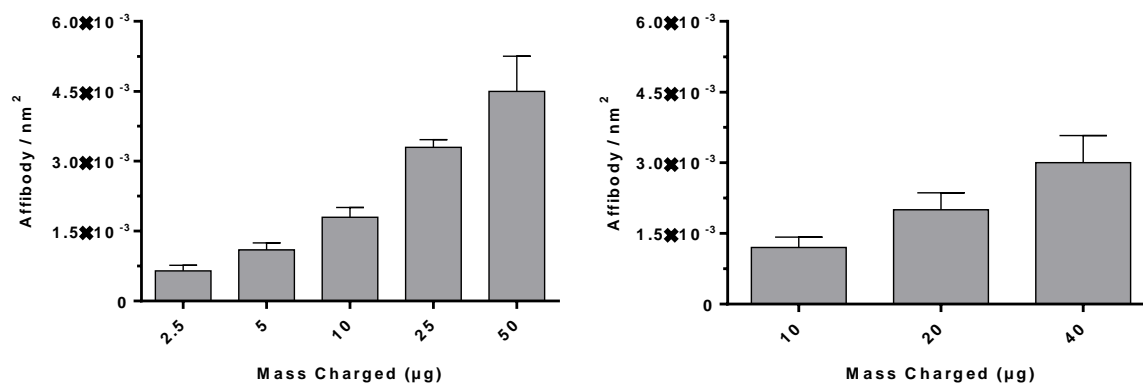
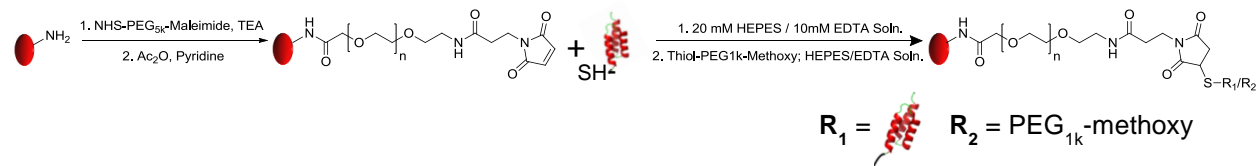


Figure 3.3 Quantification of targeting ligand on 80 x 320 nm (left) and 55 x 60 nm (right) NPs based upon various amounts of fluorescein-labeled Z<sup>EGFR</sup> affibody charged.

Table 3.2 Targeted nanoparticle characterization by dynamic light scattering

Type (nm)	Surface Modification	$D_h$ (nm) <sup>a</sup>	$PdI^a$	$\zeta$ (mV) <sup>a</sup>	Ligand Density (LG/nm <sup>2</sup> ) <sup>b</sup>
<b>80 x 320</b>	Mal-PEG <sub>5k</sub> /Acetylation	270.1 ± 1.4	0.063 ± 0.022	-24.6 ± 0.4	-
	Methoxy-PEG <sub>1k</sub>	271.2 ± 0.7	0.017 ± 0.019	-27.4 ± 0.1	-
	2.5 µg LG Charge	270.1 ± 1.7	0.020 ± 0.017	-25.7 ± 0.9	6.5 x10 <sup>-4</sup> ± 1.2 x10 <sup>-4</sup>
	5 µg LG Charge	276.1 ± 2.5	0.017 ± 0.012	-25.5 ± 0.6	1.1 x10 <sup>-3</sup> ± 1.5 x10 <sup>-4</sup>
	10 µg LG Charge	277.6 ± 2.3	0.015 ± 0.014	-22.0 ± 0.3	1.8 x10 <sup>-3</sup> ± 2.1 x10 <sup>-4</sup>
	25 µg LG Charge	290.2 ± 3.7	0.049 ± 0.042	-17.7 ± 0.7	3.3 x10 <sup>-3</sup> ± 1.6 x10 <sup>-4</sup>
	50 µg LG Charge	295.5 ± 3.8	0.109 ± 0.032	-13.0 ± 1.1	4.5 x10 <sup>-3</sup> ± 7.5 x10 <sup>-4</sup>
<b>55 x 60</b>	Mal-PEG <sub>5k</sub> /Acetylation	172.7 ± 2.5	0.13 ± 0.019	-17.2 ± 0.3	-
	Methoxy-PEG <sub>1k</sub>	174.0 ± 1.1	0.15 ± 0.019	-13.6 ± 0.5	-
	10 µg LG Charge	163.2 ± 4.8	0.11 ± 0.017	-14.3 ± 0.2	1.2 x10 <sup>-3</sup> ± 2.2 x10 <sup>-4</sup>
	25 µg LG Charge	170.5 ± 0.8	0.16 ± 0.012	-13.9 ± 0.6	2.0 x10 <sup>-3</sup> ± 3.6 x10 <sup>-4</sup>
	40 µg LG Charge	165.9 ± 1.6	0.082 ± 0.017	-15.2 ± 0.9	3.0 x10 <sup>-3</sup> ± 5.8 x10 <sup>-4</sup>

<sup>a</sup> Measured by dynamic light scattering<sup>b</sup> Calculated from fluorescence analysis

### 3.2.4 *In vitro* Analysis as Function of Particle Size, Shape, and Ligand Density

*In vitro* studies were conducted with both 55 x 60 nm and 80 x 320 nm particle types to determine ligand density and NP shape/size effects. In these studies, EGFR-overexpressing epidermoid carcinoma (A431) and alveolar macrophage (MH-S) cells were used to conduct targeted cell association and non-specific uptake experiments, respectively. Trypan Blue (TB) typically used as a live/dead stain, was used instead to determine if nanoparticles were membrane bound or internalized by cells. As observed in Figure 3.4, if nanoparticles are

membrane bound, the Dylight 488 (from the nanoparticle) forms a FRET pair with the TB, shifting the  $\lambda_{em}$  of the particle into the PE-Cy5 channel ( $\lambda_{em} \sim 580$  nm). However, since TB cannot penetrate through the plasma membrane, upon NP internalization, a FRET pair is not formed and the  $\lambda_{em}$  remains in the FITC channel ( $\lambda_{em} \sim 520$  nm). In all, four scenarios exist between the cell and the dye-labelled particle upon cell sorting and bivariate analysis: non-association (quadrant 1), membrane bound only (quadrant 2), membrane bound and internalized (quadrant 3), and internalized only (quadrant 4).

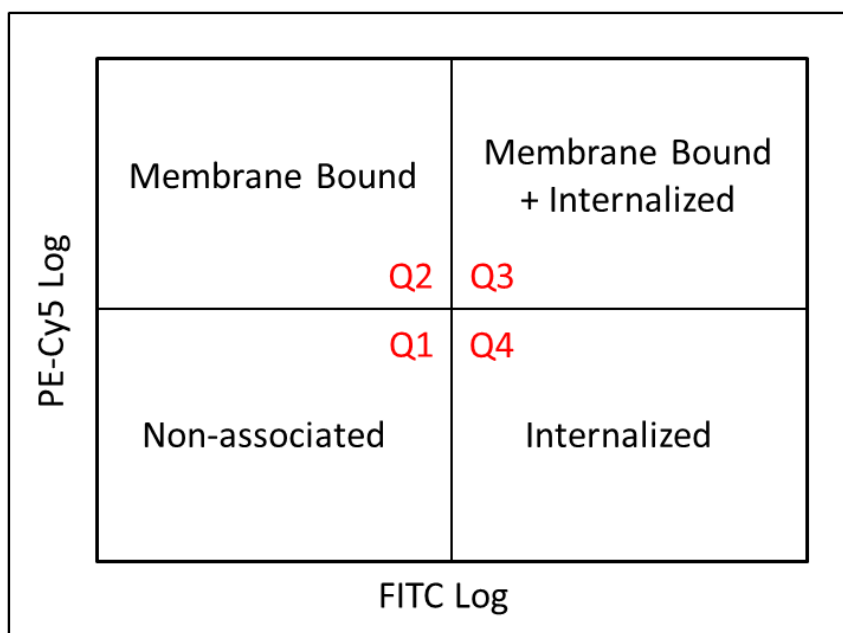


Figure 3.4 Quadrants upon bivariate analysis of flow cytometry of cell-association with targeted nanoparticles.

For targeting experimentation, a direct correlation was observed between ligand density and cells with nanoparticles bound to the outer membrane and internalized in both NP types (Figure 3.5). The rod-shaped type amplified the percentage of cell-membrane interaction at higher ligand densities potentially due to enhanced cellular adhesion over the spherical targeted counterparts; this observation was previously hypothesized via ligand-receptor binding dynamic modeling.<sup>39</sup> For the 80 nm particle, an optimum ligand density was observed at approximately

$1.8 \times 10^{-3}$  LG / nm<sup>2</sup> in the cell population that *only* exhibited internalized NPs and with a further increase in ligand density, the majority of cells displayed NPs both internalized and bound to the outer membrane. Upon increasing particle dosage, an enhancement in association was observed in all cell populations and particle types (Figure 3.6) while negative controls, PEG and wild-type affibody, displayed limited uptake with both particle types. These results seem to indicate a limit in receptor-mediated endocytosis at a specific time point, particle dosage, and ligand density. As well, particle multivalency was proven to be a key factor improving cellular internalization and ligand functionalization was shown to be imperative for any significant cell association. Non-specific uptake studies were conducted to further examine the mechanism of particle internalization as a function of targeting density. In general, non-specific uptake with alveolar murine macrophage displayed negligible association with either set of particles, however, a significant boost in association was found at the highest ligand density for 80 nm type (Figure 3.7). Additionally, mean fluorescence intensity increased with respect to ligand density for the rod-shaped NP type, further indicating a correlation exists between ligand density and non-specific macrophage interaction with rod-like nanoparticles (Figure 3.8).

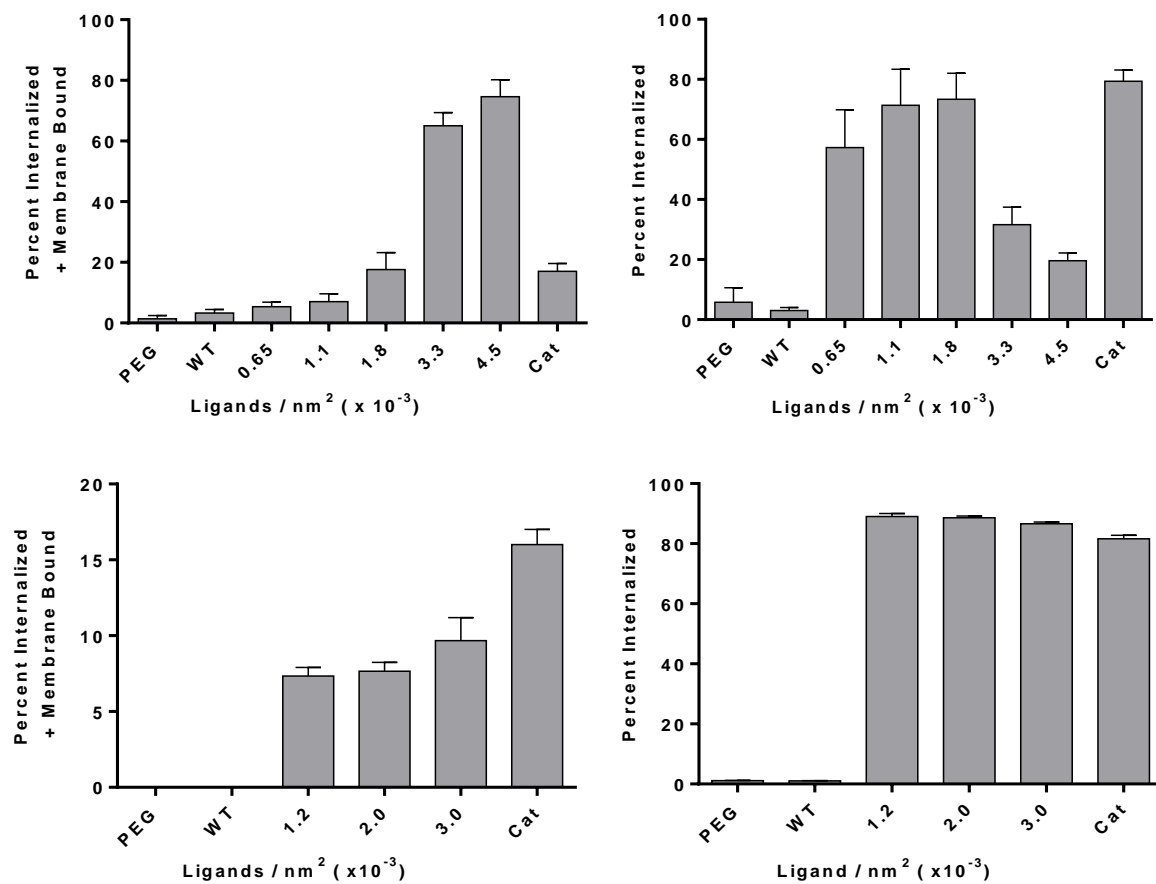


Figure 3.5 In vitro association of A431 cell population upon incubation with targeted 80 x 320 nm (top) and 55 x 60 nm NPs (bottom). Two cell populations are shown, one with NPs both bound to the outer cell membrane and internalized (left) and a second population with NPs only internalized (right).

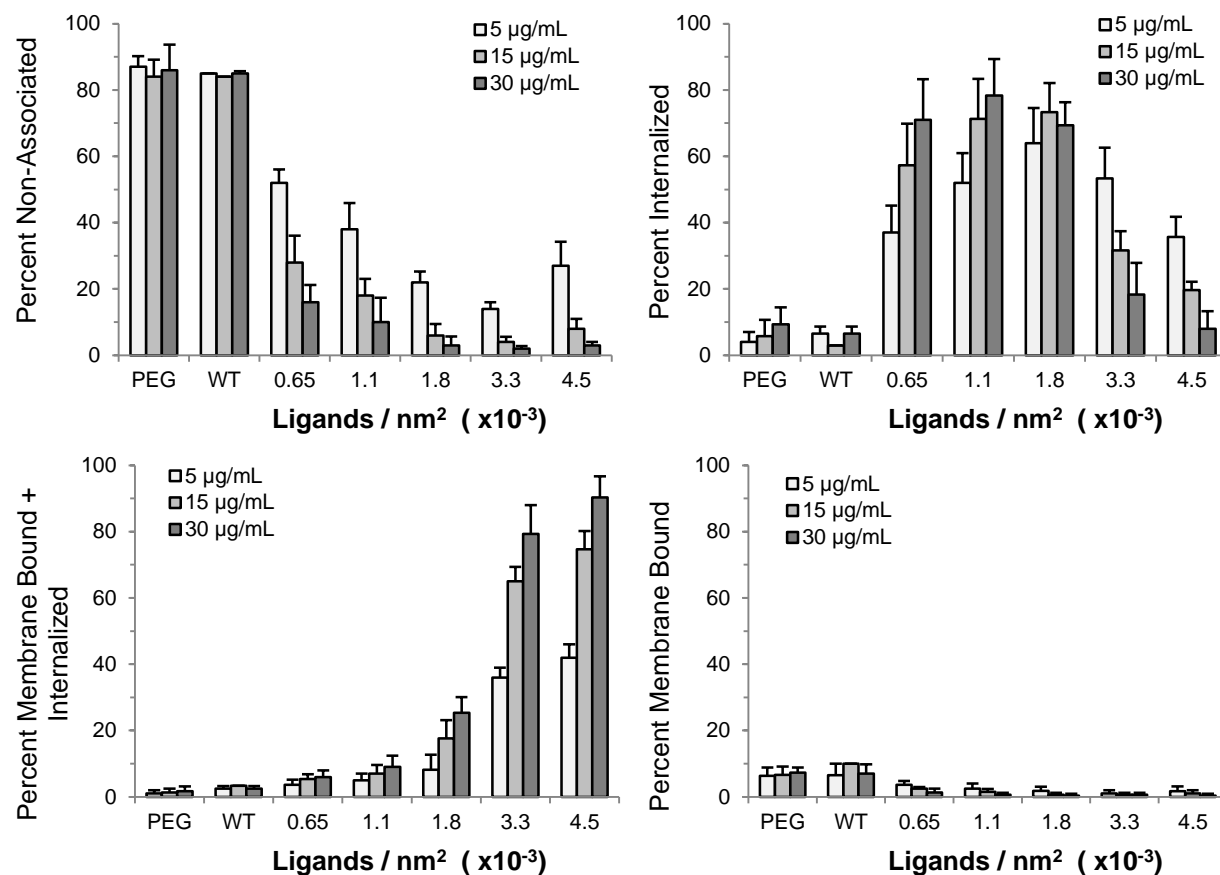


Figure 3.6 Sub-populations A431 cell interactions with 80 x 320 nm particles at five different targeting ligand densities and various dosages.

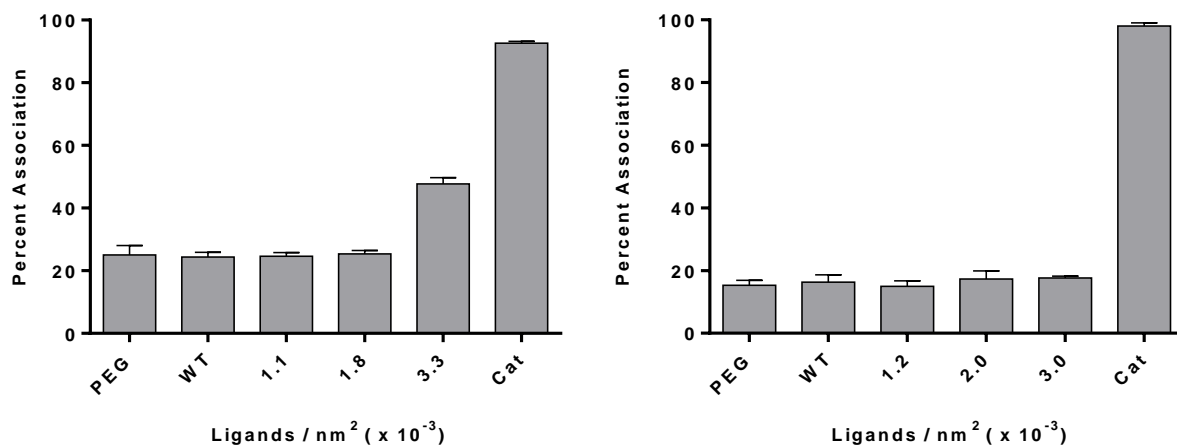


Figure 3.7 Percent association of alveolar macrophage cells (MH-S) with targeted 80 x 320 nm (left) and 55 x 60 nm (right) at three distinct ligand densities.

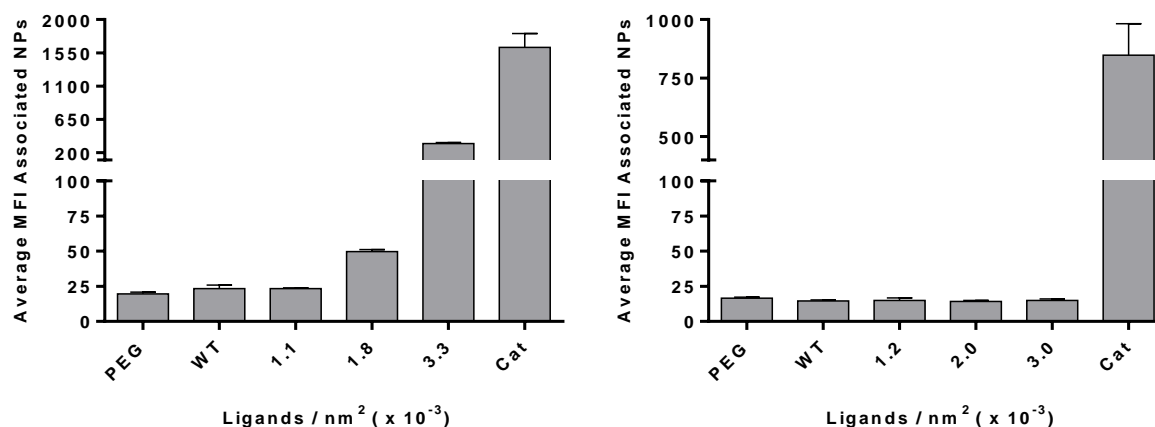


Figure 3.8 Average mean fluorescence intensity of alveolar macrophage cells (MH-S) associated with targeted 80 x 320 nm (left) and 55 x 60 nm (right) at three distinct ligand densities.

To confirm particle association observed was due to EGFR-mediated endocytosis, a competition study was completed. A distinct trend was observed upon which an increase of free affibody concentration in cell culture led to a precipitous reduction in particle association indicating a direct dependence on the receptor-mediated endocytosis pathway for particle internalization (Figure 3.9). In all, these results suggest favorable non-specific uptake with rod-shaped NPs compared to the sphere-like type since ligand density was held roughly constant between both. Similar to previous accounts, an increase in non-specific association trended with ligand density, alluding to enhanced opsonization from de-shielding of PEG coating by proteins in media.<sup>23</sup> The cationic nanoparticles, serving as a positive control, displayed near complete cellular association which is expected due to the strong interaction between the negatively charged cellular membrane and the positive surface charge of amine-functional NPs; this interaction also falls in line with previous literature accounts.<sup>5</sup> The PEG and wild-type, serving as negative controls, showed limited interaction with the EGFR-over expressing cell-line. Based on these *in vitro* findings, it was clear that alterations in ligand density led to significant changes in target (A431) and phagocytic cellular interactions. Murine biodistribution studies were then conducted to elucidate how these *in vitro* results translate to *in vivo* behavior.

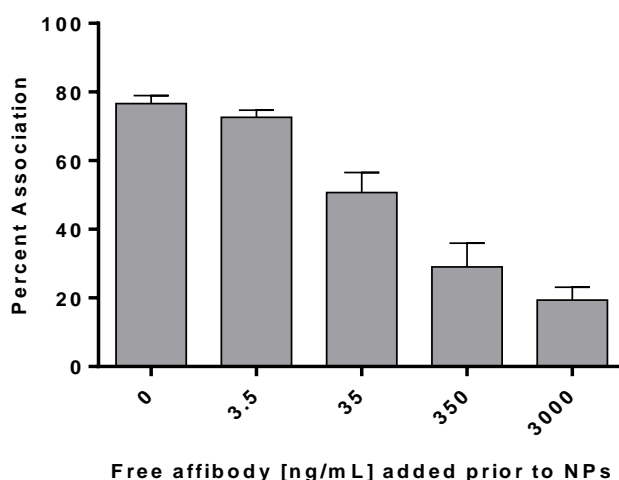


Figure 3.9 A431 cell association of 80 x 320 nm particles (ligand density =  $1.1 \times 10^{-3}$  LG/nm<sup>2</sup>) with pre-dose of free affibody administered at five different concentrations 30 min. prior to particle addition.

### 3.2.5 Assessment of Biodistribution and Pharmacokinetics of Targeted Particles

Biodistribution and blood pharmacokinetics were monitored as a function of targeting ligand density on the 80 x 320 nm hydrogel particle. In general, all targeted NP arms displayed significant reductions in their pharmacokinetic profiles in comparison to the non-targeted PEG control (Figure 3.10 and Table 3.3). The reduction in PK profiles was in direct correlation with targeting ligand density as circulation half-life decreased from 11.2 h with the PEG control to 3.9, 3.3, and 0.7 h with increasing ligand density. The observed area-under-the-curve showed substantial reductions over the PEGylated control, with 5- and 28-fold AUC reductions at the lowest and highest ligand densities, respectively. Clearance rates were drastically increased over the PEG control with 5- and 30-fold increases for the lowest and highest ligand densities, respectively. These findings corroborated with previous accounts in literature that describe enhanced non-specific binding with ligand density increase.<sup>23</sup> Based upon these PK profiles the targeting ligand density was optimized for biodistribution studies in A431-tumor bearing mice (Figure 3.11). Specifically, the targeting density at  $4.5 \times 10^{-3}$  LG/nm<sup>2</sup> was not pursued due to the



precipitous reduction in blood PK. A 24 hour biodistribution study revealed vast differences in particle sequestration as a function of targeting ligand density. A shift from spleen to liver deposition was observed with targeting density enhancement which could be due to innate high expression of EGFR in liver tissue.<sup>40</sup> As observed with blood PK analysis targeting density greatly impacted blood retention, yet, even with the mitigated blood retention, tumor accumulation improved as a function of ligand density indicating possible multivalent effects towards the high-expression EGFR cell-line. From these results it was clear targeting density had a significant impact on *in vivo* outcomes. In order to further enhance tumor accumulation, we underwent a similar biodistribution study with the smaller 55 x 60 nm, as they exhibited superior passive tumor accumulation.

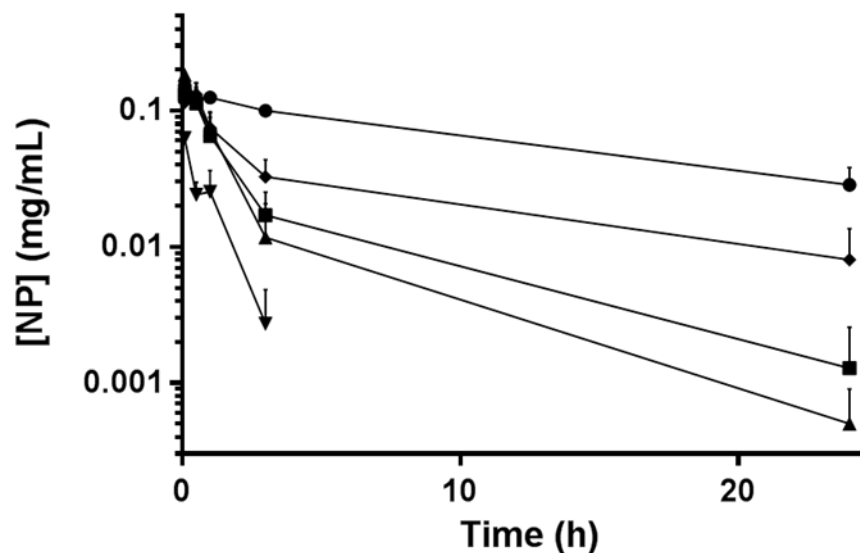
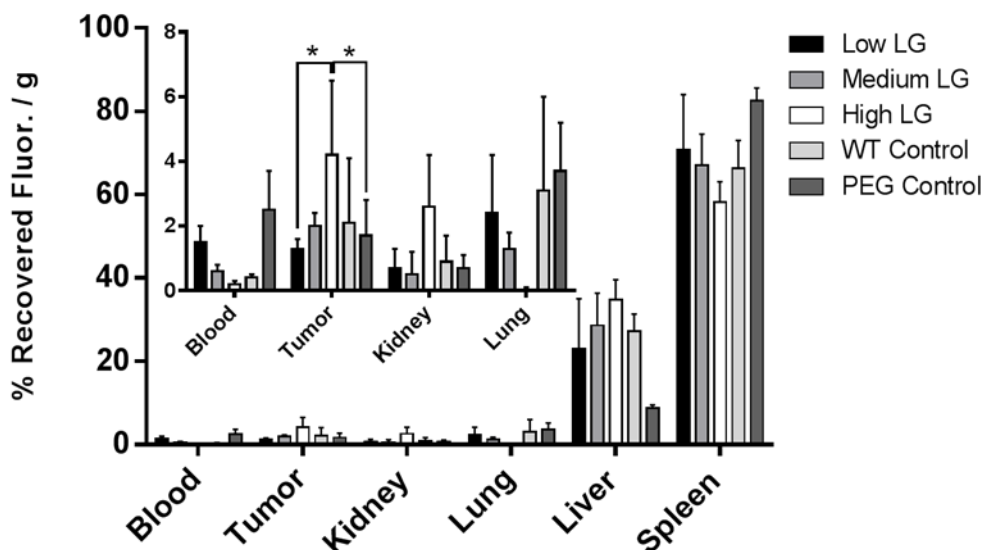


Figure 3.10 Blood pharmacokinetics of 80 x 320 nm NPs at various targeting densities [square =  $6.5 \times 10^{-4}$  LG/nm<sup>2</sup>; triangle =  $1.8 \times 10^{-3}$  LG/nm<sup>2</sup>; inverted triangle =  $4.5 \times 10^{-3}$  LG/nm<sup>2</sup>] at five time points (0.083, 0.5, 1, 3, and 24 h). PEGylated [circle] and wild-type [diamond] used as controls (n = 4).

Table 3.3 Pharmacokinetic parameters of targeted 80 x 320 nm NPs

Ligand Density (LG/nm <sup>2</sup> )	t <sub>1/2</sub> (h)	CL (mL/h)	AUC <sub>0-t</sub> (h*mg/mL)
0.65 x 10 <sup>-3</sup>	3.91	0.81	0.38
1.8 x 10 <sup>-3</sup>	3.32	0.92	0.34
4.5 x 10 <sup>-3</sup>	0.68	4.66	0.06
WT Control	8.19	0.42	0.65
PEG Control	11.17	0.14	1.70

Figure 3.11 Biodistribution of 80 x 320 nm particles at 24 hours. PEGylated and wild-type affibody particles used as controls [Low LG = 6.5 x 10<sup>-4</sup> LG/nm<sup>2</sup>; Med LG = 1.1 x 10<sup>-3</sup> LG/nm<sup>2</sup>; High LG = 1.8 x 10<sup>-3</sup> LG/nm<sup>2</sup>].

Biodistribution of 55 x 60 nm hydrogel was conducted as a function of targeting ligand density in an effort to further enhance tumor accumulation (Figure 3.12). The 55 x 60 nm arms exhibited considerably improved tumor accumulation over any of the 80 x 320 nm particle arms due to the major increase in passive accumulation. Again, all targeted NPs shifted deposition from spleen to liver in comparison to the non-targeted counterparts; however, unlike the larger particle, no discernable difference was observed in liver and spleen as a function of ligand density. In the tumor tissue, the highest targeting ligand density demonstrated the best

accumulation which was statistically similar to the non-targeted PEG control. Even with no statistical difference between the two, the  $Z^{EGFR}$  affibody-conjugated particles have a significantly greater chance of binding and internalizing within diseased cell as previously shown *in vitro*. In order to account for residual blood sequestration in the neo-plastic tissue, tumor:blood (T:B) ratios were calculated and a notable trend was observed. A direct relationship was seen between ligand density and (T:B) ratio, leading to statistically significant improvements in the targeted particle arms over the non-targeted NPs. Similar to the higher aspect ratio particles, increasing targeting ligand density seemed to improve tumor accumulation while simultaneously sacrificing blood retention.

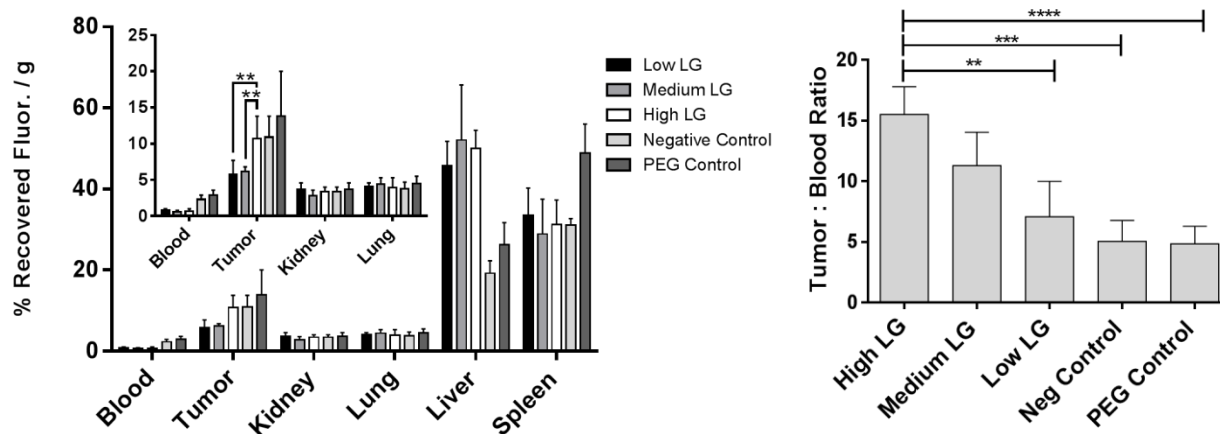


Figure 3.12 Biodistribution (left) and accumulation ratio between tumor and whole blood (right) with 55 x 60 nm NPs at 24 hours. PEGylated and Taq polymerase binder, a bacterial-binding protein, NPs were used as controls [Low LG =  $1.2 \times 10^{-3}$  LG/nm<sup>2</sup>; Med LG =  $2.0 \times 10^{-3}$  LG/nm<sup>2</sup>; High LG =  $3.0 \times 10^{-3}$  LG/nm<sup>2</sup>].

### 3.3 Conclusions

In this account, we have fabricated calibration-quality hydrogel nanoparticles using the PRINT technique at two distinct sizes and shapes. Even though remarkable efficacy has been previously established with the rod-shaped 80 x 320 nm, we found significantly improved passive accumulation with a 55 x 60 nm particle leading to potential improvement in future efficacy studies.<sup>35,36</sup> In effort to retain improvements in macrophage inhibition, protein

resistance, and extended PK profiles previously established with optimized poly (ethylene glycol) surface modulation, we developed a method to finely control the surface ligand density of an EGFR-binding affibody on the two different PRINT particles.<sup>28</sup> With the addition of targeting ligand, *in vitro* analysis yielded rapid association in epidermoid carcinoma cell-line that was entirely dependent on EGFR receptor-mediated endocytosis, however, non-specific uptake was observed in alveolar macrophage with the rod-shaped particle type at high ligand densities. In previous studies, an increase in non-specific macrophage uptake correlated with a stark reduction in circulation persistence which may help explain the drastic inverse correlation observed between ligand density and blood circulation with the 80 x 320 nm particle.<sup>28</sup> However, even with the mitigated blood retention; targeting density had a direct relationship to tumor accumulation at 24 hours. Upon targeting the sphere-like 55 x 60 nm particle, the PEGylated control and highly targeted counterpart exhibited statistically similar tumor accumulation; however, upon accounting for residual blood within the tumor, a distinct trend was observed that displayed a direct correlation between ligand density increase and tumor accumulation. Passive accumulation remains the major factor dictating neoplastic delivery; however, we established that precise control of NP ligand density, size, and shape is paramount when developing an effective delivery vehicle.

### 3.4 Materials and Methods

#### 3.4.1 Materials

2-aminoethyl methacrylate hydrochloride (AEM), diphenyl (2,4,6-trimethylbenzoyl) phosphine oxide (TPO), poly (ethylene glycol) diacrylate (Mn 700) (PEG<sub>700</sub>DA), trypsin, ethylenediaminetetraacetic acid (EDTA), and sucrose were obtained from Sigma-Aldrich. PTFE syringe filters (13 mm membrane, 0.2  $\mu$ m pore size), Thermo Scientific Dylight 488, 650, and

680, Thermo Scientific immobilized (tris(2-carboxyethyl)phosphine)disulfide reducing gel (TCEP), Thermo Scientific HyClone fetal bovine serum (FBS), triethylamine (TEA), acetic anhydride, pyridine, 4-(2-Hydroxyethyl) piperazine-1-ethanesulfonic acid (1M HEPES buffer), methanol, sterile water, dimethylformamide (DMF), Dulbecco's phosphate buffered saline (pH 7.4) (DPBS), 1X phosphate buffered saline (pH 7.4) (PBS), and Dulbecco's Modified Eagle's Medium (DMEM) were purchased from Fisher Scientific. Maleimide-PEG<sub>5k</sub>-succinimidyl carboxy methyl ester (Mal-PEG<sub>5k</sub>-SCM), methoxy-PEG<sub>5k</sub>- succinimidyl carboxy methyl ester (mPEG<sub>5k</sub>-SCM), and methoxy-PEG<sub>1k</sub>-thiol (mPEG<sub>1k</sub>-SH) were all obtained from Creative PEGWorks (Winston Salem, NC). Polyvinyl alcohol (M<sub>w</sub> 2000) (PVOH) was bought from Acros Organics and 2 µm conventional filters were purchased from Agilent Technologies. Borate buffer (pH 9.5) was acquired from RICCA Chemical Company. Murine alveolar macrophage (MH-S) cells and human epidermoid carcinoma (A431) cells were purchased from American Type Culture Collection. PRINT molds (80 nm x 80 x 320 nm and 55 x 60 nm) were acquired from Liquidia Technologies. Tetraethylene glycol monoacrylate (HP<sub>4</sub>A) was synthesized in-house by previously described methods.<sup>24</sup> Monomeric EGFR targeting affibody (Z<sup>EGFR1907</sup>), fluorescein-labelled analog, and the wild-type affibody control were prepared with methods previously described.<sup>26</sup>

### 3.4.2 Nanoparticle Fabrication

The nano fabrication technique, Particle Replication in Non-wetting Templates (PRINT), has previously been described in greater detail.<sup>10,27,28</sup> In this account, our general pre-particle solution (PPS) consisted of a 3.5 wt% of cure-site monomer (CSM) in methanol. For studies quantifying density of affibody a CSM composition of 69 wt% HP<sub>4</sub>A (main monomer), 20 wt% AEM (functional monomer), 10 wt% PEG<sub>700</sub>DA (cross-linker), and 1 wt% TPO (photoinitiator)

was used. For all *in vitro* and *in vivo* studies a CSM composition of 68 wt% HP<sub>4</sub>A, 20 wt% AEM, 10 wt% PEG<sub>700</sub>DA, 1 wt% TPO, and 1 wt% Dylight maleimide (488, 650, or 680; imaging agent) was used. In our studies, two different NP types (55 x 60 nm and 80 nm x 80 x 320 nm) were fabricated. Using a Mayer rod (#3 for 80 x 320 nm; #2 for 55 x 60 nm) and a standard syringe pump (pump rate: 90 mL/h for 80 x 320 nm, 60 mL/h for 55 x 60 nm), a thin film of PPS was drawn onto corona treated PET with the aid of a custom large scale roll-to-roll PRINT nano-fabrication system at 12 ft/min. The methanol was evaporated from the PET delivery sheet using two heat guns resulting in a thin monomer film. The delivery sheet was laminated to the nano-patterned side of mold (either 80 nm x 80 nm x 320 or 55 x 60 nm Teflon-like mold) using a pressurized nip (80 PSI), filling the patterned nano-cavities via capillary action, and then delaminated. The acrylate monomer mixture was cured in the filled mold upon passing through a UV-LED (Phoseon,  $\lambda_{\text{spectral output}}$  395 nm, 3 SCFM N<sub>2</sub>) yielding cured particles in the mold. A PVOH harvesting sheet was laminated to the filled mold, passed through a heated/pressurized nip (80 PSI, 160°C, 3 ft/min), cooled to room temperature, and then the harvesting sheet was split from the empty mold. The nanoparticle array was collected from the harvesting sheet by passing it through a bead of sterile water (4 ft/min; 2 mL water per 10 foot section), in turn, dissolving the PVOH and yielding a particle suspension. The NP suspension was passed through a 2  $\mu$ m Agilent filter to remove residual scum layer or particulates. The suspension was further purified by centrifugation with an Eppendorf 5417R centrifuge at 7,000 RPM for 20-30 min and the pelleted impurities were discarded by decantation from the purified supernatant. Excess PVOH was removed by centrifugation at 14,000 RPM (20-30 minutes for 80 x 320 nm, 1-3 hours for 55 x 60 nm) followed by supernatant removal and resuspension of the NP pellet in sterile water. The removal of excess PVOH was repeated three times.

### 3.4.3 Nanoparticle Characterization

The particle concentration was assessed by thermogravimetric analysis (TGA) on a TA Instruments Q5000 TGA. In short, 10  $\mu\text{L}$  of the nanoparticle suspension was pipette into a tared aluminum sample pan. The sample was heated to 130°C (30°C/min) and held at isotherm for 10 minutes. The sample was then cooled to 30°C (30°C/min) and held for a 2 minute isotherm. The process was repeated with the supernatant from a centrifuged nanoparticle sample in order to account for remaining mass of PVOH in the solution. The particle concentration was determined by subtracting the concentration of remaining stabilizer from the original particle solution yielding the actual NP concentration of the stock solution. The particles were imaged by scanning electron microscopy (SEM) with a Hitachi S-4700 SEM. Before imaging, the particle stock solution was diluted (50  $\mu\text{g/mL}$ ) in methanol and 2  $\mu\text{L}$  was pipette onto a silicon wafer. Using a Cressington 108 auto sputter coater, a 1.5 nm palladium-gold coating was sputtered onto the Si wafer and the sample was analyzed. Particle size and zeta potential was determined by dynamic light scattering (DLS) after dilution (0.1 mg/mL in water) using a Zetasizer Nano ZS (Malvern Instruments, Ltd.).

The hydrated dimensions of the both particle types were measured by fluid atomic force microscopy (AFM) using an Asylum Research MFP-3D atomic force microscope. Height and phase retraces were measured in water, in AC mode using a silicon nitride cantilever (Budget Sensors,  $k = 0.06 \text{ N/m}$ ) at a 1 Hz scan rate and 2  $\mu\text{m}$  scan size. The AFM sample was prepared by placing a droplet of suspended nanoparticles on a glass slide and the solvent was allowed to evaporate from the sample. With the particles settled on the slide, a droplet of water was placed on the sample to rehydrate the NPs and another droplet of water was placed on the cantilever tip. The hydrated AFM tip and glass slide were married and the images were collected. The

dimensions and subsequent surface area of both particle types (both 80 x 320 nm and 55 x 60 nm) were measured by using either the phase or height retrace.

#### 3.4.4 Surface Conjugation of NPs for Non-Targeted Studies

After particle purification, the suspension was washed into DMF (3x) using the centrifugation method (14,000 RPM; 0.5 to 1 h) and concentration was assessed by TGA analysis. The particle solution (1 mg; 0.865 mg/mL) was reacted with TEA (100  $\mu$ L) and shaken for ten minutes on a shaker plate at room temperature (Eppendorf; 1400 rpm). Methoxy-PEG<sub>5k</sub>-SCM was dissolved in DMF (14 mg; 100 mg/mL) added to the reaction mixture and left to react overnight. The reaction mixture was washed in DMF (2x) by centrifugation and resuspended in DMF (1 mg; 1 mg/mL). Post-PEGylation, the unreacted amine groups on the nanoparticle were quenched upon addition of pyridine (10  $\mu$ L) and acetic anhydride (14  $\mu$ L) and the mixture was shaken at room temperature for 30 minutes. The reaction mixture was washed in DMF (1x), pH 9.5 borate buffer (1x), and sterile water (3x). Following surface modification of both nanoparticle types, the particles were analyzed by DLS, TGA, and SEM.

#### 3.4.5 Affibody Quantification

For affibody quantification studies, the same conjugation methods were used for both PEGylation and acetylation procedures as described above. However, in place of the inert methoxy-terminated PEG<sub>5k</sub>-SCM, a maleimide-terminated PEG<sub>5k</sub>-SCM was conjugated in order to functionalize the cysteine-terminated Z<sup>EGFR</sup> affibody to the NP surface. Following surface modification, the functionalized NPs were characterized by TGA and DLS analysis. After characterization, the NP suspension (1 mg) was centrifuged and swapped to a 20 mM HEPES / 10 mM EDTA solution at ~1 mg/mL. Immobilized TCEP disulfide reducing gel (1.5x volume of affibody solution) was washed three times by spinning down the gel beads, removing the



supernatant, and resuspending in HEPES/EDTA solution (1 min; 600 rpm). FITC-labelled Z<sup>EGFR</sup> affibody (0.5 mg/mL) modified with a non-structural terminal cysteine group was added to the pelleted TCEP gel and the slurry was mixed on a shaker plate (1200 rpm) at room temperature for 45 minutes. After disulfide reduction, the slurry was centrifuged (2 min; 600 rpm) and the affibody supernatant was removed from the reducing gel. The activated affibody was immediately added to the modified-nanoparticle solution (1 mg; 1 mL total volume) and shaken overnight (1400 rpm). The mass of affibody charged per mg of NPs varied depending on the nanoparticle type being functionalized (80 nm x 320 v. 55 x 60 nm). When modifying 80 x 320 nm hydrogel particles, affibody was charged at 2.5, 5, 10, 25, or 50 µg per mg modified-NPs; however, with 55 x 60 nm NPs, affibody was charged at 10, 20, or 40 µg per mg NP. Thiol-PEG<sub>1k</sub>-SH was dissolved in the HEPES buffer solution at 100 mg/mL and added (27 µL) to the NP reaction which continued to shake for three hours. The NP reaction was then centrifuged and washed in water (4x). The FITC-tagged affibody NPs were then characterized by DLS, SEM, and TGA.

After conjugating fluorescently-tagged affibody to the nanoparticle surface, the amount of affibody conjugated to the particle was assessed by fluorescent analysis. The FITC tagged affibody-PEG-NP (1 mg/mL) solution was diluted 1:10 in borate buffer and transferred (200 µL) into a Corning black well plate in triplicate. The supernatant from the same nanoparticle solution was added to the black 96-well plate using the same method. A serial dilution of unconjugated FITC-affibody was utilized to create a standard curve (10 µg/mL - 0.01 µg/mL) and fluorescence measurements ( $\lambda_{\text{ex}} = 494 \text{ nm}$ ;  $\lambda_{\text{em}} = 521 \text{ nm}$ ) of the 96-well plate containing the (1) targeted nanoparticle (2) standard curve (3) and supernatant were taken using a SpectraMax M5 plate-reader. The fluorescence in the supernatant was subtracted from the fluorescence observed in the

nanoparticle suspension and the final fluorescence correlated to FITC-tagged affibody concentration via standard curve.

#### 3.4.6 Surface Conjugation of NPs for Targeted Studies

For *in vitro* and *in vivo* studies with targeted nanoparticles, the conjugation methodology outlined above was followed. However, instead of FITC-labelled affibody, a non-tagged analog was used. A wild-type affibody was utilized as a negative control and it was conjugated to the functionalized NPs with identical methods. Additionally, a non-targeted PEG control was used as a second negative control and it was fabricated by following all steps outlined above except for the addition of targeting ligand. A completely non-functionalized positively charged particle was used as a positive control for *in vitro* experimentation.

#### 3.4.7 A431 Cell Association and Competition Assay

For cellular association experiments, A431 cells were plated in complete medium (DMEM) at 20,000 cells per well in a 24-well plate and incubated overnight (37°C, 5% CO<sub>2</sub>) to 50% confluence. Dye-labelled particles were then dosed at three different concentrations (5, 15, 30 µg / mL) onto the A431 cells and incubated for 1 and 4 h. At these time points, cells were washed (3x) with 0.5 mL 1x PBS and the cells were detached from the plate with 1x trypsin/EDTA (300 µL / well). Cells were resuspended in 500 µL of a 0.2% TB solution (1:1 1x PBS with 10% FBS) for a total sample volume of 800 µL. The A431 cells were transferred to a polypropylene tube and analyzed using a flow. For each sample 10,000 cells were measured.

#### 3.4.8 Macrophage Association Study

Murine alveolar macrophage cells (MH-S) were used to determine how nanoparticle association and internalization varies as a function of both targeting ligand density and nanoparticle size. In these studies, MH-S cells were plated (40,000 cells per well) in a 24-well

plate and incubated at 37°C for 48 h. Following the time period, dye-labelled (Dylight 488) nanoparticles (20 µg / mL) were incubated with the macrophage cells for 4 and 24 h. At the time points, cells were washed three times with 0.5 mL 1x PBS and 1x trypsin/EDTA (300 µL / well) was added to detach the cells from the plate. The cell solution was transferred to a polypropylene tube and analyzed using a flow cytometer. For each sample 10,000 cells were measured.

#### 3.4.9 *In Vivo* Studies

All animal studies were carried out with the approved protocol by The University of North Carolina Animal Care and Use Committee. Female athymic nude mice (*Foxn1<sup>nu</sup>*; 20- 30 g) were dosed via tail vein injection from an 8 mg /mL nanoparticle suspension in an isotonic 9.25 wt% sucrose solution.

For all tumor studies, mice aged 4-6 weeks and 20-25 grams in body weight were purchased from UNC-Chapel Hill's animal core. A431 cells were administered ( $2 \times 10^6$  cells in 150 µL of DMEM) subcutaneously into the right rear flank of each mouse and tumor volume was estimated by the formula:  $\text{mm}^3 = (w^2 \times l) / 2$ , where  $w$  = width and  $l$  = length of the tumor. After approximately 4 weeks, tumors were 300-500 mm<sup>3</sup> and mice were randomized for each study arm.

To determine nanoparticle size dependence on passive tumor accumulation, PEGylated/non-targeted hydrogels of two distinct sizes were dosed into tumor-bearing mice. Nanoparticle injections and harvesting of organs were performed with aid from the Animal Studies Core at UNC-Chapel Hill. Mice were dosed (60 mg / kg) with 80 x 320 nm particles, 55 x 60 nm particles, or sucrose (N = 4 per arm). After 24 h, mice were anesthetized with a ketamine/ dexmedetomidine blend. Mice were then euthanized via cardiac puncture for blood collection (stored in heparinized Eppendorf tubes) and cervical dislocation for a secondary

conformation of death. Tissues were harvested (liver, spleen, lung, kidney, and tumor), weighed, and transferred to 12-well plates for fluorescence analysis on an IVIS Lumina instrument (Caliper Life Sciences) and fluorescence filters were set ( $\lambda_{\text{ex}} = 675 \text{ nm}$  /  $\lambda_{\text{em}} = 720 \text{ nm}$ ). Harvested blood (100  $\mu\text{L}$ ) from all samples was transferred into a black 96-well plate and a small aliquot of each particle type was pipette into blood from a control mouse (5  $\mu\text{L}$  NP stock in 195  $\mu\text{L}$  blood) in order to normalize fluorescence between NPs.

In an effort to determine how targeting ligand density affects blood retention over time, 80 x 320 nm particles were administered and harvested at several time points. These studies were conducted with five different nanoparticle arms:  $6.5 \times 10^{-4} \text{ LG/nm}^2$ ,  $1.8 \times 10^{-3} \text{ LG/nm}^2$ ,  $4.5 \times 10^{-3} \text{ LG/nm}^2$ , PEG control, and a wild-type negative control (12.5 mg / kg). Mice were harvested at five different time points: 0.083, 0.5, 1, 3, and 24 h (N = 4 per time point for each NP arm). Tissue harvests and fluorescence analysis were both conducted in the same manner as methods previously described. PK analysis of blood retention studies were conducted with MS Excel PK Solver 2.0.<sup>29</sup> Data was fit to a non-compartmental model for all nanoparticle type.

Targeted tumor accumulation and biodistribution studies with targeted 80 x 320 nm hydrogels in A431 tumor-bearing mice were conducted as a function of targeting ligand density. The general procedure outlined in the non-targeted particle biodistribution section above was followed, except nanoparticle arms were altered. For this study, five different particles types were analyzed:  $6.5 \times 10^{-4} \text{ LG/nm}^2$ ,  $1.1 \times 10^{-3} \text{ LG/nm}^2$ ,  $1.8 \times 10^{-3} \text{ LG/nm}^2$ , PEG control, and a wild-type negative control (12.5 mg / kg). It should be noted that the NP ligand density at  $4.5 \times 10^{-3} \text{ LG/nm}^2$  was not conducted due to poor blood retention observed in the previous pharmacokinetic experiment. Additionally, Dylight 650 was used as the nanoparticle imaging agent instead of Dylight 680.

In order to determine how NP size and targeting density affect tumor accumulation and biodistribution, *in vivo* trials were conducted with 55 x 60 nm particles in tumor-bearing mice. In this experiment five different nanoparticle arms were investigated:  $1.2 \times 10^{-3}$  LG/nm<sup>2</sup>,  $2.0 \times 10^{-3}$  LG/nm<sup>2</sup>,  $3.0 \times 10^{-3}$  LG/nm<sup>2</sup>, PEG control, and negative control. Notably, ligand loadings were designed to closely match that of the 80 x 320 nm tumor accumulation study at the two highest ligand densities. As well, a third ligand density was appended onto the study to potentially enhance nanoparticle uptake in the tumor even further.

### 3.5 References

1. Li, S. D.; Huang, L. *Mol. Pharm.* **2008**, 5 (4), 496–504.
2. Matsumura, Y. and Maeda, H. *Cancer Res.* **1986**, 46, 6387-6392.
3. Bertrand, N.; Wu, Jun.; Xu, X.; Kamaly, N.; and Farokhzad, O. C. *Adv. Drug Deliver. Rev.* **2014**, 66, 2-25.
4. Heidel, J. D.; Davis, M. E. *Pharm. Res.* **2011**, 28, 187–199.
5. Alexis, F.; Pridgen, E.; Molnar, L.K.; Farokhzad, O.C. *Mol. Pharm.* **2008**, 5 (4), 505-515.
6. Xiao, K.; Li, Y.; Luo, J.; Lee, J.S.; Xiao, W.; Gonik, A.M.; Agarwal, R.G.; Lam, S.L. *Biomaterials* **2011**, 32 (13), 3435-3446.
7. Yamamoto, Y.; Nagasaki, Y.; Kato, Y.; Sugiyama, Y.; Kataoka, K. *J. Control. Release* **2001**, 77 (1-2), 27-38.
8. Gref, R.; Luck, M.; Quellec, P.; Marchand, M.; Dellacherie, E.; Harnisch, S.; Blunk, T.; Muller, R. H. *Colloids Surf., B* **2000**, 18 (3–4), 301–313.
9. Sun, X.; Rossin, R.; Turner, J.L.; Becker, M.L.; Joralemon, M.J.; Welch, M.J.; Wooley, K.L. *Biomacromolecules* **2005**, 6, 2541-2554.
10. Gratton, S. E. A.; Napier, M. E.; Ropp; P. A.; Tian, S. and DeSimone J. M. *Pharm. Res.* **2008**, 25 (12), 2845-2852.
11. Huang, X.; Teng, X.; Chen, D.; Tang, F. and He, J. *Biomaterials* **2010**, 31 (3), 438-448.
12. Frieboes, H. B.; Wu, M.; Lowengrub, J.; Decuzzi, P. and Cristini, V. *PLoS ONE* **2013**, 8 (2), 1-11.
13. Byrne, J. D.; Betancourt, T. and Brannon-Peppas, L. *Adv. Drug Deliver. Rev.* **2008**, 60, 1615-1626.
14. Iinuma, H.; Maruyama, K.; Okinaga, K.; Sasaki, K.; Sekine, T.; Ishida, O.; Ogiwara, N.; Johkura, K. and Yonemura, Y. *Int. J. Cancer* **2002**, 99, 130-137.
15. Hrkach, J.; Hoff, D. V.; Ali, M. M.; Andrianova, E.; Auer, J.; Campbell, T.; Witt, D. D.; Figa, M.; Figueiredo, M.; Horhota, A.; Low, S.; McDonnell, K.; Peeke, E.; Retnarajan, B.;

- Sabnis, A.; Schnipper, E.; Song, J. J.; Song, Y. H.; Summa, J.; Tompsett, D.; Troiano, G.; Hoven, T. V. G.; Wright, J.; LoRusso, P.; Kantoff, P. W.; Bander, N. H.; Sweeney, C.; Farokhzad, O. C.; Langer, R. and Zale, S. *Sci. Transl. Med.* **2012**, *4* (128), 128-139.
16. Lopes de Monezes, D. E.; Pilarski, L. M. and Allen, T. M. *Cancer Res.* **1998**, *58*, 3320-3330.
  17. Cheng, Z.; Zaki, A. A.; Hui, J. Z.; Muzykantov, V. R.; Tsourkas, A. *Science* **2012**, *338*, 903-910.
  18. Davis, M. E.; Chen, Z. and Shin, D. M. *Nat. Rev. Drug Discov.* **2008**, *7*, 771-782.
  19. Hong, S.; Leroueil, P. R.; Majoros, I. J.; Orr, B. G.; Baker, J. R. and Holl, M. M. B. *Chem. Biol.* **2007**, *14*, 107-115.
  20. Kolhar, P.; Anselmo, A. C.; Gupta, V.; Pant, K.; Prabhakarapandian, B.; Ruoslahti, E. and Mitagotri, S. *PNAS* **2013**, *110* (26), 10753-10758.
  21. Wang, J.; Tian, S.; Petros, R. A.; Napier, M. E. and DeSimone, J. M. *J. Am. Chem. Soc.* **2010**, *132* (32), 11306-11313.
  22. Elias, D. R.; Poloukhine, A.; Popik, V. and Tsourkas, A. *Nanomed-Nanotechnol.* **2013**, *9* (2), 194-201.
  23. Salvati, A.; Pitek, A. S.; Monopoli, M. P.; Prapainop, K.; Bombelli, F. B.; Hristov, D. R.; Kelly, P. M.; Aberg, C.; Mahon, E. and Dawson, K. A. *Nat. Nanotechnol.* **2013**, *8*, 137-143.
  24. Guzman, J.; Iglesias, M. T.; Compan, V. and Andrio, A. *Polymer* **1997**, *38* (20), 5227-5232.
  25. Montet, X.; Funovics, M.; Montet-Abou, K.; Weissleder, R. and Josephson, L. *J. Med. Chem.* **2006**, *49* (20), 6087-6093.
  26. Kim, D.; Yan, Y.; Valencia, C. A. and Liu, Rihe. *PLoS One* **2012**, *7* (8), 1-13.
  27. Rolland, J. P.; Maynor, B. W.; Euliss, L. E.; Exner, A. E.; Denison, G. M. and DeSimone, J. M. *J. Am. Chem. Soc.* **2005**, *127*, 10096-10100.
  28. Perry, J. L. and Reuter, K. G.; Kai, M. P.; Herlihy, K. P.; Jones, S. W.; Luft, J. L.; Napier, M.; Bear, J. E. and DeSimone, J. M. *Nano Lett.* **2012**, *12* (10), 5304-5310.

29. Zhang, Y.; Huo, M.; Zhou, J. and Xie, S. *Comput. Methods Programs Biomed.* **2010**, *99*, 306-314.
30. Yuan, F.; Dellian, M.; Fukumura, D.; Leunig, M.; Berk, D. A.; Torchilin, V. P. and Jain, R. K. *Cancer Res.* **1995**, *55*, 3752-3756.
31. Perrault, S. D.; Walkey, C.; Jennings, T.; Fischer, H. C. and Chan, W. C. W. *Nano Lett.* **2009**, *9* (5), 1909-1915.
32. Huo, S.; Ma, H.; Huang, K.; Liu, J.; Wei, T.; Jin, S.; Zhang, J.; He, S. and Liang, X. *Cancer Res.* **2012**, *73* (1), 1-12.
33. Schadlich, A.; Caysa, H.; Mueller, T.; Tenambergen, F.; Rose, C.; Gopferich, A.; Kuntsche, J. and Mader, K. *ACS Nano* **2011**, *5* (11), 8710-8720.
34. Chu, K. S.; Hasan, W.; Rawal, S.; Walsh, M. D.; Enlow, E. M.; Luft, J. C.; Bridges, A. S.; Kuijter, J. L.; Napier, M. E.; Zamboni, W. C. and DeSimone, J. M. *Nanomed-Nanotechnol.* **2013**, *9* (5), 686-693.
35. Chu, K. S.; Schorzman, A. N.; Finniss, M. C.; Bowerman, C. J.; Peng, L.; Luft, J. C.; Madden, A. J.; Wang, A. Z.; Zamboni, W. C. and DeSimone, J. M. *Biomater.* **2013**, *34* (33), 8424-8429.
36. Chu, K. S.; Finniss, M. C.; Schorzman, A. N.; Kuijter, J. L.; Luft, J. C.; Bowerman, C. J.; Napier, M. E.; Haroon, Z. A.; Zamboni, W. C. and DeSimone, J. M. *Nano Lett.* **2014**, *14* (3), 1472-1476.
37. Benhabbour, S. R.; Luft, J. C.; Kim, D.; Jain, A.; Wadhwa, S.; Parrott, M. C.; Liu, R.; DeSimone, J. M. and Mumper, R. J. *J. Control. Release* **2012**, *158* (1), 63-71.
38. Sonavane, G.; Tomoda, K. and Makino, K. *Colloids Surf., B* **2008**, *66*, 274-280.
39. Y. Liu, S. Shah, W. Hu and J. Gao. "Adhesion Dynamics of Functional Nanoparticles for Targeted Drug Delivery", Proceedings of the 25th Southern Biomedical Engineering Conference (IFMBE), **2009**.
40. Natarajan, A.; Wagner, B. and Sibilio, M. *PNAS* **2007**, *104* (43), 17081-17086.



## CHAPTER 4 MEDIATING PASSIVE ACCUMULATION WITH PRINT NANOPARTICLES: EFFECT OF PARTICLE SIZE AND TUMOR MODEL

### 4.1 Introduction

The fundamentals of particle delivery center around two unique parameters of solid tumor vasculature: tortuous and hyper-vasculature circulatory networks allowing macromolecular accumulation and poor lymphatic filtration allowing the carrier to persist within the tumor, notably termed the Enhanced Permeation and Retention (EPR) Effect.<sup>1,2,15</sup> While hypothesized in the 1980's, the academic endeavors are only recently transitioning to clinical benefit and realistically the overall value to this point has been marginal.<sup>3-5</sup> The central roadblock to translational success is not unique to particulates, but, an overarching issue with all novel treatments against disease: the necessity of predictive pre-clinical models. In the case of cancer, recapitulation of human disease is hindered by intrinsic complexity of the diseased tissue due to the heterogeneity in even a single cancerous mass.<sup>6,7</sup>

Similar to normal homogeneous tissue, cancerous tissue requires a blood vessel network that supplies sufficient nutrients, effectively clears waste, and transports oxygen within 100 – 200  $\mu\text{m}$  of growing tissue, a length well within the confines of diffusion.<sup>6,8</sup> However, unlike healthy tissue, diseased and rapidly proliferating tissue undergoes angiogenesis uncontrollably when angiogenic activators (VEGF family, TGF- $\beta$  receptors, PECAM, etc.) are upregulated over angiogenic inhibitors (VEGFR-1, endostatin, vasostatin, etc.) yielding non-uniform and chaotic vasculature that varies drastically over the entire tumor mass; yet, extent of this heterogeneity has been shown to depend on the unique properties of the specific cancer: tumor type, location,

and mass size.<sup>3,8-13</sup> Simultaneously, these attributes affect the extent of EPR that a solid tumor mass presents, leading to major differences in macromolecular accumulation.

The degree of EPR has shown to fluctuate drastically with unique properties of the specific cancer. Along with differences in blood vasculature, the amount of connective tissue (stroma), presence of a lymphatic network, and level of interstitial pressure has all shown to differ among individual cancers.<sup>14-18</sup> These characteristics impact how appropriate a nano-formulation is for a particular cancer type over more traditional small molecule therapy. For instance, pancreatic cancer typically expresses high amounts of stroma, is poorly vascularized, and lacks significant lymphatic drainage.<sup>19,20</sup> While poor lymphatic drainage is beneficial for particle retention, negligible vascularization and extraordinary presence of connective tissue make particulate deposition unlikely. The activity of the mononuclear phagocyte system (MPS) has also shown to fluctuate from cancer to cancer, yielding vastly different particle clearance, affecting blood PK, and overall influencing particle accumulation.<sup>21,22</sup> Finally, fenestrations in the tumor vasculature into and within the diseased mass differs greatly, so, an optimal NP diameter may exist that penetrates most effectively throughout the solid tumor.<sup>5,23-25</sup> In general, a consensus in literature exists that decreasing carrier size will improve tumor deposition.<sup>11,12,25,28-30</sup>

While reducing particle size is generally considered advantageous, tumor deposition and overall performance of the carrier varies throughout literature due to the heterogeneity of nanoparticle systems and disease models.<sup>11,12,25,28-30</sup> In a specific instance, a series of Pt-loaded polymeric micelles (30, 50, 70, and 100 nm) were observed to accumulate equivalently in a highly-permeable subcutaneous murine colon adenocarcinoma model resulting in comparable inhibition of tumor growth. However, the same NP set was tested against a hypopermeable subcutaneous human pancreatic adenocarcinoma model and vastly different accumulation among

the NP sizes was observed. In the poorly vascularized pancreatic model, the two smaller NPs accumulated 2 – 3 times greater than the larger two NPs resulting in vastly improved tumor inhibition for the smaller NPs.<sup>13</sup> In a different research group, gold NPs (AuNPs) were investigated (20, 40, 60, 80, and 100 nm) within a hypervascularized subcutaneous human breast melanoma model resulting in tumor accumulation irrelevant of size, but, dictated by particle half-life in the blood.<sup>26</sup> In a separate research group, an orthotopic model was developed from the same MDA-MB-435 cell line and a series of AuNPs (15, 30, 60, and 100 nm) were once again studied. In this case, AuNPs were observed to accumulate within the diseased tissue in accordance with particle size, with smaller AuNPs leading to enhanced deposition.<sup>27</sup> In these accounts, tumor sequestration was observed to change with cancer type (pancreatic vs. colon vs. breast), model (subcutaneous vs. orthotopic), and in some cases, particle size. The complicated nature of particle tumor deposition highlights just how imperative it is to exhaustively evaluate a carrier.

To this aim, we investigated the effects of nanoparticle size/shape, cancer cell type, and disease model type *in vitro* and *in vivo*. Utilizing PRINT, nanoparticles were manufactured in three distinct sizes: 55 nm x 60 nm, 80 nm x 80 nm x 180 nm, and 80 nm x 80 nm x 320 nm and all were densely PEGylated post-fabrication. *In vitro*, there was no discernable difference in cellular interaction between the nanoparticle types. *In vivo*, biodistribution and blood pharmacokinetic profile were statistically similar among all three NPs in healthy nude mice. Administration of PRINT NPs into four different subcutaneous tumor models showed dramatically different tumor accumulation between the different cancer cell types with evident particle size dependence. Immunohistochemistry (IHC) staining revealed distinct microvessel densities among the four subcutaneous tumors sectioned which seemed to correspond with

overall tumor deposition. Finally, an orthotopic model was tested with three of the cancer cell lines revealing preferential accumulation in primary tumors and metastases over healthy tissue. Overall, tumor accumulation was observed to vary dramatically with particle size, cancer cell line, and disease model.

## 4.2 Results and Discussion

### 4.2.1 Particle Fabrication and Characterization

The fabrication and characterization of hydrogel nanoparticles of sizes 80 nm x 80 nm x 320 nm and 55 nm x 60 nm is identical to details in sections 3.4.2 and 3.4.3. The 80 nm x 80 nm x 180 nm NP was fabricated utilizing the same protocol as the 80 nm x 80 nm x 320 nm particle. In this account, however, isopropanol (instead of methanol) was utilized in all pre-particle solutions as it provided a more uniform thin polymer film. Previously, when using methanol as a solvent, stringent climate control was essential for successful particle fabrication. In previous accounts of fabrication, temperature ranges of approximately 60 – 70 °F and humidity between 10 – 30 % RH were required. Under current procedures utilizing isopropanol, distinct control over temperature and humidity is not necessary assuming typical environmental working conditions (temperature 70-75°F; humidity 10-50% RH). A simple change in pre-particle solvent has given the DeSimone group a more robust fabrication technique that yields an array of diverse nanoparticle types (Figure 4.1 and Table 4.1).

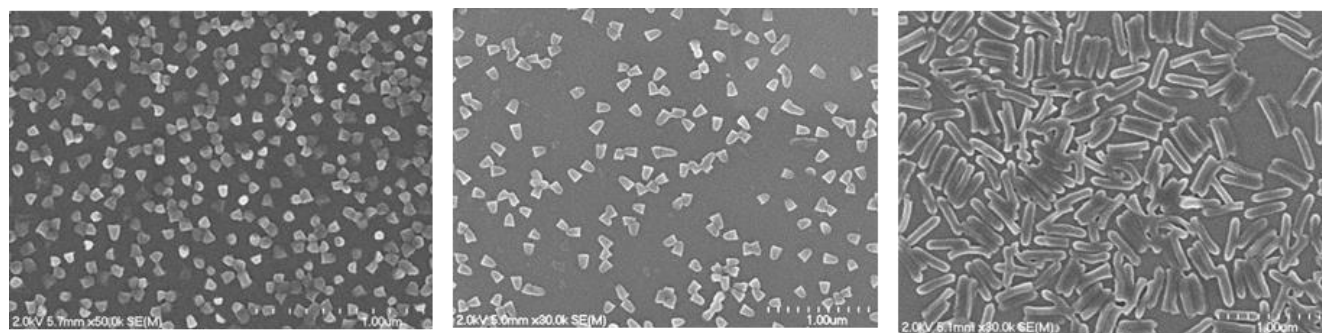


Figure 4.1 Scanning electron micrographs of 55 x 60 nm, 80 x 180 nm, and 80 x 320 nm PRINT hydrogel particles.

Table 4.1 Particle characterization by dynamic light scattering

NP Type (nm)	Z-avg (nm)	PdI	ZP (mV)
55 x 60	126 ± 4	0.09 ± 0.01	-19 ± 1
80 x 180	184 ± 4	0.07 ± 0.01	-20 ± 1
80 x 320	257 ± 5	0.01 ± 0.01	-23 ± 1

#### 4.2.2 Biodistribution and Blood Pharmacokinetics in Healthy Mice

Extending circulation time of nano-based drug delivery systems upon I.V. administration is an important factor facilitating accumulation in cancerous tissue.<sup>26,31</sup> By improving I.V. blood retention, particulate drug systems have a greater probability of permeating into the porous and hyper-vascularized neoplastic tissue. In previous accounts, nanoparticle size has been closely attributed to unique blood pharmacokinetic profiles with smaller particulates extending blood retention.<sup>32,33</sup> In addition, particle size is widely-noted as the most dominant parameter improving solid tumor uptake with decreasing NP size.<sup>11,12,25,28-30</sup> The intertwined relationship of nanoparticle size, blood PK, and tumor accumulation clouds what exact factors lead to improved tumor delivery and due to this complicated relationship, we wanted to conduct blood pharmacokinetic studies in *Foxn1<sup>nu</sup>* mice with PRINT NPs of three distinct sizes: 80 x 320, 80 x 180, and 55 x 60 nm. In all *in vivo* and *in vitro* studies, particles were surface-modified with a dense coating of methoxy-terminated poly (ethylene glycol) that has shown to dramatically enhance circulation time as noted in Chapter 2.<sup>34</sup> Interestingly, blood pharmacokinetic profiles of the three NP types displayed no statistically significant difference in PK behavior (Figure 4.2). Key pharmacokinetic parameters for different NP sizes such as circulation half-life ( $t_{1/2}$   $\beta$ ), volume of distribution ( $V_d$ ), and area-under-curve (AUC) all fell within statistically similar values of approximately 13-20 hours, ~1.3 mL, and 15 mg/mL·h, respectively (Table 4.2). These

results may indicate that any differences in tumor accumulation can be attributed to size and not a different pharmacokinetic behavior. Biodistribution upon organ resection revealed similar deposition between main tissues for nanoparticle clearance for all NP types (Figure 4.3) with slight dependence on NP size observed within the kidneys.

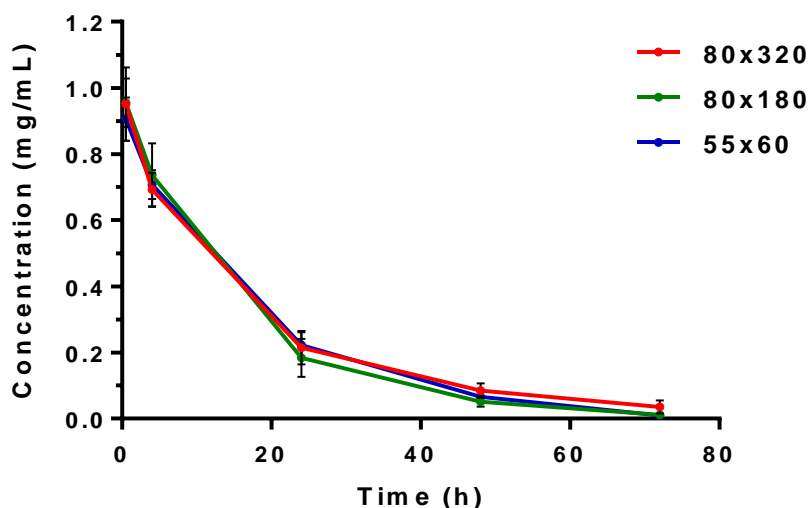


Figure 4.2 Blood pharmacokinetics of three NP types in healthy mice at several time points: 0.5, 4, 24, 48, and 72 h (n = 5 per NP arm).

Table 4.2 Blood pharmacokinetics as a function of a nanoparticle type

	55 x 60	80 x 180	80 x 320
$t_{1/2 \alpha}$ (h)	$4.0 \pm 4.4$	$7.7 \pm 3.1$	$4.5 \pm 1.9$
$t_{1/2 \beta}$ (h)	$12.8 \pm 1.4$	$14.7 \pm 2.9$	$20.3 \pm 7.3$
$V_d$ (mL)	$1.4 \pm 0.1$	$1.3 \pm 0.1$	$1.3 \pm 0.2$
CL (mL/h)	$0.08 \pm 0.01$	$0.09 \pm 0.02$	$0.08 \pm 0.01$
$AUC_{0-t}$ (mg/mL·h)	$15.4 \pm 1.9$	$14.3 \pm 3.0$	$14.6 \pm 1.3$

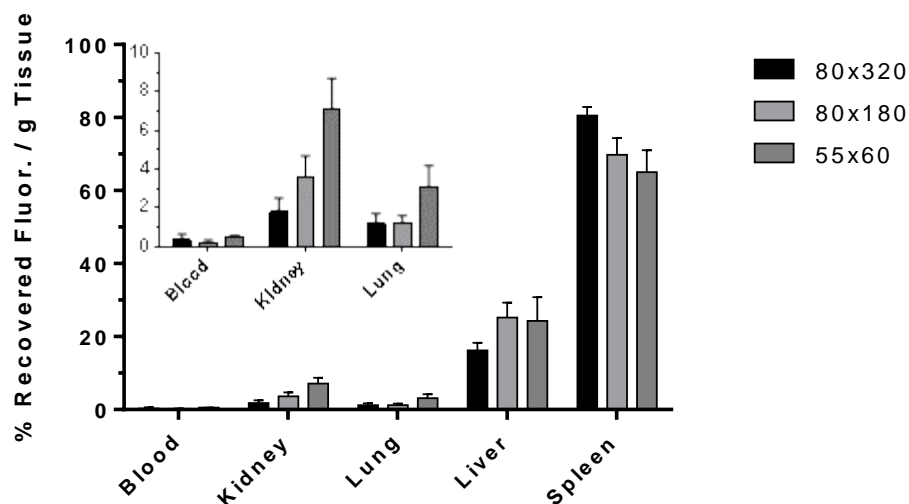


Figure 4.3 Biodistribution of 55 x 60, 80 x 180, and 80 x 320 nm in healthy mice at 24 hour post-injection at 60 mg / kg (n = 4).

#### 4.2.3 In Vitro Assessment of NPs

While blood pharmacokinetic profile and biodistribution of the three different PRINT hydrogels were similar, it was of interest to validate *in vitro* behavior. The DeSimone lab has previously shown major differences in cellular interactions based nanoparticle shape. In these accounts, high aspect ratio nanoparticles were shown to internalize at a faster rate in HeLa cells, yet, it is of significance to note said particles exhibited a strong positive charge facilitating this interaction.<sup>35</sup> In current studies, the densely PEGylated nanoparticles exhibited a negative surface charge as previously shown in Table 4.1 and all nanoparticle sizes poorly associated with the cancer cell lines of interest (Figure 4.4) after a 24 h incubation period. As expected, phagocytic alveolar murine macrophage associated with all three nanoparticles types at approximately 20-30 % association after 24 h which is similar to previously described findings (See Figure 2.5). Overall, the PEG-coating paired with the negative surface charge of the various NPs seemed to effectively shield interaction with non-phagocytic cancer cells no matter the particle shape.

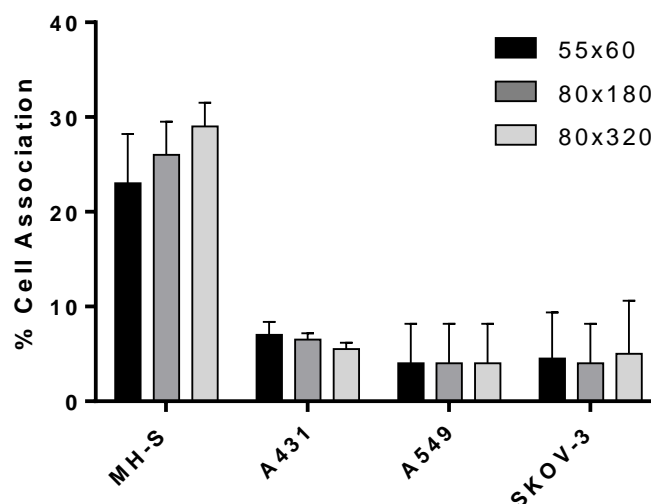


Figure 4.4 *In vitro* cell association of various NP types with murine macrophages (MH-S) and three different cancer cell types (A431, A549, and SKOV-3).

#### 4.2.4 NP Distribution in Flank Tumor Models and Immunohistochemistry

Pre-clinical animal models that accurately predict behavior in a clinical setting is perhaps the greatest current challenge in drug development.<sup>3,36</sup> Improper or incomplete validation of nano-based drug delivery methods by non-predictive animal models and inappropriate assessment of success pre-clinically can be tied to wasted endeavors in early clinical development.<sup>36,37</sup> Needless to state, it is of dire circumstance that a nanotherapy is exhaustively validated in a number of disease models prior to adorning it efficacious. In an effort to validate the impact of various PRINT NPs towards solid tumor delivery, we analyzed accumulation in several murine flank tumor models. While flank tumor models are hardly predictive in nature, they are frequently used in nanoparticle drug delivery literature to test how well the carrier deposits within solid tumor tissues. The aim of these studies was to determine how tumor accumulation varied across different flank tumor models and then determine how these findings translated to more predictive orthotopic cancer models.



Mice were injected subcutaneously in the right flank with either A549 (human non-small cell lung cancer cells), A431 (human epidermoid cancer cells), SKOV3 (human ovarian cancer cells) or 344SQ (mouse non-small cell lung cancer cells). When flank tumors reached  $\sim 100 \text{ mm}^3$ , mice were injected (tail vein) with either 80 nm x 320 nm, 80 nm x 180 nm, or 55 nm x 60 nm PRINT particles. Particle biodistribution was assessed 24 hours post NP injections via organ resection and fluorescent imaging. Upon fluorescence analysis, it was evident that both nanoparticle size and disease type/model had drastic effects on overall accumulation in the solid flank tumors (Figure 4.5). The 55 x 60 nm particle out performed all particle types in the A431, SKOV3, and 344SQ flank tumor models. Interestingly, in the A549 flank tumor model, the 55 nm x 60 nm and the 80 nm x 180 nm particles performed statistically the same. In most cases, a positive correlation existed between reductions in NP size and flank accumulation; however, it is currently unknown whether pore cutoff size in the tumor vasculature is the main driver of this observation. In three of four flank models (SKOV3, A431, and A549) tumor deposition ranged from  $\sim 3\text{-}15\%$  depending on the NP type, yet, the 344SQ tumor model yielded significantly increased deposition between  $\sim 15\text{-}38\%$ . Biodistribution in flank tumor-bearing mice displayed similar distributions throughout the four models with slight variations in spleen and liver delivery (Figure 4.6). It is reasonable to assume that alterations in biodistribution between model types can at least in part be attributed to differences in tumor depot as biodistribution in healthy mice was statistically similar.

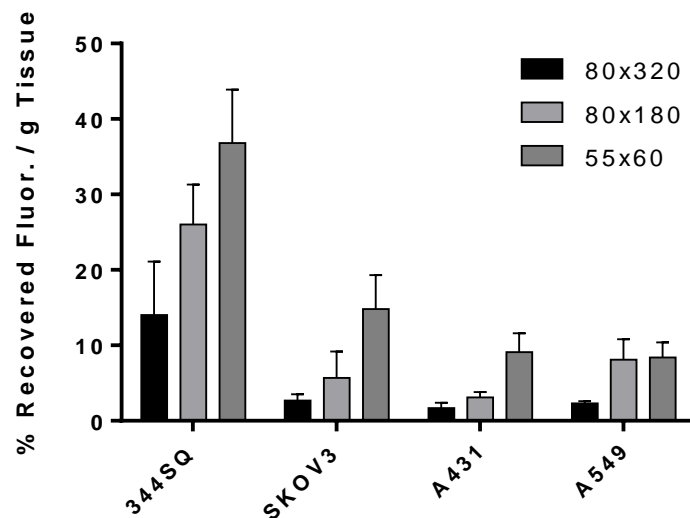


Figure 4.5 Flank tumor accumulation of PRINT particles of various sizes and shapes was evaluated at 24 h post-injection at 60 mg/kg. Data displayed as percent recovered fluorescence per gram of tissue (n = 4).

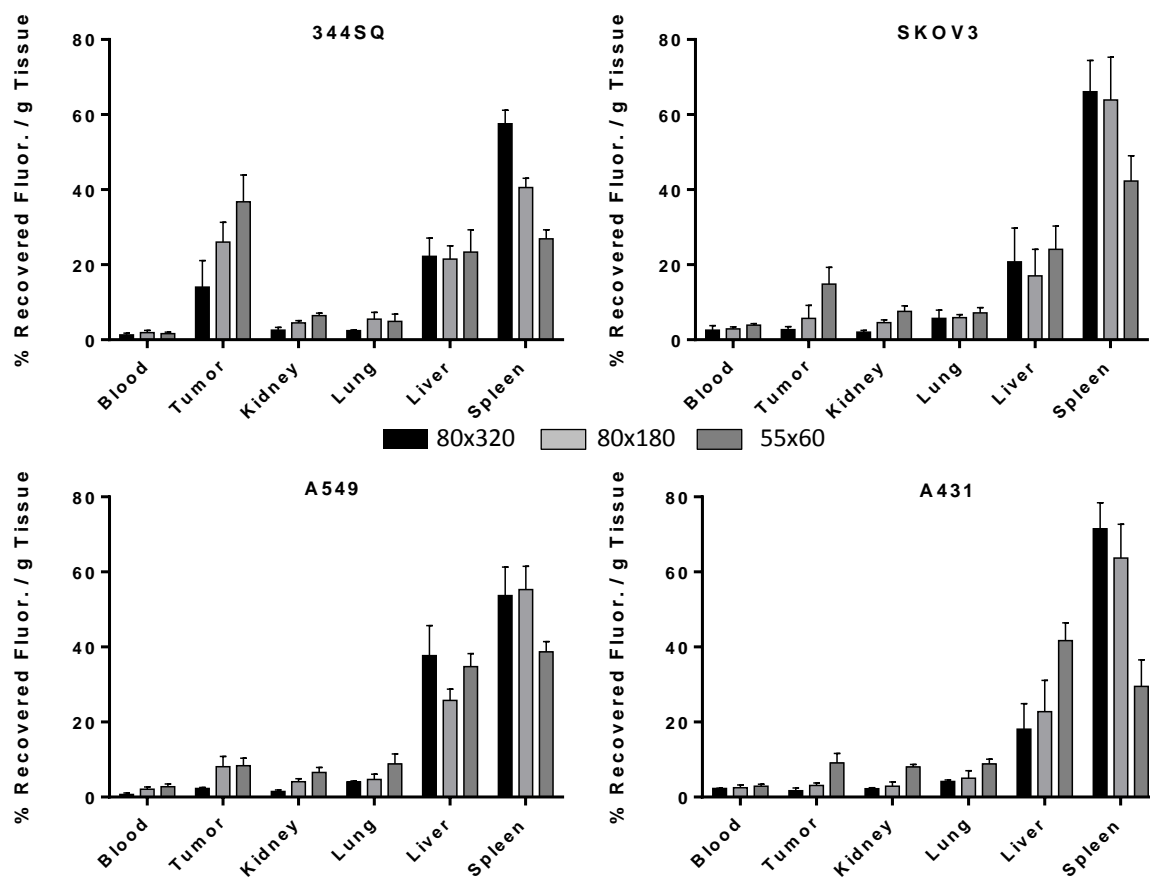


Figure 4.6 Biodistribution of NPs at three distinct sizes in four different tumor-bearing mouse models at 24 h post-injection (60 mg / kg). Organs of interest were resected and fluorescently imaged (n = 4).

Upon resection of flank tumors and fluorescent imaging, visual differences were noted and immunohistochemistry was conducted to determine variance in cell surface markers and tumor vascularization. Upon visual inspection, A431 flank tumors seemed to be more vascularized than the A549 and SKOV-3 tumor tissues (Figure 4.7). Upon fixation, sectioning, and staining the microvessel density, as identified with a CD-31 endothelial cell marker, seemed to vary across the different flank tumors 344SQ > SKOV3 > A431 > A549 (Figure 4.8). This finding was corroborated with complete vessel, endothelial vasculature coupled with lumen, in the same manner. Interestingly, the microvessel density seemed to align well with overall flank tumor deposition of NPs. Lymphatic tissue (Lyve1), tumor-associated macrophage (TAMs; F4/80), collagen (Collagen IV), and vascular endothelial growth factor (VEGF) markers were also utilized during IHC staining (Figure 4.9). The highest expression of collagen and TAMs were observed with the 344SQ and A549 cell lines while lymphatic tissue and VEGF seemed equivalent across all sections. In previous accounts, high collagen expression is associated with poor tissue vascularization which in thought would lead to low NP tumor deposition.<sup>38</sup> In this account, however, both microvessel density and collagen expression are the highest for the 344SQ flank model which displayed the highest NP tumor depot. While it is not clear at this time what accounts for this discrepancy, there seems to be a stark difference in microvessel density, collagen, and TAMs across the different flank models.

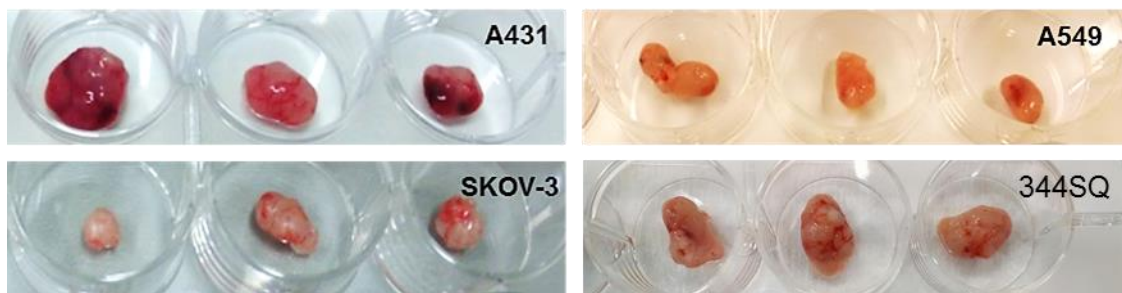


Figure 4.7 Photographs of different flank tumors once resected from the mouse.

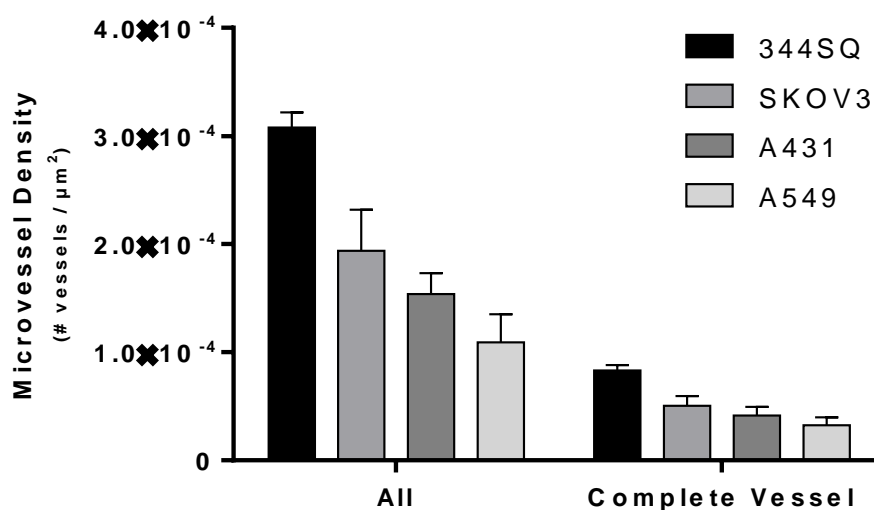


Figure 4.8 Immunohistochemistry analysis of parafilm-fixed flank tumors. Vascularization of the cancerous tissue was identified with a CD-31 marker. Complete vessel is defined as endothelial tissue coupled with lumen.

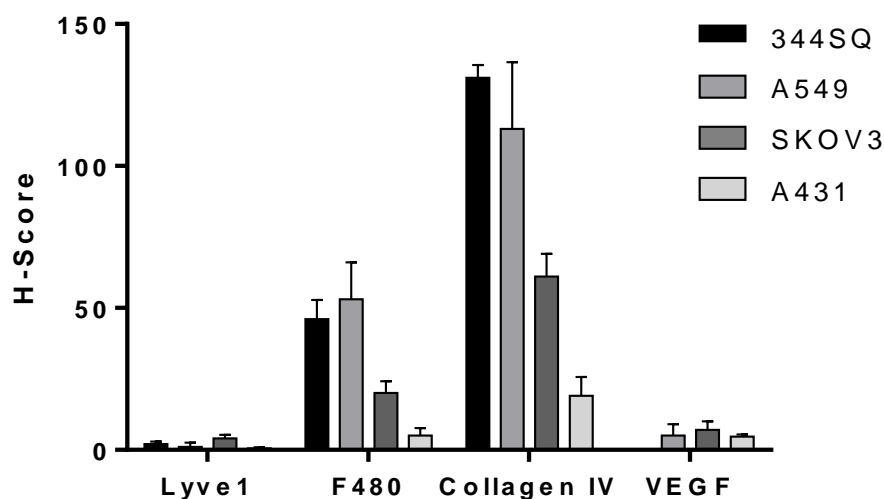


Figure 4.9 Immunohistochemistry analysis of parafilm-fixed flank tumors with several markers: lymphatic vessel (Lyve1), tumor-associated macrophage (F480), collagen (Collagen IV), and vascular endothelial growth factor (VEGF).

#### 4.2.5 NP Distribution in Orthotopic Tumor Models

Assessment of drug or drug carrier performance in clinically relevant pre-clinical models is imperative to ascertain potential success. While there are obvious limitations translating discoveries from mice to humans, there are certain mouse models that better reflect human cancer pathology.<sup>39,40</sup> In line with this, it should be noted that while enhanced deposition of a

carrier to a flank tumor may reflect potential benefits in drug delivery, the clinical course of action for a large solid mass would traditionally be surgery followed by radiation/chemo therapy. In light of this, nanoparticle therapies may be better suited to aid in cancer treatment if they could preferentially target metastatic disease over healthy tissue. To this aim, particle deposition into three different metastatic orthotopic mouse models was investigated: 344SQ (lung), A549 (lung), and SKOV3 (ovarian).

The deposition of 55 x 60 nm PRINT NPs was assessed in three different orthotopic mouse models that were also prone to metastatic growth. In these studies, a preferential deposition of the hydrogel carrier was observed in the primary tumor and metastatic tissue over healthy tissue. In the A549 lung model, disease was apparent at the primary injection site post-surgery along with significant lymphatic disease. In the 344SQ lung model, disease was observed in the lung tissue and several metastases formed in the lymph nodes, pleural cavity, and along the chest wall (Figure 4.10 and Figure 4.13). Fluorescent images from the primary lung tumors display, in a compelling fashion, dramatic particle accumulation in the diseased sites in comparison to surrounding healthy lung tissue. The ovarian model displayed significant disease in the intraperitoneal cavity along with metastases in the liver (Figure 4.11). As seen in Figure 4.12, particle distribution in the three orthotopic models does not necessarily reflect what was previously observed in the flank models, most notably the drastic variance between the A549 cell-line. As well, it was surprising that particle accumulation in the diseased tissue was so high, ranging from 20 – 50% (Figure 4.12 D). In general, particle distribution was observed in all metastatic disease throughout each model albeit at different extents (Figure 4.13). The establishment of more clinically relevant mouse models along with the preferential delivery of a particle carrier bodes well for the use of PRINT in a clinical setting. Nevertheless, only with the

incorporation of chemotherapeutic and subsequent advancements in efficacy of that therapeutic can we establish the success of this carrier.

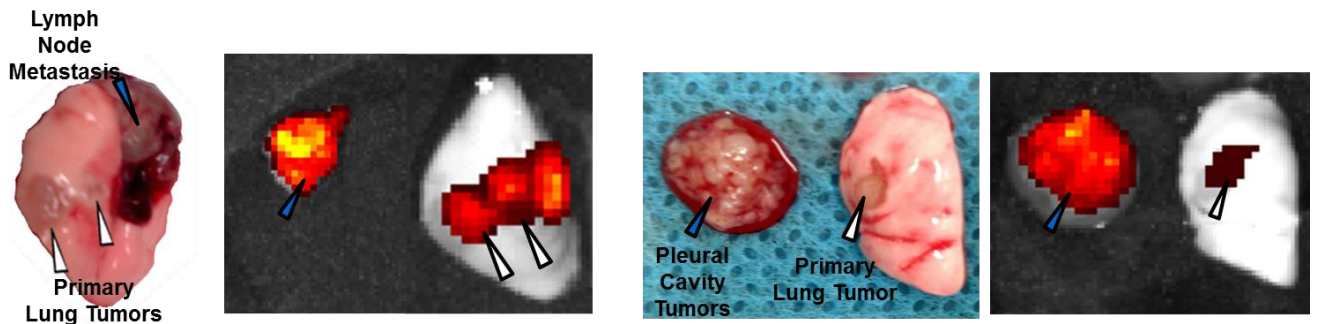


Figure 4.10 Photograph and fluorescence images of orthotopic 344SQ (left two) and A549 (right two) tumors treated with fluorescently labeled PRINT particles indicating preferential accumulation of particles in diseased tissue. White triangles indicate primary tumors, and blue triangles indicate either lymph node metastasis or pleural cavity tumors.

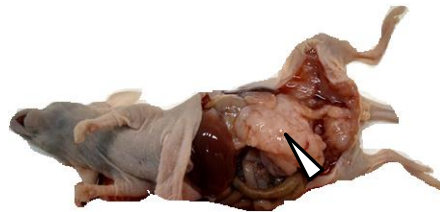


Figure 4.11 Representative photograph of orthotopic SKOV-3 tumors (indicated by the white triangle) formed in the IP cavity of a nude mouse.

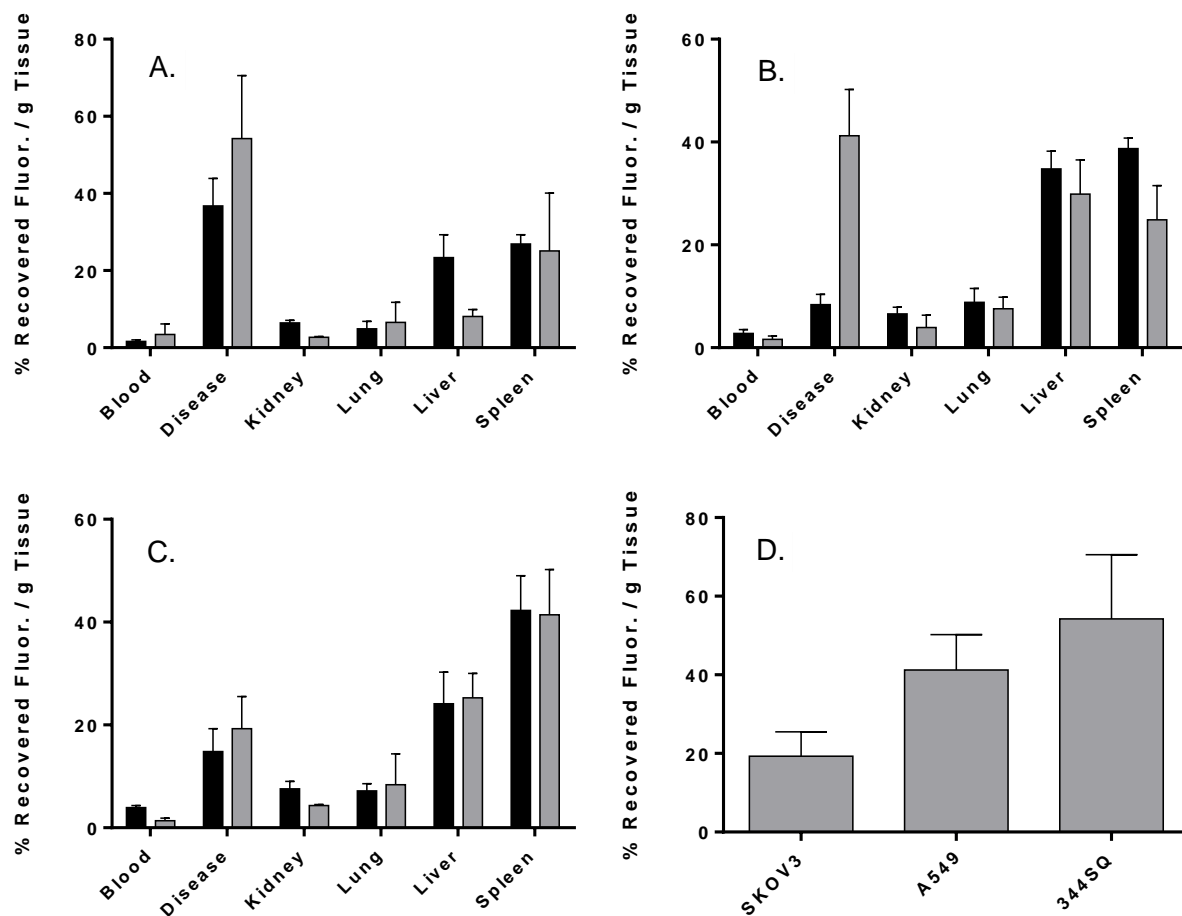


Figure 4.12 Biodistribution of 55 x 60 nm particles in tumor-bearing mice 24 h post-injection (60 mg / kg). Organs of interest were resected and imaged via fluorescence. Both orthotopic (gray bar) and flank (black bar) tumor models were investigated for the following cell lines (A) 344SQ, (B) A549, (C) SKOV3. Total fluorescence of diseased tissue was compared in orthotopic models (D).

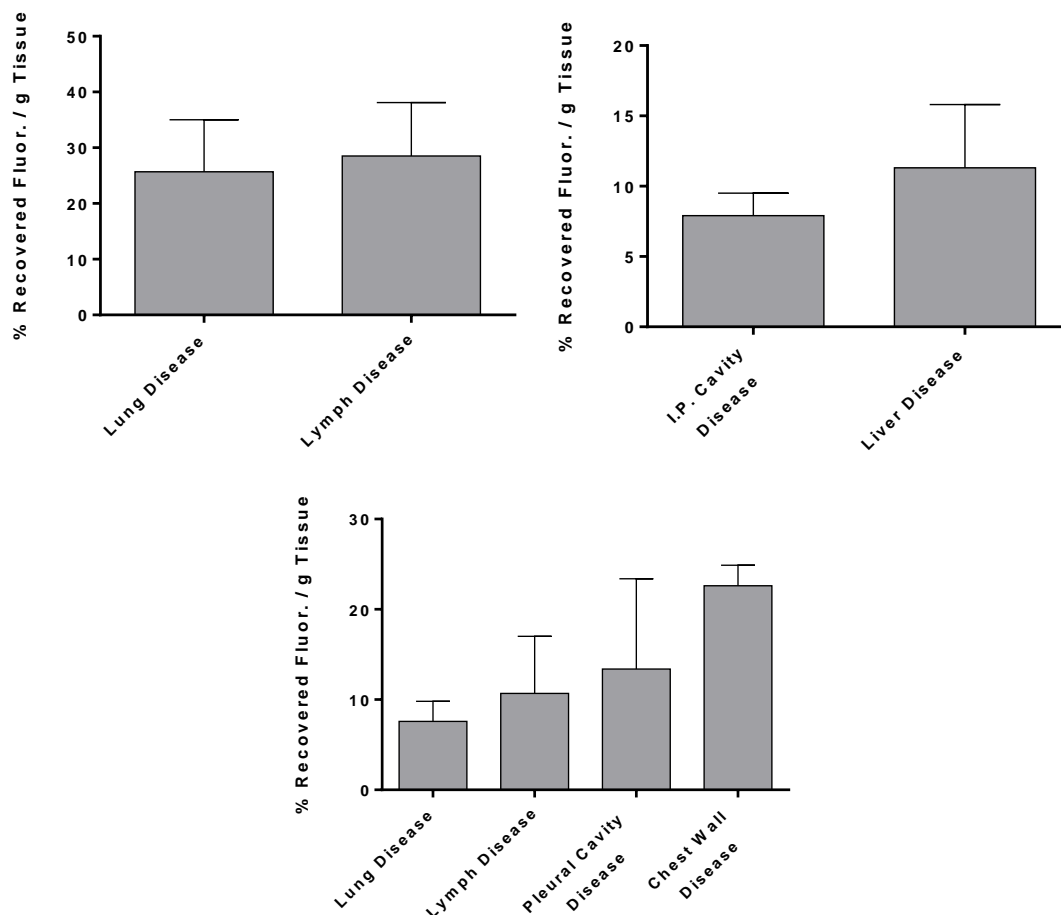


Figure 4.13 Biodistribution of 55 x 60 nm particles in metastatic disease sites throughout the three orthotopic mouse models: A549 (top-left), SKOV-3 (top-right), and 344SQ (bottom).

### 4.3 Conclusions

In this account, we utilized PRINT to manufacture hydrogel particles of various sizes/shapes to examine how NP size, tumor cell-line, and tumor location affect particle sequestration in cancerous tissue. The three different particle types: 80 nm x 80 nm x 320 nm, 80 nm x 80 nm x 180 nm, and 55 x 60 nm were surface-modified with a dense brush of poly(ethylene glycol) and exhibited a negative surface charge which in tandem has shown to dramatically enhance blood retention, macrophage resistance, and protein resistance. Unlike previous accounts, the various particle sizes exhibited similar blood pharmacokinetic behavior, association with cancerous cells, and resistance to macrophage uptake. Four flank tumor mouse



models were tested for particulate accumulation revealing vastly different deposition among the different particle types and models. The IHC staining displayed stark differences in the different flank models with microvessel density, collagen, and TAMs varying among the solid tumors. Upon administration of the 55 nm x 60 nm particle into orthotopic tumor models, significant accumulation was observed in both primary and metastatic sites. While preferential metastatic accumulation of PRINT nanoparticles is encouraging, we will not know the true impact until a potent chemotherapeutic is incorporated and efficacy studies are carried out in a number of clinically translatable models.

#### 4.4 Materials and Methods

##### 4.4.1 Materials

2-aminoethyl methacrylate hydrochloride (AEM), diphenyl (2,4,6-trimethylbenzoyl) phosphine oxide (TPO), poly (ethylene glycol) diacrylate ( $M_n$  700) (PEG<sub>700</sub>DA), trypsin, ethylenediaminetetraacetic acid (EDTA), and sucrose were obtained from Sigma-Aldrich. Thermo Scientific Dylight 488, 650, and 680, Thermo Scientific HyClone fetal bovine serum (FBS), triethylamine (TEA), acetic anhydride, isopropanol, sterile water, dimethylformamide (DMF), Dulbecco's phosphate buffered saline (pH 7.4) (DPBS), 1X phosphate buffered saline (pH 7.4) (PBS), and Dulbecco's Modified Eagle's Medium (DMEM) were purchased from Fisher Scientific. Methoxy-PEG5k- succinimidyl carboxy methyl ester (mPEG5k-SCM) was obtained from Creative PEGWorks (Winston Salem, NC). Polyvinyl alcohol ( $M_w$  2000) (PVOH) was bought from Acros Organics. Murine alveolar macrophage (MH-S), human epidermoid carcinoma (A431), and human ovarian adenocarcinoma (SKOV3) cells were purchased from American Type Culture Collection. Murine lung adenocarcinoma (344 SQ) and human non-small cell lung carcinoma (A549) were graciously provided by the laboratories of Dr. Chad

Pecot. PRINT molds (80 nm x 80 x 320 nm, 80 nm x 80 nm x 180 nm, and 55 x 60 nm) were all acquired from Liquidia Technologies. As described in previous accounts, tetraethylene glycol monoacrylate (HP<sub>4</sub>A) was synthesized in-house.<sup>41</sup> For all immunohistochemistry and staining, rabbit polyclonal antibodies against CD31 (ab28364) and Lyve1 (ab14917) were from Abcam (Cambridge, MA), Collagen IV (AB8201) from EMD Millipore (Billerica, MA), and VEGF (sc-152) from Santa Cruz Biotechnology (Dallas, Texas). Rat monoclonal antibody F4/80 (clone BM8, # 14-4801-82) was from eBioscience Inc. (San Diego, CA).

#### 4.4.2 Nanoparticle Fabrication

The fabrication of 55 x 60 nm and 80 x 320 nm PRINT nanoparticles was fairly similar to previous methods as described in sections 2.4.2 and 3.4.2. Instead of methanol as the pre-particle solvent, isopropanol was utilized in effort to create a polymer film less dependent on temperature and humidity conditions. For the 80 x 80 x 180 nm particle, a Teflon-like PRINT mold (as provided by © Liquidia Technologies) was utilized and the fabrication procedure was equivalent to the 80 x 320 nm NP type. In addition, purification procedures for the 80 x 320 nm and 55 x 60 nm types were kept consistent to previous descriptions and only alteration for the 80 x 180 nm type was the centrifuge time (45 – 90 minutes).

#### 4.4.3 Nanoparticle Characterization

The nanoparticles were characterized by dynamic light scattering, thermal gravimetric analysis, and atomic force microscopy as previously described in sections 2.4.3 and 3.4.3. However, minor alterations were made to the scanning electron microscopy imaging protocol. The microscopy sample preparation was changed to reduce swelling of the hydrogel matrix prior to SEM analysis resulting in vastly improved images. Before SEM analysis, a particle solution in N,N-dimethylformamide was diluted further in DMF to 50 µg/mL and 1 µL of that solution was

pipette onto a clean silicon wafer. The solvent was allowed to evaporate from the wafer overnight and dried further with a heat gun. The sample was allowed to cool to room temperature and imaged immediately thereafter.

#### 4.4.4 Surface Modification for *In Vitro* and *In Vivo* Experiments

After the nanoparticles were purified in sterile water, the suspension was washed into DMF (3x) using the centrifugation method (14,000 RPM; 0.5 to 3 h). In effort synthesize NPs for large-scale *in vivo* studies, modification procedures were effectively scaled-up by five-fold. The concentration was assessed by TGA and the particles were concentrated (5 mg / mL). The particle solution (5 mg; 4.3 mg/mL) was reacted with TEA (100  $\mu$ L), methoxy-PEG<sub>5k</sub>-SCM (140  $\mu$ L; 100 mg / mL in DMF), and left to react overnight. The reaction mixture was washed once in DMF and unreacted amines were quenched with addition of pyridine (50  $\mu$ L), acetic anhydride (70  $\mu$ L), and shaken at room temperature for 30 minutes. The mixture was washed once in DMF, once in pH 9.5 borate buffer, and sterile water (3x). Following surface modification of all three nanoparticle types, the particles were fully characterized by methods previously described.

#### 4.4.5 Cellular Association Studies

Cell association studies were conducted with identical procedures for each individual cell type as outlined in sections 3.4.7 and 3.4.8. In these experiments three distinct particle sizes were tested against four different cell lines: murine alveolar macrophage (MH-S), human non-small cell lung carcinoma (A549), human ovarian adenocarcinoma (SKOV-3), and human epidermoid carcinoma (A431). As noted before, cell association was assessed via FACS analysis.

#### 4.4.6 In Vivo Studies

All animal studies were carried out with the approved protocol by The University of North Carolina Animal Care and Use Committee. In all mouse models, female athymic nudes

(*Foxn1<sup>nu</sup>*; 20- 30 g) were dosed with a 60 mg / kg tail vein injection from an 8 mg /mL nanoparticle suspension in a 9.25 wt% sucrose solution.

PRINT NPs of three distinct sizes were administered into healthy female mice in effort to determine how nanoparticle size alters biodistribution and blood pharmacokinetics. For these studies, surface-modified 55 x 60, 80 x 180, and 80 x 320 nm NPs were injected via tail-vein (n = 5 per NP arm). At each time point (0.5, 4, 24, 48, and 72 h), whole blood (20-30  $\mu$ L per time point) was collected via tail nick directly into a heparinized Eppendorf tube and stored at 4°C until the final time point was collected. At 72 hours, mice were euthanized and sacrificed via cardiac-puncture and cervical dislocation. Organs of interest were collected (spleen, liver, lungs, kidneys) and blood from the cardiac puncture was utilized as the last blood PK time point. Whole blood (15  $\mu$ L) from all time points was diluted into sterile water (135  $\mu$ L), thoroughly shaken, and 100  $\mu$ L was pipette into an opaque 96-well plate. A standard curve was created by diluting a small aliquot (10  $\mu$ L) of each NP type into freshly harvested blood from control mice (n = 3 per NP arm) in order to normalize the fluorescence between NPs. Fluorescence measurements were taken from organs and blood as previously described in sections 2.4.9 and 3.4.9. In these studies, PK Solver 2.0 was utilized to determine important pharmacokinetic parameters as in section 3.4.9.

For flank tumor studies, mice were aged 6 – 8 weeks and injected in the right rear flank with tumor cells. Mice were inoculated with one of four cell lines: 5 x 10<sup>6</sup> SKOV3 cells in 1X PBS, 5 x 10<sup>6</sup> A549 cells in 1 x PBS, 2 x 10<sup>6</sup> A431 cells in DMEM, or 1 x 10<sup>5</sup> 344SQ cells in 1 x PBS. Tumor growth was measured twice weekly via caliper measurements. When tumors reached ~150 mm<sup>3</sup> mice were injected with one of three NP types and 24 hours later mice were sacrificed, harvested, and fluorescently imaged. For greater detail of flank tumor biodistribution

studies reference sections 2.4.9 and 3.4.9. For orthotopic tumor studies, lung cancer cells were implanted via intra-thoracic injection into either female nude (A549 cells) or female SvJ mice (344SQ cells) at six weeks of age. Mice were inoculated with either  $1 \times 10^6$  A549 cells or  $1 \times 10^5$  344SQ cells (1:1 ratio of Hank's media and BD Matrigel) and disease progression was monitored by weight gain/loss and overall health of mouse. Luciferase-expressing SKOV3 cells ( $1 \times 10^6$ ) were resuspended in 200  $\mu$ L 1X PBS and injected with a 25 gauge needle IP into female nude mice and disease progression was monitored by bioluminescence. At 4 weeks post-inoculation (lung cancer models) and 13 weeks (ovarian cancer model), mice were dosed with fluorescently-labeled 55 x 70 nm particles. Mice were once again euthanized, sacrificed/harvested, and imaged at 24 hours with methods previously noted.

#### 4.4.7 Immunohistochemistry Analysis

Flank tumors were harvested from mice once they reached 150 mm<sup>3</sup>; they were fixed in formalin and processed by the University of North Carolina's Translational Pathology Laboratory (TPL). Immunohistochemistry analysis was carried in the Bond fully-automated slide staining system (Leica Bicrosystems Inc. Vist, CA). Slides were deparaffinized in Bond dewax solution (AR9222) and hydrated in Bond wash solution (AR9590). Antigen retrieval was performed at 100°C in Bond-epitope retrieval solution 1 [pH-6.0] (AR9961) for Collagen IV and F4/8 (20 minutes), VEGF and Lyve1 and CD31 (30 minutes). Bond-epitope retrieval solution 1 (20 min) or Bond enzyme 1 (5 min, AR9551) for F4/80. After pretreatment, CD-31 (1:50), VEGF (1:100), F4/80 (1:50), Lyve1 were applied for 1 h and Collagen IV for 30 min. Detection of F4/80 was performed using Bond Intense R Detection System (DS9263) supplemented with the biotinylated goat anti-Rat IgG (ab7096, Abcam). The rest of were supplemented with Bond

polymer refine detection system (DS9800). Stained slides were dehydrated and cover-slipped. Positive and negative controls (no primary antibody) were included for each antibody.

Sections were digitally imaged (20X objective) in the Aperio ScanScope XT using line-scan camera technology (Leica Biosystems). Digital images were stored and analyzed with Aperio eSlide Manager Software. Tumor areas were circled on each slide using Aperio positive pen tool. Tumor identification was guided by H&E slide. Collagen IV and VEGF signal was quantified using Aperio color deconvolution algorithm version 9. This algorithm calculates the area and intensity for the positive stain and generates Score (0-300). Aperio membrane v9 algorithm was used for F4/80 and Lyve1 positive cells, and microvessel v1 for CD31. These procedures were kindly provided by Nana Feinberg of TPL.

#### 4.5 References

1. Matsumura, Y. and Maeda, H. *Cancer Res.* **1986**, *46*, 6387-6392.
2. Hashizume, H.; Baluk, P.; Morikawa, S.; McLean, J. W.; Thurston, G.; Roberge, S.; Jain, R. K. and McDonald, D. M. *Am. J. Pathol.* **2000**, *156* (4), 1363-1380.
3. Prabhakar, U.; Maeda, H.; Jain, R. K.; Sevic-Muraca, E. M.; Zamboni, W.; Farokhzad, O. C. Barry, S. T.; Gabizon, A.; Grodzinski, P. and Blakey, D. C. *Cancer Res.* **2013**, *73*(8), 2412-2417.
4. Nichols, J. W. and Bae Y. H. *J. Control. Release* **2014**, *190*, 451-464.
5. Jain, R. K. and Stylianopoulos, T. *Nat. Rev. Clin. Oncol.* **2010**, *7*, 653-664.
6. Nagy, J. A.; Chang, S.; Shih, S.; Dvorak, A. M. and Dvorak, H. F. *Semin. Thromb. Hemost.* **2010**, *36* (3), 321-331.
7. Isaiah J. Fidler. *Cancer Res.* **1978**, *38*, 2651-2660.
8. Judith Folkman. *Nat. Med.* **1995**, *1* (1), 27-31.
9. Gasparini, G.; Longo, R.; Toi, M. and Ferrara, N. *Nat. Clin. Prac. Oncol.* **2005**, *2* (11), 562-577.
10. Bao, L.; Matsumura, D.; Baban, D.; Sun, Y. and Tarin, D. *Br. J. Cancer* **1994**, *70*, 228-232.
11. Xiao, K.; Luo, J.; Li, Y.; Xiao, W.; Lee, J. S.; Gonik, A. M. and Lam, K. S. *Nanosci. Nanotechnol. Lett.* **2010**, *2* (2), 79-85.
12. Frieboes, H.; Wu, M.; Lowengrub, J.; Decuzzi, P. and Cristini, V. *PLOS One* **2013**, *8* (2), 56876.
13. Cabral, H.; Matsumoto, Y.; Mizuno, K.; Chen, Q.; Murakami, M.; Kimura, M.; Terada, Y.; Kano, M. R.; Miyazono, K.; Uesaka, M.; Nishiyama, N. and Kataoka, K. *Nat. Nanotechnol.* **2011**, *6*, 815-823.
14. Eberhard, A.; Kahlert, S.; Goede, V.; Hemmerlein, B.; Plate, K. H. and Augustin, H. G. *Cancer Res.* **2000**, *60*, 1388-1393.
15. Noguchi, Y.; Wu, J.; Duncan, R.; Strohalm, J.; Ulbrich, K.; Akaike, T. and Maeda, H. *Jpn. J. Cancer Res.* **1998**, *89*, 307-314.

16. Padera, T. P.; Kadambi, A.; Tomaso, E.; Carreira, C. M.; Brown, E. B.; Boucher, Y.; Choi, N. C.; Mathisen, D.; Wain, J.; Mark, E. J.; Munn, L. L. and Jain, R. K. *Science* **2002**, 296, 1883-1885.
17. Jain, R. K. and Fenton, B. T. *J. Nat. Cancer Inst.* **2002**, 94 (6), 417-421.
18. Boucher, Y.; Baxter, L. T. and Jain, R. K. *Cancer Res.* **1990**, 50, 4478.
19. Uster, P. S.; Working, P. S. and Vaage, J. *Int. J. Pharm.* **1998**, 162, 77-86.
20. Kano, M. R.; Bae, Y.; Iwata, C.; Morishita, Y.; Yashiro, M.; Oka, M.; Fujii, T.; Komuro, A.; Kiyono, K.; Kaminishi, M.; Hirakawa, K.; Ouchi, Y.; Nishiyama, N.; Kataoka, K. and Miyazono, K. *PNAS*. **2007**, 104, 3460-3465.
21. Reiche, E. M. V.; Nunes, S. O. V. and Morimoto, H. K. *Lancet* **2005**, 5, 617-625.
22. Visser, K. E.; Eichten, A. and Coussens, L. M. *Nat. Rev. Cancer* **2006**, 6, 25-37.
23. Hobbs, S. K.; Monsky, W. L.; Yuan, F.; Goberts, W. G.; Griffith, L.; Torchilin, V. P. and Jain, R. K.. *PNAS* **1998**, 95 (8), 4607-4612.
24. Jain, R. K.; Munn, L. L. and Fukumura, D. *Nat. Rev. Cancer* **2002**, 2, 266-276.
25. Yuan, F.; Dellian, M.; Fukumura, D.; Leunig, M.; Berk, D. A.; Torchilin, A. P. and Jain, R. K. *Cancer Res.* **1995**, 55, 3752-3756.
26. Perrault, S. D.; Walkey, C.; Jennings, T.; Fischer, H. C. and Chan, W. C. W. *Nano. Letters* **2009**, 9 (5), 1909-1915.
27. Sykes, E. A.; Chen, J.; Zheng, G. and Chan, W. C. W. **2014**, *ACS Nano*, 8 (6), 5696-5706.
28. Huo, S.; Ma, H.; Huang, K.; Liu, J.; Wei, T.; Jin, S.; Zhang, J.; He, S. and Liang, X. *Cancer Res.* **2012**, 73(1), 1-12.
29. Sonavane, G.; Tomoda, K. and Makino, K. *Coll. Surf. B Biointer.* **2008**, 66, 274-280.
30. Ding, Y.; Li, S. and Nie, G. *Nanomed.* **2013**, 8 (7), 1209-1222.
31. Alexis, F.; Pridgen, E.; Molnar, L. K.; Farokhzad, O. C. *Mol. Pharmaceutics* **2008**, 5 (4), 505-515.
32. Chouly, C.; Pouliquen, D.; Lucet, I.; Jeune, J. J. and Jallet, P. *J. Microencapsulation* **1996**, 13(3), 245-255.
33. He, C.; Hu, Y.; Yin, L.; Tang, C. and Yin C. *Biomater.* **2010**, 32 (13), 3657-3666.



34. Perry, J. L. and Reuter, K. G.; Kai, M. P.; Herlihy, K. P.; Jones, S. W.; Luft, J. L.; Napier, M.; Bear, J. E. and DeSimone, J. M. *Nano Lett.* **2012**, *12* (10), 5304-5310.
35. Gratton, S.E.A., Ropp, P. A.; Pohlhaus, P. D.; Luft, J. C.; Madden, V. J.; Napier, M. E. and DeSimone, J. M. *PNAS*, **2008**, *105* (33), 11613-11618.
36. Eliasof, S.; Lazarus, D.; Peters, C. G.; Case, R. I.; Cole, R. O.; Hwang, J.; Schluep, T.; Chao, J.; Lin, J.; Yen, Y.; Hand, H.; Wiley, D. T.; Zuckerman, J. E. and Davis, M. E. *PNAS* **2013**, *110* (37), 15127-15132.
37. Lammers, T.; Kiessling, F.; Hennink, W. E. and Storm, G. *J. Control. Release* **2012**, *161* (2), 175-187.
38. Kloppel, G. Pathology of Non-endocrine Pancreatic Tumors. In: V.L.W. Go, E.P., DiMagno, J.D. Gardner, E. Lebenthal, H. A., Rebner and G.A. Scheele (eds.) *The pancreas: biology, pathobiology and disease*, 2nd ed., 871-897., Raven, New York, (1993).
39. Olive K. P. and Tuveson, D. A. *Clin. Cancer Res.* **2006**, *12*, 5277.
40. Voskoglou-Nomikos, T.; Pater, J. L. and Seymour, L. *Clin. Cancer Res.* **2003**, *9*, 4227.
41. Guzman, J.; Iglesias, M. T.; Compan, V.; Andrio, A. *Polymer* **1997**, *38* (20), 5227-5232.

## CHAPTER 5 ENVIRONMENT-SENSITIVE DRUG RELEASE FROM PRINT NANOPARTICLES

### 5.1 Introduction

As discussed in Chapters 2, 3, and 4 the basic PRINT hydrogel nanoparticle formulation has been vastly improved for both passive and active targeting of diseased tissue. Optimization of the NP surface chemistry with either inert poly (ethylene glycol) or active Z<sup>EGFR</sup> targeting affibody has enhanced the carrier's *in vivo* behavior.<sup>1</sup> Furthermore, a reduction in NP size improved tumor deposition immensely in a number of murine disease models and preferential accumulation was observed at the target cancer site. With these improvements in the carrier and identification of disease models most appropriate for a nanoparticle therapy, our current endeavors focus on the incorporation of a potent chemotherapeutic into the particle matrix. In this work, incorporation of gemcitabine pro-drugs for site-specific release in the tumor bed is the main emphasis.

Pro-drug techniques are utilized throughout literature as an effective way to deliver toxic payload specifically to the target site while bypassing healthy tissue. In some cases, “pro-drug” indicates the API must be activated by a chemical, enzymatic, or biological mechanism *in vivo* prior to evoking a toxic effect, as in the case of gemcitabine. Gemcitabine must first influx into the cell by means of nucleoside transporters and intracellularly convert to diphosphate and triphosphate analogues that are responsible for its cytotoxicity.<sup>18</sup> In the case of quercetin, a potent tyrosine kinase inhibitor, no oral bioavailability was expressed and was therefore altered with a carboxyl-functionality to enhance solubility upon IV-administration. After IV-treatment,

the pro-drug hydrolyzed and converted back into its active analogue.<sup>19</sup> As indicated, pro-drug formulations have been utilized to overcome issues with drug activity and delivery, as well as, several other issues in therapeutic administration.<sup>20,21</sup>

In the case of nanoparticulate delivery, pro-drug formulations can be utilized as a way to complex or covalently bind the API to the carrier. In some instances, the API can be complexed into a polymeric backbone and subsequently assembled into a micelle, as well, direct encapsulation and surface complexation of the drug are common.<sup>22-25</sup> These methods often require external stimuli, such as near-IR light, or internal stimuli, such as innate salt content in plasma, to convert Pt (IV) to cytotoxic Pt (II) complexes.<sup>24,25</sup> These stimuli-dependent linkages can prove to be advantageous when trying to limit off-target sequestration of the toxic payload. As well, these linkages can promote drug release specifically at the desired disease site.

In the laboratories of Dr. Joseph M. DeSimone, a number of pro-drug PRINT systems have been developed that incorporate potent therapeutics.<sup>2-8</sup> In one account, docetaxel was successfully encapsulated within a PLGA carrier and upon administration *in vivo* improved plasma pharmacokinetics, drug biodistribution, and tumor regression was observed.<sup>3</sup> In order to overcome the burst release commonly observed with drug encapsulation into a thermoplastic PLGA matrix, docetaxel was lipidized through a pH-sensitive linkage. In this case, the lipidated pro-drug diffused much slower through the hydrophobic PLGA matrix leading to sustained release at physiological conditions and dramatically improved tumor regression when compared to the free-drug and non-lipidated analogs.<sup>4</sup> Along with drug encapsulation into a PLGA matrix, the DeSimone lab has developed therapeutic systems amenable for direct functionalization into hydrophilic thermoset.

In order to chemically attach a chemotherapeutic throughout an acrylic thermoset, the drug must be modified with a chemical entity amendable to radical polymerization. In the DeSimone lab, a number of common chemotherapeutics have been modified with this acrylate functionality through a pH-sensitive silyl ether linkage and the steric nature of the silanol substituent groups were modified to greatly reduce susceptibility of acidic or basic hydrolysis.<sup>9</sup> With this pH-sensitive linkage, drug release at physiological conditions (pH~7.4) was diminished. Subsequently, if the carrier were administered *in vivo*, it could accumulate in the diseased tissue with the majority of toxic payload still loaded. Once at the target site, the carrier can be internalized within the cell by one of the reported mechanisms of particulate endocytosis and upon reaching the acidic environment of the late-endosome the toxic payload can be released, killing the diseased cell. Deviating from pH-dependent drug release, another site-specific release system was developed in house that utilizes differences in reduction potential within subcellular compartments.

Covalent disulphide linkages are susceptible to thiol- reduction when in the presence of molecules that express free thiol functionality. Glutathione is one such molecule found *in vivo* that expresses a free thiol, furthermore, the molecule is found at exceedingly high concentrations (1-10 mM) in the cytoplasm, as opposed to normal extracellular concentrations of 1-10  $\mu$ M.<sup>10,11</sup> Similar to previously discussed pH-dependent linkage, the DeSimone group capitalized on this concentration disparity and synthesized a model siRNA therapeutic with acrylate functionality through a reversible disulphide linkage.<sup>6,12</sup> With this reducible linkage, a high loading of active therapeutic entrapped within the particle matrix and upon dosage to HeLa cells, significant gene knockdown was observed.<sup>12</sup> Recently, this disulphide linkage has been repurposed for

conjugation with gemcitabine, a common nucleoside metabolic inhibitor, indicated for breast, ovarian, non-small cell lung, and pancreatic cancers.<sup>13,14</sup>

To this aim, we fabricated two 80 nm x 80 nm x 320 nm PRINT particles with either a pH-dependent gemcitabine pro-drug or an intracellular reducing-dependent gemcitabine pro-drug. The total drug-loading and time-dependent release of these nano-carriers via drug dissolution and HPLC analysis revealed vastly different release kinetics between the two linkages. The 80 nm x 80 nm x 320 nm NPs with reducible pro-drug were dosed onto three separate cancer cell-lines revealing potent cytotoxic effect. In future studies, the reducible pro-drug will be tested *in vivo* for therapeutic effect.

## 5.2 Results and Discussion

### 5.2.1 Pro-drug Nanoparticle Fabrication and Characterization

In these studies, two bifunctional environment-dependent linkages were synthesized in house and are discussed in greater detail in previous accounts. In both linkages, one side group is functionalized with a common chemotherapeutic, gemcitabine, and the other an acrylate group for fabrication into the polymeric matrix upon PRINTing (Figure 5.1). The pH- and reduction-dependent pro-drugs (henceforth denoted iPr-GEM and SS-GEM, respectively) were loaded into the pre-particle solution (PPS) at 20 wt % of solids for either fabrication of 80 nm x 80 nm x 320 nm PRINT hydrogels. As a side note, diethyl silyl gemcitabine (Et-GEM) acrylate was also tested for functionalization within hydrogel PRINT NPs at an equivalent weight percent; however, due to rapid drug dissolution while harvesting from PVOH in cold buffer solution (pH 7.4 and 9.0 tested) , the pro-drug was not pursued further. Additionally it should be noted that due to drug-incorporation, the weight percentage of HP<sub>4</sub>A was cut by 20 % in order to maintain 3.5 wt % total solids in the isopropanol PPS (Table 5.1). A decrease in primary monomer and

subsequent reduction in hydrophilic monomer : cross-linker ratio may alter the modulus of these drug-loaded nanoparticles. Overall, fabrication of both nanoparticle sets was successful and the particles exhibited a similar size range, polydispersity, and zeta-potential as previously noted (Table 5.2). Upon SEM imaging, both pro-drug loaded nanoparticle types displayed similar size and shape to previous 80 nm x 80 nm x 320 nm particles that lack pro-drug (Figure 5.2).

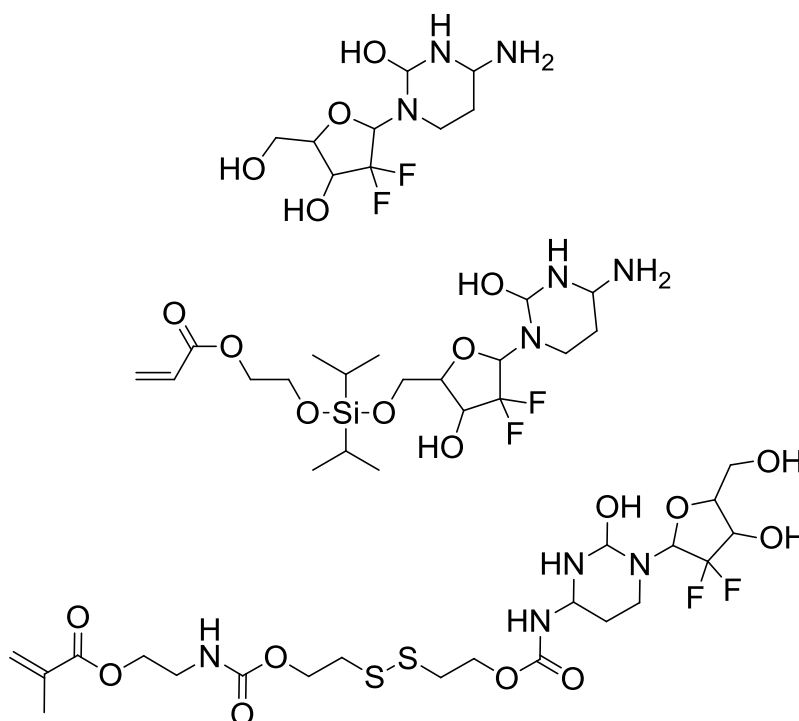


Figure 5.1 Base chemotherapeutic gemcitabine (top) and subsequent derivatives: diisopropyl silyl ether acrylate (iPr-GEM; middle) and reducible disulphide acrylate (SS-GEM; bottom).

Table 5.1 Composition of drug-loaded PRINT NPs

Monomer	Pro-drug NPs	Blank NPs
	Weight %	Weight %
2-aminoethyl methacrylate HCl (AEM)	20	20
PEG <sub>700</sub> diacrylate	10	10
2,4,6 trimethylbenzoyl diphenylphosphine oxide (TPO)	1	1
Isopropyl-GEM or Disulphide-GEM (iPr-GEM or SS-GEM)	20	0
Hydroxy (PEG) <sub>4</sub> acrylate (HP <sub>4</sub> A)	49	69
Total	100	100

Table 5.2 Dynamic light scattering of prodrug-loaded 80 nm x 80 nm x 320 nm NPs

80 x 320 Type	Z-avg (nm)	PdI	ZP (mV)
iPr-GEM	249 ± 4	0.02 ± 0.01	36 ± 5
SS-GEM	274 ± 2	0.11 ± 0.02	35 ± 7

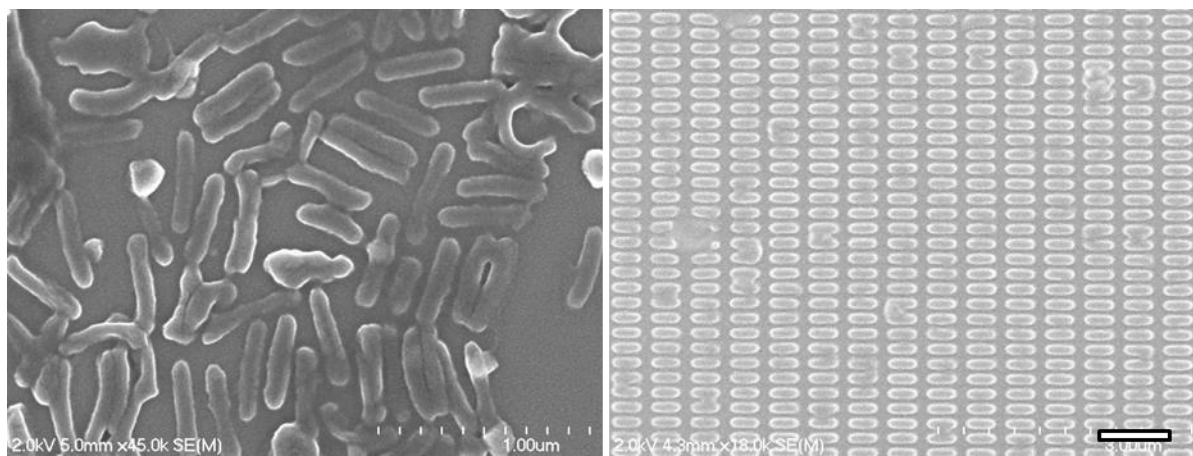


Figure 5.2 Scanning electron microscopic images of harvested iPr-GEM NPs (left) and laminated SS-GEM (right) loaded 80 nm x 80 nm x 320 nm [scale bar on right = 1 μm].

### 5.2.2 Gemcitabine Release from Hydrogel Nanoparticles

In order to quantify total drug-loading and rate of release of the two linkages from the PRINT hydrogels, drug dissolution and HPLC analysis was conducted. A loading of active gemcitabine was observed at approximately 100 µg and 50 µg of gemcitabine per mg of NP for iPr-GEM and SS-GEM, respectively. Based upon this, the loading efficiency

(  $\frac{\text{Experimental Mass GEM via HPLC of Total Drug Release}}{\text{Hypothetical Charge Mass GEM via PPS}}$  ) was calculated at approximately 90% and 50%

for the iPr-GEM and SS-GEM, respectively. In time-dependent release studies for iPr-GEM loaded NPs, drug release was minimal at physiological conditions (pH 7.4) with less than 20% over five days. In the same time interval, in conditions representative of the subcellular late endosome (pH 5.0), sustained drug release of up to 80% was observed (Figure 5.3). Expanding on these results, it is of interest to note that due to poor lymphatic drainage and tissue oxygenation in the tumor bed, cancerous tissue is often acidic in nature (pH < 7).<sup>15,16</sup> In the case of iPr-GEM loaded NPs, passive targeting to the tumor site may elicit drug release and upon endocytosis, sustained cell-specific drug delivery can be obtained. In the case of SS-GEM, no detectable drug release was observed at extracellular reducing conditions (1 µM GSH); yet, burst release was observed at cytoplasmic conditions (5 mM GSH) with over 50% in the first eight hours and a sustained release of 70% over the next five days (Figure 5.4).



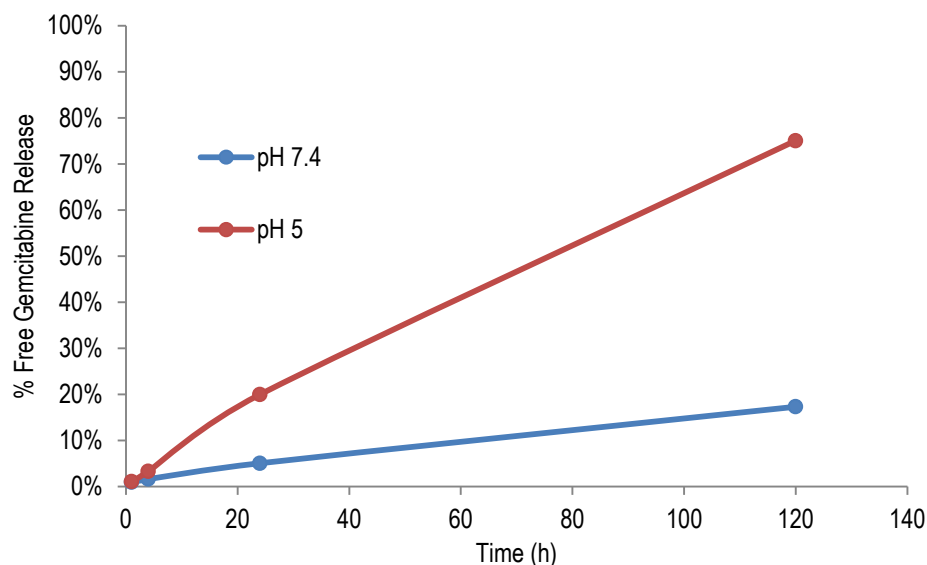


Figure 5.3 Release of free gemcitabine from iPr-GEM loaded 80 x 320 nm NPs upon dissolution as quantified by HPLC (time points: 0, 1, 4, 24, 48, and 120 hours).

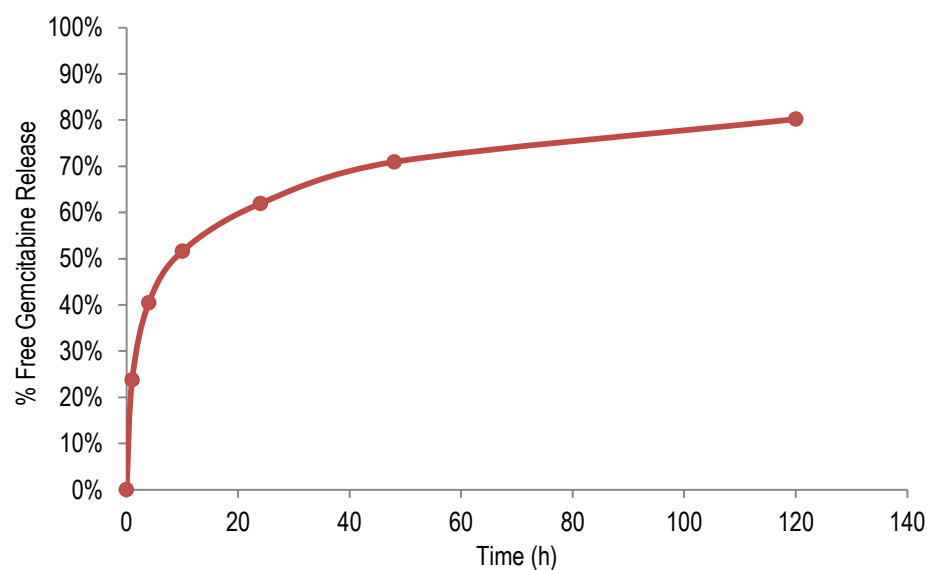


Figure 5.4 Release of free gemcitabine from SS-GEM loaded 80 x 320 nm NPs upon dissolution in 5 mM glutathione as quantified by HPLC (time points: 0, 1, 4, 24, 48, and 120 hours).

### 5.2.3 Cytotoxicity of Gemcitabine-Loaded PRINT NPs

The cytotoxicity of SS-GEM drug-loaded 80nm x 80 nm x 320 nm NPs was tested and dosed onto three different cancer cell-lines: 344SQ (mouse non-small cell carcinoma), GFP-expressing A549 (human non-small cell lung carcinoma), and A431 (human epidermoid carcinoma). Important to note that the iPr-GEM was not tested for cytotoxicity and future studies

were tabled due to the inability to surface modify NPs for *in vivo* function (PEGylation and acetylation) without losing the majority of drug in reaction and wash solutions. However, SS-GEM loaded NPs exhibited drug retention during modification and deemed suitable for *in vitro* testing. In previously denoted cell-lines, free gemcitabine exhibited half maximal inhibitory concentrations (IC<sub>50</sub>) at approximately 4 nM and free SS-GEM exhibited an IC<sub>50</sub> between 15-100 nM (Table 5.3). The diminished cytotoxicity of the pro-drug is likely due to necessary disulphide reduction and subsequent conversion to active gemcitabine prior to expressing an apoptotic effect. To this end, the SS-GEM loaded NPs exhibited significantly lower toxicity towards all cancer cell-lines. The reduced NP toxicity is most likely due to necessary cellular endocytosis, drug conversion, and diffusion prior to gemcitabine exhibiting an apoptotic effect.

Table 5.3 IC<sub>50</sub> values of Gemcitabine in Three Cancer Cell-lines

Drug Form	344SQ	GFP-A549	A431
Free Gemcitabine	4	3	4
Pro-drug Gemcitabine	60	15	100
Pro-Drug Loaded 80 nm x 80 nm 320 nm	500	125	ND*

\*IC<sub>50</sub> not detected

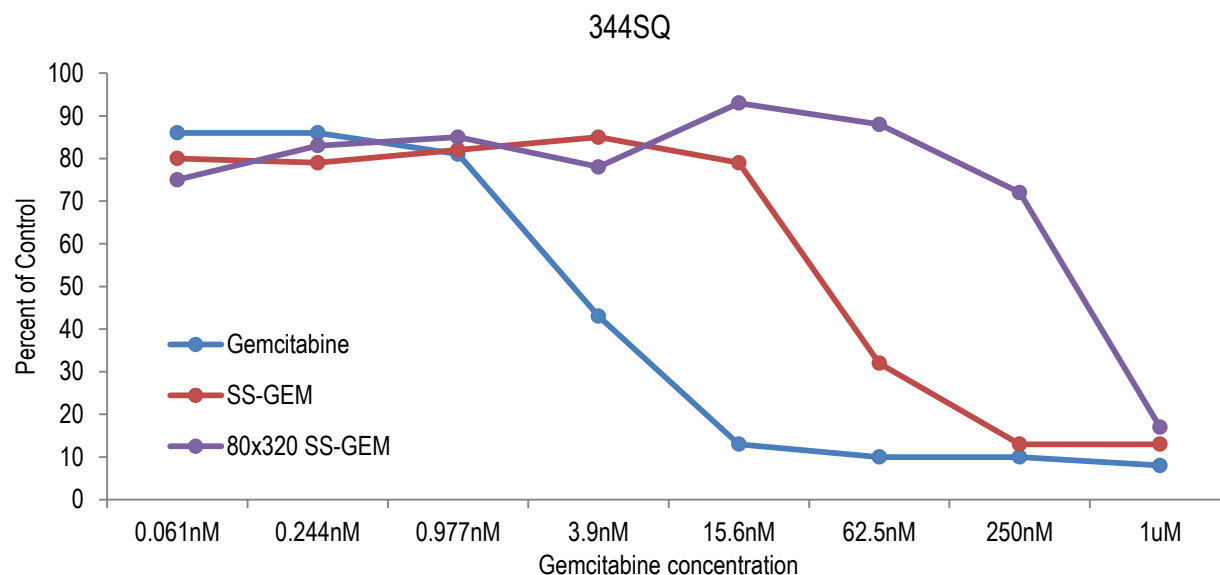


Figure 5.5 Cytotoxicity of SS-GEM loaded 80 x 320 nm NPs dosed onto 344SQ (mouse non-small cell lung carcinoma) cells with approximate  $IC_{50}$  values of 4, 60, and 500 nM for the free-gemcitabine, SS-GEM pro-drug, and SS-GEM loaded NPs, respectively.

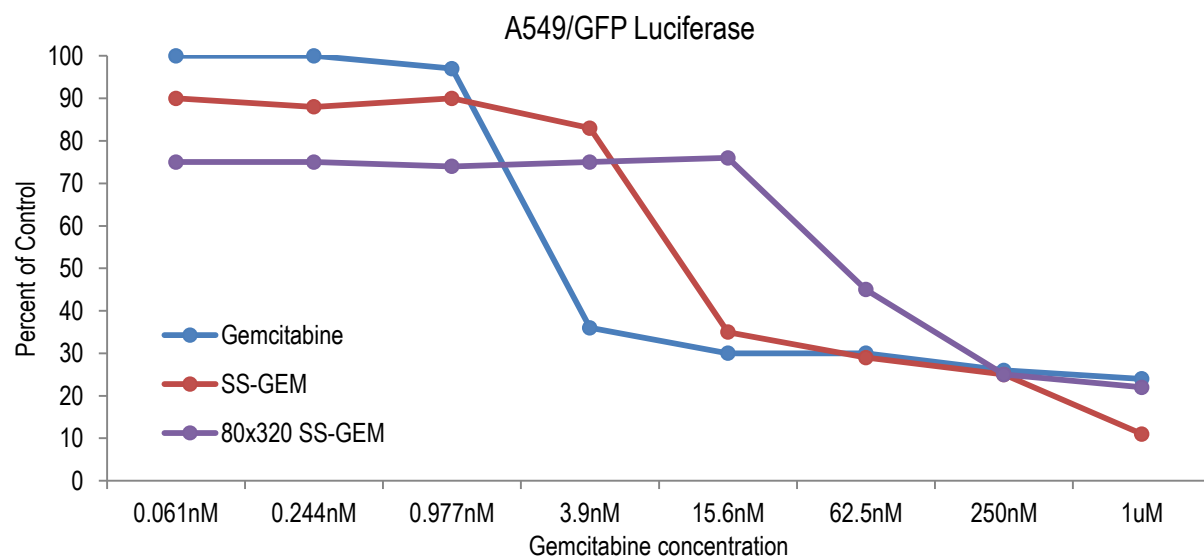


Figure 5.6 Cytotoxicity of SS-GEM loaded 80 x 320 nm NPs dosed onto A549 (GFP-expressing human non-small cell lung carcinoma) cells with approximate  $IC_{50}$  values of 3, 15, and 125 nM for the free-gemcitabine, SS-GEM pro-drug, and SS-GEM loaded NPs, respectively.

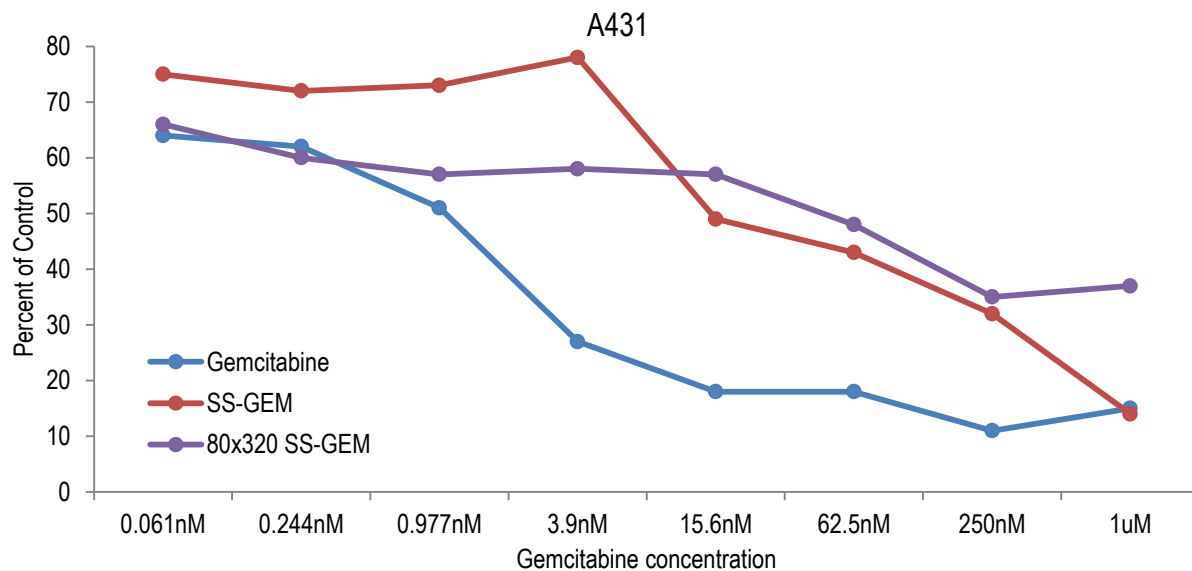


Figure 5.7 Cytotoxicity of SS-GEM loaded 80 x 320 nm NPs dosed onto A431 (human epidermoid carcinoma) cells with approximate  $IC_{50}$  values of 4 and 100 nM for the free-gemcitabine and SS-GEM pro-drug, respectively. No  $IC_{50}$  for drug loaded NPs was quantified.

### 5.3 Materials and Methods

#### 5.3.1 Materials

2-aminoethyl methacrylate hydrochloride (AEM), reduced glutathione (GSH), dithiothreitol (DTT), diphenyl (2,4,6-trimethylbenzoyl) phosphine oxide (TPO), poly (ethylene glycol) diacrylate ( $M_n$  700) (PEG<sub>700</sub>DA), trypsin, ethylenediaminetetraacetic acid (EDTA), and sucrose were obtained from Sigma-Aldrich. Thermo Scientific HyClone fetal bovine serum (FBS), isopropanol, sterile water, dimethylformamide (DMF), Dulbecco's phosphate buffered saline (pH 7.4), 1X phosphate buffered saline (PBS), sodium hydroxide potassium acid phthalate buffer (pH 5.0), and Dulbecco's Modified Eagle's Medium (DMEM) were purchased from Fisher Scientific. Polyvinyl alcohol ( $M_w$  2000) (PVOH) was bought from Acros Organics. Human epidermoid carcinoma (A431) cells were purchased from American Type Culture Collection. Murine lung adenocarcinoma (344 SQ) cells were graciously provided by the laboratories of Dr. Chad Pecot. GFP-expressing human non-small cell lung carcinoma (A549) cells were kindly provided by the UNC Animal Core. 80 nm x 80 nm x 320 nm PRINT molds were acquired from

Liquidia Technologies. As described in previous accounts, tetraethylene glycol monoacrylate (HP<sub>4</sub>A) was synthesized in-house.<sup>17</sup>

### 5.3.2 Pro-drug Incorporation and Particle Characterization

The pro-drug loaded 80 nm x 80 nm x 320 nm were fabricated with similar methods as indicated in section 4.4.2 with a few minor changes. The SS-GEM and iPr-GEM pro-drugs were dissolved in DMF (40 – 100 mg /mL) prior to addition into the pre-particle solution. Upon drawing the polymeric film on the R2R, the heat gun temperature was increased in order to evaporate poorly volatile DMF prior to mold lamination. All other procedures, such as lamination to PVOH, were kept the same.

In effort to reduce premature gemcitabine release when harvesting and purifying iPr-GEM loaded NPs, a number of procedures were put into place to diminish premature drug release. First, the harvesting solution (pH 7.4) was kept at 4°C. In addition, the NP solution was purified by centrifugation methods utilizing chilled pH 7.4 buffer. As well, complete characterization by TGA and DLS was completed as quickly as possible. As will be described in greater detail in section 5.3.3, both total and time-dependent drug release was initiated immediately upon concentration assessment by TGA.

### 5.3.3 Drug Release and HPLC Quantification

Total drug release and time-dependent drug release studies were assessed by simple drug dissolution methods. Total drug release of iPr-GEM NPs was assessed by first resuspending NPs at 1 mg / mL (200 µL) in pH 2.0 buffer and incubating in a 1.5 mL Eppendorf for 24 hours at 37 °C on a shaker plate (Eppendorf, 1400 rpm). At the time point, an aliquot of the particle solution (80 µL) was removed from the incubating solution, placed into another Eppendorf tube, and centrifuged (Eppendorf 5417C, 14000 rpm) for 30 minutes. The supernatant (60 µL),

containing the released gemcitabine, was put into another Eppendorf and placed directly into storage at -20°C. Total drug release of SS-GEM loaded NPs was assessed utilizing the exact same methods except the particles were initially resuspended in a reducing solution of DTT (100 mM). Time-dependent drug release of iPr-GEM loaded NPs was assessed by first resuspending NPs at 1 mg / mL (1 mL) in either pH 5.0 or pH 7.4 buffer. The dissolution procedure was identical to total drug release studies except multiple time points were collected at 1, 4, 8, 24, 48, and 120 hours. The time-dependent drug release of SS-GEM loaded NPs was identical that of iPr-GEM except the NPs were initially resuspended in a 5 mM glutathione solution.

In order to quantify the mass of gemcitabine released in total and over time, HPLC analysis was utilized. HPLC was run on an Agilent 1200 series HPLC system. The mobile phase consisted of mixtures of H<sub>2</sub>O + 0.1% TFA (solvent A) and acetonitrile + 0.1% TFA (solvent B). The elution protocol for released gemcitabine consisted of a gradient starting at 100:0 (A to B) and finishing at 97.5:2.5 (A to B) over 10 minutes. The analyte was eluted at a flow rate of 1 mL / min and monitored at a wavelength of 267 nm. The peak for gemcitabine eluted at approximately 8 minutes. In order to quantify drug release, a standard curve was created from a 0.5 mg / mL gemcitabine·HCl water solution with 10 standard dilutions (Figure A.1-A.4).

#### 5.3.4 Cytotoxicity Studies

Cells were seeded in 200 µL of media [RMPI 1640 Medium supplemented with 10% FBS] at a density of 5000 cells /cm<sup>2</sup> into a 96-well micro-titer plate. Cells were allowed to adhere for 24 h and then incubated with SS-GEM NPs, free gemcitabine, or free SS-GEM prodrug at concentrations ranging from 1,000 µg/mL to 0.061 ng/mL for 72 h at 37 °C in a humidified 5% CO<sub>2</sub> atmosphere. After the incubation period, all medium/particles were aspirated off cells. 100 µL fresh medium was added back to cells followed by addition of 100 µL Cell Titer-Glo®

Luminescent S8 Cell Viability Assay reagent. Plates were placed on a microplate shaker for 2 min and incubated at room temperature for 10 minutes to stabilize luminescent signal. The luminescent signal was then recorded (Molecular Dynamics SpectraMax M5 plate reader) and the viability of the cells were expressed as a percentage of the viability of cells grown in the absence of particles.

#### 5.4 Conclusions

Significant work has been conducted into the optimization of PRINT hydrogels for tumoritropic delivery. With the optimal particle, it was of great interest to load a potent and commonly used chemotherapeutic, gemcitabine, into the polymeric matrix through environmental-dependent linkages. In this account two linkages were studied (1) a reversible disulphide linkage dependent on cytosolic reducing conditions for cleavage and (2) a pH-dependent silyl ether linkage dependent on acidic late-endosome conditions for cleavage. In drug dissolution, immediate burst release of the SS-GEM loaded NPs was observed when in cytoplasmic reducing conditions, yet, negligible release was observed in extracellular reducing conditions. The iPr-GEM linkage displayed a sustained release profile over the course of 5 days with minimal release in physiological conditions. In cytotoxicity studies, encouraging toxicity was observed for SS-GEM loaded NPs against A549 human NSCLC. In future experiments, SS-GEM loaded NPs will be tested in human A549 xenograft and orthotopic mouse models.

## 5.5 References

1. Perry, J. L. and Reuter, K. G.; Kai, M. P.; Herlihy, K. P.; Jones, S. W.; Luft, J. L.; Napier, M.; Bear, J. E. and DeSimone, J. M. *Nano Lett.* **2012**, *12* (10), 5304-5310.
2. Chu, K. S.; Hasan, W.; Rawal, S.; Walsh, M. D.; Enlow, E. M.; Luft, J. C.; Bridges, A. S.; Kuijer, J. L.; Napier, M. E.; Zamboni, W. C. and DeSimone, J. M. *Nanomed-Nanotechnol.* **2013**, *9* (5), 686-693.
3. Chu, K. S.; Schorzman, A. N.; Finniss, M. C.; Bowerman, C. J.; Peng, L.; Luft, J. C.; Madden, A. J.; Wang, A. Z.; Zamboni, W. C. and DeSimone, J. M. *Biomat.* **2013**, *34* (33), 8424-8429.
4. Chu, K. S.; Finniss, M. C.; Schorzman, A. N.; Kuijer, J. L.; Luft, J. C.; Bowerman, C. J.; Napier, M. E.; Haroon, Z. A.; Zamboni, W. C. and DeSimone, J. M. *Nano Lett.* **2014**, *14* (3), 1472-1476.
5. Parrott, M. C.; Finniss, M.; Luft, J. C.; Pandya, A.; Gullapalli, A.; Napier, M. E. and DeSimone, J. M. *J. Am. Chem. Soc.* **2012**, *134* (18), 7978-7982.
6. Dunn, S. S.; Tian, S.; Blake, S.; Wang, J.; Galloway, A. L.; Murphy, A.; Pohlhaus, P. D.; Rolland, J. P.; Napier, M. E. and DeSimone, J. M. *J. Am. Chem. Soc.* **2012**, *134* (17), 7423-7430.
7. Hasan, W.; Chu, K.; Gullapalli, A.; Dunn, S. S.; Enlow, E.; Luft, J. C.; Tian, S.; Napier, M.E.; Pohlhaus, P. D.; Rolland, J. P. and DeSimone, J. M. *Nano Lett.* **2012**, *12*, 287-292.
8. Enlow, E. M.; Luft, J. C.; Napier, M. E. and DeSimone, J. M. *Nano Letters*, **2011**, *11* (2), 808-813.
9. Parrott, M. C.; Luft, J. C.; Byrne, J. D.; Fain, J. H.; Napier, M. E. and DeSimone, J. M. *J. Am. Chem. Soc.* **2010**, *132* (50), 17928-17932.
10. Griffith, O. W. and Meister, A. *PNAS* **1985**, *82* (14), 4668-4672.
11. Tietze, F. *Anal. Biochem.* **1969**, *27*, 502-522.
12. Xu, J.; Wang, J.; Luft, J. C.; Tian, S.; Owens, G.; Pandya, A.; Berglund, P.; Pohlhaus, P. D.; Maynor, B. W.; Napier, M. E. and DeSimone, J. M. *J. Am. Chem. Soc.* **2012**, *134*, 8774-8777.
13. Hui, J. F. and Reitz, J. *Am. J. Health-Syst Ph.* **1997**, *54* (2), 162-170.



14. Scagliotti, G. V.; Parikh, P.; Pawel, J.; Biesma, B.; Vansteenkiste, J.; Manegold, C.; Serwatowski, P.; Gatzemeier, U.; Digumarti, R.; Zukin, M.; Lee, J. S.; Mellemgaard, A.; Park, K.; Patil, S.; Rolski, J.; Goksel, T.; Marinis, F.; Simms, L.; Sugarman, K. P. and Gandara, D. *Am. Soc. Clin. Oncol.* **2008**, 26 (21), 3543-3551.
15. Wike-Hooley, J. L.; Haveman, J. and Reinhold, H. S. *Radiotherap. Oncol.* **1984**, 2, 343-346.
16. Gerweck, L. E. and Seetharaman, K. *Cancer Res.* **1996**, 56, 1194-1198.
17. Guzman, J.; Iglesias, M. T.; Compan, V.; Andrio, A. *Polymer* **1997**, 38 (20), 5227-5232.
18. Mini, E.; Nobili, S.; Caciagli, B.; Landini, I.; and Mazzei, T. *Ann. Oncol.* **2006**, 5, 7-12.
19. Mulholland, P. J.; Ferry, D. R.; Anderson, D.; Hussain, S. A.; Young, A. M.; Cook, J. E.; Hodgkin, E.; Seymour, L. W. and Kerr, D. J. *Ann. Oncol.* **2001**, 12, 245-248.
20. Chen, Q.; Espey, M. G.; Krishna, M. C.; Mitchell, J. B.; Corpe, C. P.; Buettner, G. R.; Schacter, E. and Levine, M. *PNAS* **2005**, 102 (38), 13604-13609.
21. Ferguson, M. J.; Ahmed, F. Y and Cassidy, J. *Drug Resist. Update* **2001**, 4, 225-232.
22. Xiao, H.; Qi, R.; Liu, S.; Hu, X.; Duan, T.; Zheng, Y.; Huang, Y. and Jing, X. *Biomater.* **2011**, 32 (30), 7732-7739.
23. Dhar, S.; Gu, F. X.; Langer, R.; Farokhzad, O. C. and Lippard, S. J. *PNAS* **2008**, 105 (45), 17356-17361.
24. Dai, Y.; Xiao, H.; Liu, J.; Yuan, Q.; Ma, P.; Yang, D.; Li, C.; Cheng, Z.; Hou, Z.; Yang, P. and Lin, J. **2013**, 135, 18920-18928.
25. Jeong, Y.; Kim, S.; Jin, S.; Ryu, H.; Jin, Y.; Jung, T.; Kim, I. and Jung, S. **2010**, 97(3), 1268-1276.

## CHAPTER 6 FUTURE WORK AND SUMMARY

### 6.1 Hydrogel PRINT Nanoparticles for the Treatment of Cancer

As demonstrated in this work, nanoparticle surface modification, alterations in NP size, and variations in disease model can have dramatic effects on particle-blood interactions and subsequent *in vivo* biodistribution. Designing PRINT NPs with a dense PEG layer is paramount for enhancing macrophage resistance, inhibiting protein binding, and extending retention in the blood compartment.<sup>1</sup> Interestingly, PRINT NPs require significantly lower PEG coverage upon comparison to other nanoparticles throughout literature. Most likely, the hydrophilic nature of the hydrogel promotes biocompatibility and helps avoiding immune recognition. When actively targeting PEGylated PRINT NPs, optimizing ligand surface density is vital. With increasing ligand coverage, NP internalization in target and off-target cells increased dramatically *in vitro*; as well, upon IV-administration, blood retention quickly diminished and particle accumulation into an EGFR-overexpressing flank tumor increased. However, it was beyond question that the determinant factor promoting tumor deposition was nanoparticle size, as the 55 nm x 60 nm NP outperformed all types (targeted 80 x 320, non-targeted 80 x 320, and targeted 55 x 60 nm). Even with superior tumor deposition of the non-targeted 55 x 60 nm NP, it is premature to suggest that this will without a doubt translate to greater efficacy as targeting may enhance *in vivo* cancer cell uptake, subsequently, improving efficacy. Even with these optimizations in PRINT NPs, nanoparticles should only be utilized in treating cancers prone to macromolecular accumulation as the degree of EPR effect varies immensely from one cancer type to another.

Exhaustive evaluation of disease models prone to NP accumulation may translate to more immediate therapeutic benefit. In our studies, NP tumor accumulation varied dramatically between different murine cancer models. A murine non-small cell lung isograft, 344SQ, displayed superior particle sequestration over all other flank cancer cell-types and orthotopic disease models of metastatic NSCLC revealed preferential particle accumulation in diseased tissue. With the optimized carrier and model, ongoing studies encompass the incorporation of gemcitabine pro-drugs into the particle matrix and how environmental stimuli can be used to release the toxic cargo. As current studies progress, obstacles will arise, some of these can be predicted and others not. Potentially, the most foreboding challenge may arise from the same poly (ethylene glycol) coating that has led to such remarkable tumor accumulation.

## 6.2 The PEGylation Paradox

Optimizing the PEGylation density has led to unprecedented sequestration of PRINT NPs inside murine tumors and yet it is currently unknown whether this will prove beneficial in the realm of drug delivery. The reasoning behind the uncertainty lies within the superior resistance of PEGylated particles to be internalized in non-phagocytic cell-lines, as would be cancer cells. With the current pro-drugs being assessed, both require NPs to be internalized within a cell for drug release, whether in the cytosol or late endosome. While some drug release may occur in the slightly acidic extracellular tumor environment, the degree of release *in vivo* is not currently known. In order to counter this potential issue, alternative methods of drug delivery once at the tumor site should be devised in case of therapeutic failure.

Alternatives to poly (ethylene glycol) coatings or adaptations of it may prove beneficial. A number of alternative surface coatings to PEG have been created, such as poly (vinyl alcohol),

poly-N-vinylpyrrolidone, and poly (amino acid) s.<sup>2-5</sup> These alternative coatings display similar characteristics of PEG in reducing RES recognition and extending blood circulation.<sup>2</sup> As well, PEG substitutes may become a necessity as PEG-specific IgM antibodies have been observed after initial dosage of stealth liposomes, leading to substantially reduced circulation half-life in follow-up IV-administrations.<sup>6,7</sup> However, in most cases, alternative coatings still require covalent attachment; therefore, this may not overcome issue related to particulate cell internalization once at the tumor site. Adsorption of PEG to the surface of the particle may be useful over covalent attachment as the coating can shed over time, leaving a positive surface charge on the NP, and promoting cellular internalization which has been observed in previous studies.<sup>8</sup> However, non-covalent interactions of a PEG surface coating may result in stability and storage issues prior to particle injection. Dr. Leaf Huang, a key designer of the PEGylated liposome, has described that a covalently attached sheddable-PEG coating may prove invaluable in facilitating successful drug delivery to tumor cells.<sup>6</sup> The sheddable-coating may be possible through the use of PEG-NP linkages that, like the pro-drugs linkages previously discussed, can be environmentally dependent. To this effect, several linkages have already been developed that may yield successful release of the PEG coating upon accumulation in the tumor bed.

The development of pH-sensitive linkages that rapidly release PEG at slightly acidic conditions is of utmost importance for effective drug delivery within cancer cells (Figure 6.1).<sup>2</sup>  $\beta$ -thiopropionate linkages have proven to be extremely sensitive to changes in pH with reported degradations of up to 97% at pH 5.5 and no observable cleavage at physiological conditions (37°C; pH ~7.4) after 24 hours.<sup>2,9</sup> Perhaps the most commonly used acid-sensitive linker utilizes hydrazone chemistry. In one account utilizing a DNA/polycation polyplexes, no-deshielding of PEG from the NP was observed after 4h at physiological conditions with complete deshielding at

1h at pH 5.<sup>2,10</sup> The most promising may be diorthoester chemistry, as it one of the most studied linkages and very mild reductions in pH (tumor microenvironment) promote rapid hydrolysis and PEG shedding.<sup>2,6,11-13</sup>

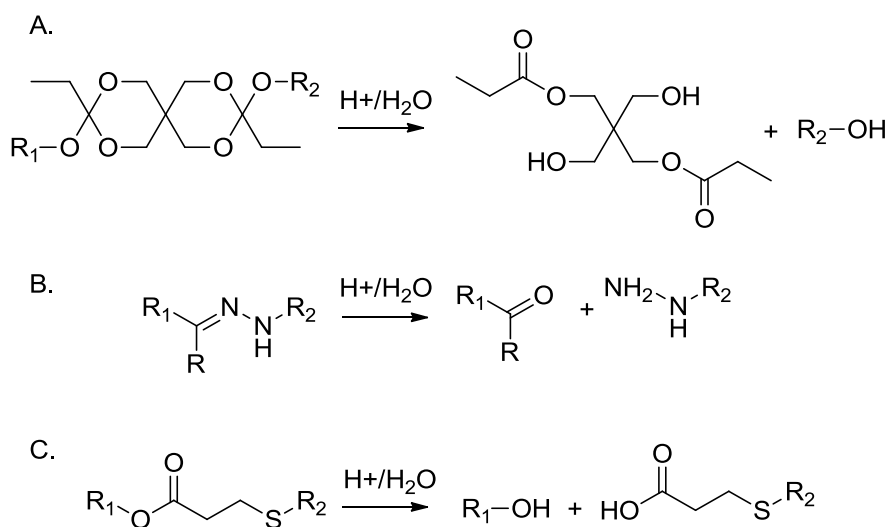


Figure 6.1 Diorthoester (A), hydrazone (B), and  $\beta$ -thiopropionate (C) pH-sensitive linkages commonly used with sheddable PEG and subsequent hydrolysis reactions ( $R_1$  = PEG,  $R_2$  = NP).<sup>2</sup>

Even with this potential issue and others may come along, the delivery of PRINT nanoparticles to cancerous tissue continues to be an exciting and fruitful endeavor. The use of PRINT technology allows for such fine control over particle design parameters that we have been able to improve tumor accumulation from less than 1% in the year 2010 to upwards of 50% in 2015. In general, these accomplishments were made possible through the advancement of the particle surface characteristics and size, as well, the study of what animal models are best fit for particulate therapy. Needless to say, the future of PRINT in the field of cancer treatment is very promising.

## 6.3 Summary

### 6.3.1 PEGylated PRINT Nanoparticles: The Impact of PEG Density on Protein Binding, Macrophage Association, Biodistribution, and Pharmacokinetics

The impacts of NP surface modification with poly (ethylene glycol): extending NP blood circulation, inhibiting protein binding to the carrier, and diminishing overall RES recognition is well known.<sup>14</sup> However, the degree of PEGylation on a particulate surface, or PEGylation density, to successfully promote these *in vivo* benefits is more elusive. In literature, complications arise due to differences in the carrier and major differences in validation and because of this, questions remain to be answered. What is the standard manner in which PEG density should be reported (PEG/nm<sup>2</sup>, PEG/NP, mol PEG / mass NP, etc.)? What is the optimal PEG coverage to promote benefits *in vivo*? Is this PEG density dependent on the characteristics of the carrier? What is the proper method to quantify PEGylation density? These questions remain unanswered, for the most part, because there are few ways to accurately quantify PEG density.

In Chapter 2, we attempted to address this issue by developing a method to assess PEG density via standard plate-reader analysis of a fluorescently-tagged PEG. The PEGylation density on the surface of hydrogel PRINT nanoparticles was varied and the effects on protein adsorption, macrophage uptake, and circulation time were observed. Interestingly, the density of PEGylation necessary to promote a long-circulating particle was dramatically less than what has been previously reported. Overall, the methodology provides a rapid screening technique to predict particle behavior *in vivo* and our results deliver further insight to what PEG density is necessary to facilitate long-circulation.

### 6.3.2 Targeted PRINT Hydrogels: The Role of Nanoparticle Size and Ligand Density on Cell Association, Biodistribution, and Tumor Accumulation

Functionalizing nanoparticles with biological entities that bind to over-expressed receptors on cancerous cells, termed active targeting, is a major endeavor in the field. Active targeting continues to be a hotly studied area due to the potential to preferentially target cancer cells over healthy tissue leading to several benefits: improving drug delivery, reducing off-target toxicity, and increasing the overall therapeutic index of an API.<sup>15</sup> However recently, undesired consequences of targeting a carrier have begun to arise due to “over-targeting” a carrier; examples include unanticipated toxicity of a seemingly non-toxic carrier, alterations in PK/PD, and enhanced immunogenicity.<sup>15,16</sup> Similar to issues addressed in Chapter 2, it was of interest to study how ligand density changed the behavior in cell culture and *in vivo*.

In Chapter 3, we addressed these issues by fabricating two hydrogel particle types (80 nm x 80 nm x 320 nm and 55 nm x 60 nm) with varying amounts of EGFR binding affibody ( $Z^{\text{EGFR}}$ ) conjugated through a PEG<sub>5k</sub>-linker. The density of ligand density was varied on both NP types and effects on cell uptake, biodistribution, and tumor accumulation were observed. *In vitro* studies revealed direct dependence of cell membrane association and cellular internalization as a function of targeting ligand density, nanoparticle dosage, and time. *In vivo* studies displayed a notable inverse relationship between circulation time and ligand density, yet, a direct correlation was observed for tumor accumulation. Overall, targeting ligand density and NP size were shown to have major impacts on *in vivo* outcomes.

### 6.3.3 Mediating Passive Accumulation with PRINT Nanoparticles: The Effect of Particle Size and Tumor Model

The therapeutic benefit of nanoparticles as drug carriers against cancer has, to this point, been of moderate success.<sup>17</sup> Some researchers indicate that the lack of impact stems from natural

lags between academic success and clinical translation, specifically noting antibody drug conjugates (ADCs) and the large time interval between its foundation in the 1970's and its current massive success in the year 2015.<sup>18</sup> Without a doubt, this is a fair and reasonable view. Academic discoveries need time to mature, pass through the minds and hands of researchers, and have points of controversy and discussion before they can translate to something as complex as treating human disease. However, a number of issues currently exist in the field of nanoparticulate cancer therapeutics that hinder clinical achievements: (1) improper assessment of efficacy in disease models (ex. insufficient data collection in tumor regression/survival studies), (2) use of disease models that fail to translate to humans (ex. subcutaneous xenograft mouse models, while low in cost and beneficial in a complementary role, are alone insufficient when assessing potential clinical success), and (3) large batch-to-batch variance of the carrier (ex. changes in drug loading, size, stability). Along with these issues, the field has not truly identified the types of cancer most benefited by particle therapy. With these issues in mind, we attempted to identify cancer cell-lines that may be the most impacted by the use of nanoparticle therapies.

In Chapter 4, we manufactured three different particle types: 80 nm x 80 nm x 320 nm, 80 nm x 80 nm x 180 nm, and 55 x 60 nm surface-modified poly(ethylene glycol) and examined how NP size, tumor cell-line, and tumor location affect particle deposition in cancerous tissue. *In vivo* studies revealed that particle size had no effect on blood pharmacokinetic behavior, association with cancerous cells, or macrophage resistance. In four different flank tumor mouse models, particulate accumulation varied drastically between the different NP types and models. Additionally, IHC staining of the four flank models revealed major differences in microvessel density, collagen, and tumor-associated macrophage. In orthotopic disease models, 55 nm x 60 nm NPs preferentially deposited in both primary and metastatic sites in comparison to off-target



healthy tissue. While preferential metastatic accumulation is encouraging, assessment of therapeutic effect can only be deemed upon efficacy in clinically relevant disease models.

#### 6.3.4 Environment-Sensitive Drug Release from PRINT Nanoparticles

Passive and active targeting nanoparticulate strategies may yield improved deposition into a solid tumor mass; yet, delivery of an active pharmacological agent is the main goal. While several NP technologies utilize drug encapsulation as the method of drug entrapment, diffusion out of the particle upon administration promotes higher volume of distribution and systemic toxicity.<sup>19,20</sup> In order to account for this, a number of pro-drug strategies have been developed that covalently attach an API to a nanocarrier through a cleavable bond that can be unconjugated with a unique stimulus.<sup>21,22</sup> In the laboratories of DeSimone, two linkages have been developed that cleave under pH (silyl ether) or reducing (reversible disulphide) conditions and were therefore repurposed for chemotherapeutic / nanoparticle attachment.<sup>23,24</sup>

In Chapter 5, two different linkages (1) silyl ether and (2) a reversible disulphide were studied that exhibit bifunctional functionality with gemcitabine, a common nucleoside analogue, and an acrylate group for PRINT NP incorporation. The SS-GEM linker revealed burst release upon reaching conditions similar to cell cytoplasm, an environment reducing in nature, and negligible release in extracellular reducing conditions. The iPr-GEM displayed sustained release at acidic conditions, similar to subcellular conditions in the late endosome, and slow release in physiological conditions. The advancements made in particle surface characteristics, NP size, and tumor model optimization will be combined with these endeavors in pro-drug incorporation in effort to test for therapeutic efficacy.

## 6.4 References

1. Perry, J. L. and Reuter, K. G.; Kai, M. P.; Herlihy, K. P.; Jones, S. W.; Luft, J. L.; Napier, M.; Bear, J. E. and DeSimone, J. M. *Nano Lett.* **2012**, *12* (10), 5304-5310.
2. Romberg, B.; Hennink, W. E. and Storm, G. *Pharm. Res.* **2008**, *25* (1), 55-71.
3. Takeuchi, H.; Kojima, H.; Yamamoto, H. and Kawashima, Y. *J. Control. Release* **2001**, *75*, 83-91.
4. Torchilin, V. P.; Shtilman, M. I.; Trubetskoy, V. S.; Whiteman, K. and Milstein, A. M. *Biochim. Biophys. Acta.* **1994**, *1195*, 181-184.
5. Metselaar, J. M.; Bruin, P.; de Boer, L. W.; de Vringer, T.; Snel, C.; Oussoren, C.; Wauben, M. H.; Crommelin, D. J.; Storm, G. and Hennink W. E. *Bioconjug. Chem.* **2003**, *14*, 1156-1164.
6. Huang, L. and Li, S. *J. Control. Release* **2010**, *145* (3), 178-181.
7. Tagami, T.; Nakamura, K.; Shimizu, T.; Yamazaki, N.; Ishida, T. and Kiwada, H. *J. Control. Release* **2010**, *142*, 160-166.
8. Gratton, S.E.A., Ropp, P. A.; Pohlhaus, P. D.; Luft, J. C.; Madden, V. J.; Napier, M. E. and DeSimone, J. M. *PNAS*, **2008**, *105* (33), 11613-11618.
9. Oishi, M.; Sasaki, S.; Nagasaki, Y. and Kataoka, K. *Biomacromolecules* **2003**, *4*, 1426-1432.
10. Walker, G. F.; Fella, C.; Pelisek, J.; Fahrmeir, J.; Boeckle, S.; Ogris, M. and Wagner, E. **2005**, *11* (3), 418-425.
11. Guo, X. and Szoka, F. C. *Bioconjugate Chem.* **2001**, *12* (2), 291-300.
12. Li, W.; Huang, Z.; Mackay, A.; Grube, S. and Szoka, F. C. *J. Gene. Med.* **2005**, *7* (1), 67-79.
13. Guo, X.; Huang, Z. and Szoka, F. C. *Method. Enzymol.* **2004**, *387*, 147-152.
14. Alexis, F.; Pridgen, E.; Molnar, L. K.; Farokhzad, O. C. *Mol. Pharmaceutics* **2008**, *5* (4), 505-515.
15. Hrkach, J.; Hoff, D. V.; Ali, M. M.; Andrianova, E.; Auer, J.; Campbell, T.; Witt, D. D.; Figa, M.; Figueiredo, M.; Horhota, A.; Low, S.; McDonnell, K.; Peeke, E.; Retnarajan, B.; Sabnis, A.; Schnipper, E.; Song, J. J.; Song, Y. H.; Summa, J.; Tompsett, D.; Troiano, G.; Hoven, T. V. G.; Wright, J.; LoRusso, P.; Kantoff, P. W.; Bander, N. H.; Sweeney, C.; Farokhzad, O. C.; Langer, R. and Zale, S. *Sci. Transl. Med.* **2012**, *4* (128), 128-139.

16. Wang, J.; Tian, S.; Petros, R. A.; Napier, M. E. and DeSimone, J. M. *J. Am. Chem. Soc.* **2010**, *132* (32), 11306-11313.
17. Prabhakar, U.; Maeda, H.; Jain, R. K.; Sevic-Muraca, E. M.; Zamboni, W.; Farokhzad, O. C. Barry, S. T.; Gabizon, A.; Grodzinski, P. and Blakey, D. C. *Cancer Res.* **2013**, *73*(8), 2412-2417.
18. Sengupta, S. and Kulkarni, A. *ACS Nano* **2013**, *7* (4), 2878-2882.
19. Chu, K. S.; Schorzman, A. N.; Finniss, M. C.; Bowerman, C. J.; Peng, L.; Luft, J. C.; Madden, A. J.; Wang, A. Z.; Zamboni, W. C. and DeSimone, J. M. *Biomater.* **2013**, *34* (33), 8424-8429.
20. Chu, K. S.; Finniss, M. C.; Schorzman, A. N.; Kuijter, J. L.; Luft, J. C.; Bowerman, C. J.; Napier, M. E.; Haroon, Z. A.; Zamboni, W. C. and DeSimone, J. M. *Nano Lett.* **2014**, *14* (3), 1472-1476.
21. Dai, Y.; Xiao, H.; Liu, J.; Yuan, Q.; Ma, P.; Yang, D.; Li, C.; Cheng, Z.; Hou, Z.; Yang, P. and Lin, J. **2013**, *135*, 18920-18928.
22. Xiao, H.; Qi, R.; Liu, S.; Hu, X.; Duan, T.; Zheng, Y.; Huang, Y. and Jing, X. *Biomater.* **2011**, *32* (30), 7732-7739.
23. Parrott, M. C.; Finniss, M.; Luft, J. C.; Pandya, A.; Gullapalli, A.; Napier, M. E. and DeSimone, J. M. *J. Am. Chem. Soc.* **2012**, *134* (18), 7978-7982.
24. Dunn, S. S.; Tian, S.; Blake, S.; Wang, J.; Galloway, A. L.; Murphy, A.; Pohlhaus, P. D.; Rolland, J. P.; Napier, M. E. and DeSimone, J. M. *J. Am. Chem. Soc.* **2012**, *134* (17), 7423-7430.

## APPENDIX

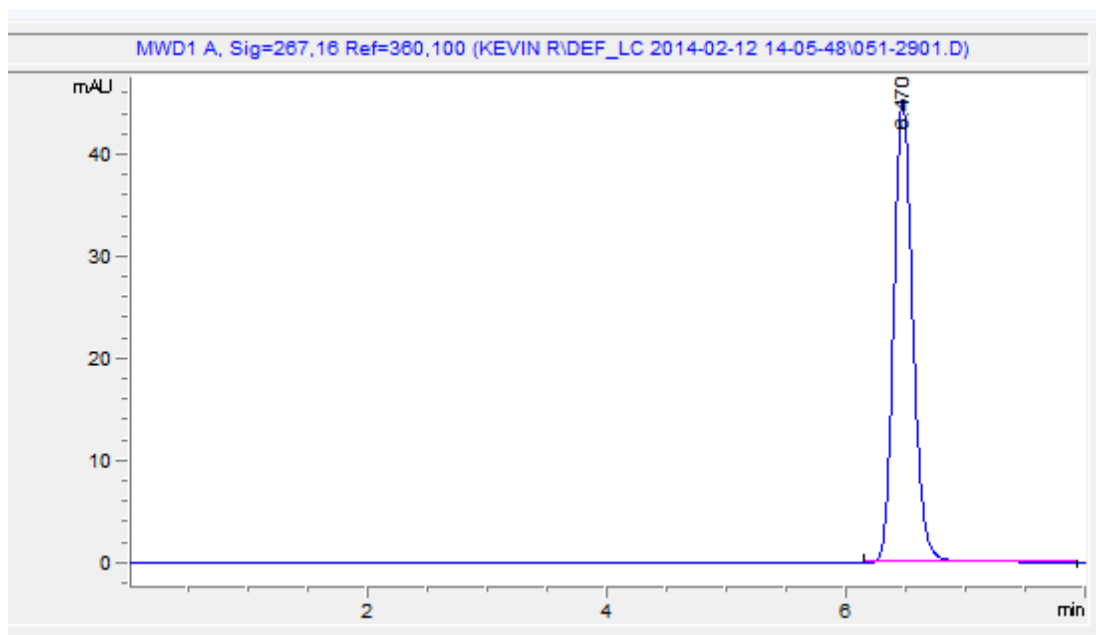


Figure A.1 Chromatogram of gemcitabine·HCl (0.25 mg / mL in sterile water) upon analysis via HPLC (Abs = 267 nm) with observed elution time of ~ 6.5 min.

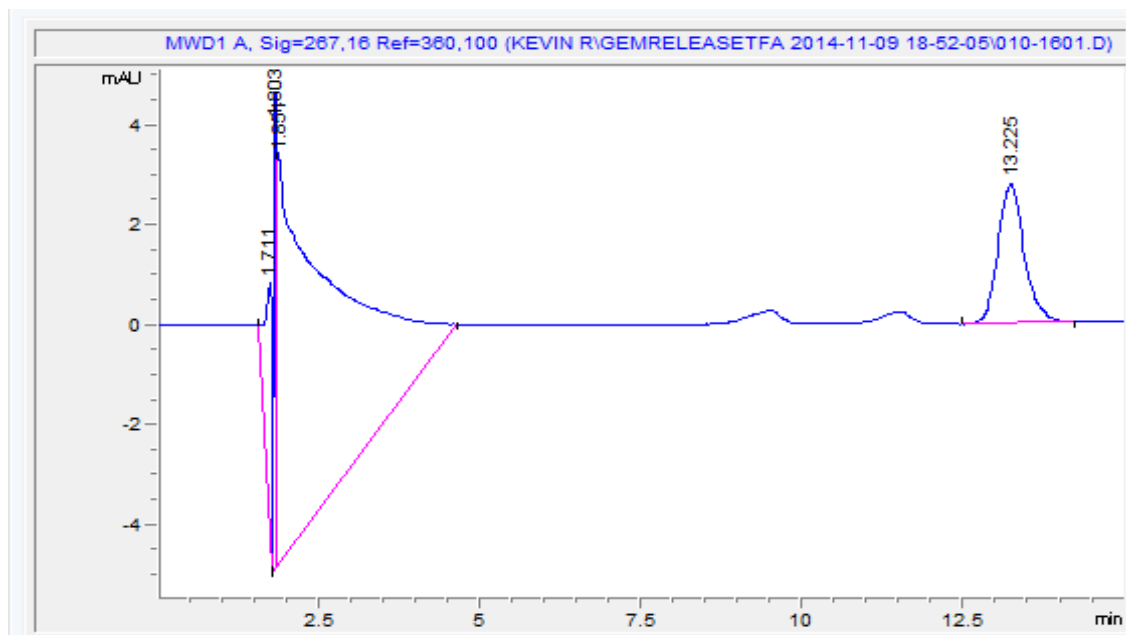


Figure A.2 Chromatogram of SS-GEM pro-drug (0.1 mg / mL in sterile water) upon analysis via HPLC (Abs = 267 nm) with observed elution time of ~ 13.2 min.

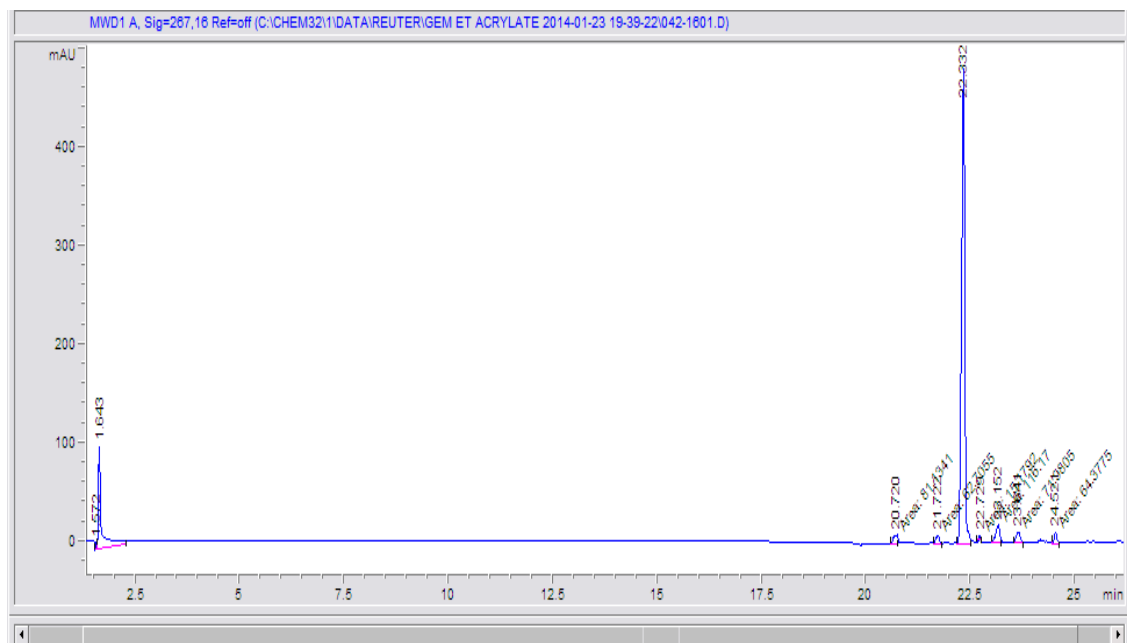


Figure A.3 Chromatogram of iPr-GEM pro-drug (0.1 mg / mL in sterile water) upon analysis via HPLC (Abs = 267 nm) with observed elution time of ~ 22.2 min.

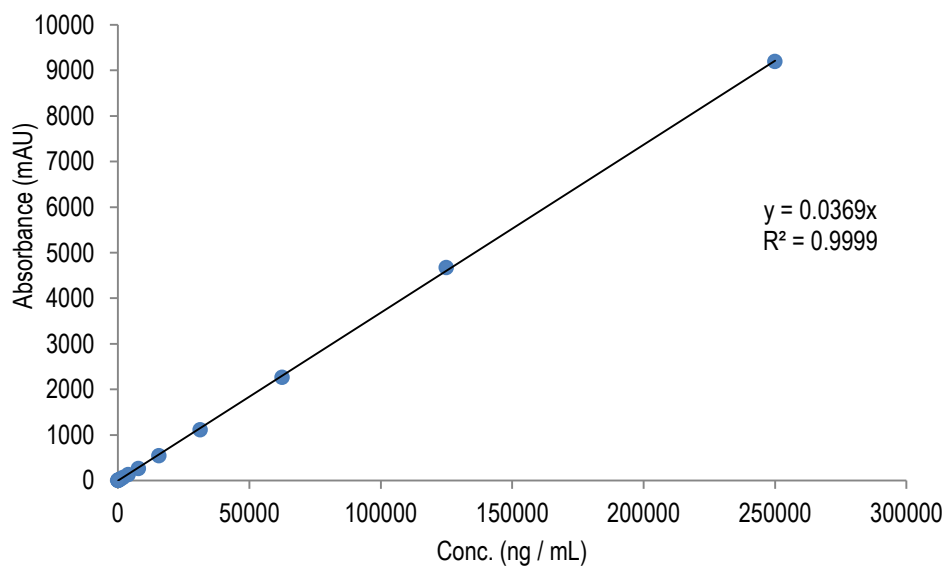


Figure A.4 Standard curve of gemcitabine (10 standard dilutions) upon analysis via HPLC (Abs = 267 nm).